Acknowledgements

I am grateful to Dr. V.K. Dadhwal, Dean, IIRS for extending his full support and providing the necessary facilities throughout the course.

I am deeply thankful to my project supervisor, Mr. I.C. Das, Scientist "SF" for his guidance, patience and encouragement, without which this project would have not come to fruition.

I feel indebted to Prof. R.C. Lakhera, Head, Geosciences Division for his constant help, co-operation and supervision all through the course.

I offer my sincere thanks to the faculty members of the Geosciences Division Prof. V.K. Jha, Prof. S.K. Srivastav, Dr. P.K. Champati Ray, Dr. R.S. Chatterjee, - for providing all valuable suggestions and support at each and every step.

I am very much thankful to Mr. Milap Punia, Senior Lecturer, JNU, Delhi for his valuable suggestions.

I am extremely thankful to Dr. A. K. Mishra, Marinesciences Division for his support throughout my M.Tech programme as our course co-ordinator.

I am extremely thankful to Mr Velumurugan Scientist Agriculture and Soil Division for his support and guidance during the field spectra collection using Analytical Spectral Device (ASD).

I convey my sincere thanks to Mr. Prasanth Kawishwar, Mr. Vivek Kumar Singh, Mr. Asit Baron Mahato, Ms Arpita Sinha, Mr. Nishadh S., Mr. Rajeev R.K.N, Mr. Prashob Raj, Mr. Sam Varghese, Mr. L. K. Sekhar, Mr. Prasanth K and Mr. Muhammed Rafeek V. T. for providing me support during my project work.

I am also thankful to all my fellow trainees, Mr. Rahul K. Pandey, Mr. Ramesh Kumar, Ms Debaraty Roy for their constant support.

I am also thankful to all the non-teaching staff of IIRS for their help and support during my stay in IIRS.

I am also thankful to my family and friends back home for their constant inspiration. My work would not have been possible without the help from all these well-wishers.

Dehra dun (Ashok Sekhar)

Abstract

Hyperion sensor is a hyperspectral imager on-board of EO-1 satellite. The product is distributed by USGS, and the level one product, which is only radiometrically corrected, is available. The EO-1 satellite was launched on November 21, 2001.

Hyperspectral imaging sensors have been used for more than a decade to aid in the detection and identification of diverse surface targets, topographical and geological features but the datasets are not immune to the effects of the intervening atmosphere. Various atmospheric constituents attenuate the incident and up-welling reflectance and finally degrade the signal corresponding to the feature being sensed. Thus, if this atmospheric attenuation could be identified and corrected for by using existing radiative transfer models, better understanding of the earth features should be possible.

The present study concentrate on the retrieval of reflectance image from the level one radiometrically corrected data two study areas, Udaipur (Rajasthan) and Jamda-Koira valley in Keonjhar district (Orissa). In this study, two atmospheric correction models have been used. FLAASH and ATCOR2 atmospheric correction models have been used to retrieve reflectance image from the radiance data. Preprocessing of the dataset need to be done before applying atmospheric correction on the dataset. Spectral subsettings of noise prone bands have been successfully done which leaves 196 unique bands from 242 bands of the hyperion dataset. Local destriping of the affected bands have been done using a 3*3 local mean filter. Atmospheric correction on the preprocessed image have retrieved reflectance image which have been validated using the statistical parameters Spectral Angle Mapper (SAM) and Normalized Euclidean Distance (NED). These statistical parameters were applied by taking the field spectra of geological samples generated from the Analytical Spectral Device (ASD) as the reference spectra. These statistical parameters indicated that the FLAASH model have outperformed the ATCOR2 model. Hence the FLAASH derived reflectance image has been further used for the spectral analysis and the mineral abundance mapping.

The mineral abundance mapping using the spectral analysis of the reflectance image involves the endmember collection using the N-Dimensional visualizer tool in ENVI software. Four endmembers were collected from the Udaipur study area and they are Kaolinite, Montmorillonite, Pyrophyllite and Fe rich Chlorite (Chamosite). Similarly for the Orissa study area, Hematite, minetailings and alluvium were selected as the endmembers after understanding the geology and analysis of the reflectance image. Various mapping techniques were applied to generate the final classified mineral abundance image. Linear Spectral Unmixing, Mixture Tune Matched Filtering, Spectral Feature Fitting, Spectral Angle Mapper and band absorption depth analysis were applied in this regard. In both the study areas, Linear spectral unmixing and Mixture Tune Matched Filtering gave good results in mapping the endmembers. In other techniques such as the Spectral Angle Mapper (SAM) and Spectral feature fitting have given intermixing of endmembers in both the study areas. Hence it can be concluded that an integrated approach of different mapping techniques will yield a better mapping of the endmembers. Band absorption analysis have not given good results due to lack of spectral quality in the SWIR portion of the Hyperion dataset.

Keywords: ATCOR, Endmembers, FLAASH, Hyperion, Linear Spectral Unmixing, Mixture Tuned Matched Filtering, Spectral Angle Mapper.

Chapter 1

1.1 Introduction

The materials of the mineral kingdom are wrested from the earth for man's necessities and comfort. Their search has given rise to voyages of discovery and settlement of new lands; their ownership has resulted in industrial development and in commercial or political supremacy or has caused strife or war. Their quest necessities a knowledge of their occurrence, distribution and mode of origin. The development of the industrial nations has coincided with the utilization of their mineral resources and that those countries lacking them tended to become agricultural and handicraft nations. The energy of coal and the solidity of metals spelled industrial growth and, in turn, industrial might, and other nations came to regard mineral self-sufficiency as one of the chief goals of economic nationalism. It is startling to realize that the insatiable demand for minerals to sustain modern industrialized economic life has caused the world to dig and consume more minerals within the period embracing the two World Wars than in all previous history. This made deep inroads into the storehouse of mineral resources-inroads heightened by war demands-and former bountiful supplies now show serious depletion. There is an important fact that needs to be realized. The more we manufacture, the greater are the inroads upon the very basis of nearly all manufacturing, and the greater the depletion of unrenewable mineral resources. This alarming consumption of mineral resources and the exhaustion of known reserves mean that new supplies must be discovered if industrial development is to persist unimpaired. With waning discoveries, search must be directed to less obvious occurrences, of which vast numbers must still lie hidden within the earth (Bateman 1988). These requirements followed by the new technologies have certainly helped us to look for the mineral resources. The modern technology has helped us to use various kinds of methods for mineral exploration. One of the most common techniques that are very much useful in mineral exploration prospecting is the Remote Sensing.

The term remote sensing can be defined as the science of acquiring, processing, and interpreting images that record the interaction between the electromagnetic energy and matter (Sabins, 1996). A physical quantity (light) emanates from a screen, which is a source of radiation. The radiated light passes over a distance, and thus is "remote" to some extent, until it encounters and is captured by a sensor (your eyes). Each eye sends a signal to a processor (your brain) which records the data and interprets this into information. Several of the human senses gather their awareness of the external world almost entirely by perceiving a variety of signals, either emitted or reflected, actively or passively, from objects that transmit this information in waves or pulses. Thus, one hears disturbances in the atmosphere carried as sound waves, experiences sensations such as heat (either through direct contact or as radiant energy), reacts to chemical signals from food through taste and smell, is cognizant of certain material properties such as roughness through touch, and recognizes shapes, colors, and relative positions of exterior objects and classes of materials by means of seeing visible light issuing from them. In the previous sentence, all sensations that are not received through direct contact are remotely sensed (source: http://www .crisp.nus.edu.sg/~research /tutorial/e ye.htm).

In other words, remote sensing involves the acquisition and measurement of data/information on some property(ies) of a phenomenon, object, or material by a recording device not in physical, intimate contact with the feature(s) under surveillance; techniques involve amazing knowledge pertinent to environments by measuring force fields, electromagnetic

radiation, or acoustic energy employing cameras, radiometers and scanners, lasers, radio frequency receivers, radar systems, sonar, thermal devices, seismographs, magnetometers, gravimeters, scintillometers, and other instruments (IIRS, 2005). Remote Sensing can be thought of as the "eyes" of such systems providing repeated synoptic (even global) visions of earth resources from an aerial or space vantage point. (source:http://www.gisdevelopment.net/tutorials/tuman008.htm)

The basic components of an ideal remote sensing are as follows.

- A uniform energy source.
- A non-interfering atmosphere.
- A series of unique energy-matter interactions at the earth's surface.
- A super sensor.
- A real time data processing and supply system.
- Multiple data users.

In any approach to applying remote sensing, not only must the right mixes of data acquisition and data interpretation techniques be chosen, but the right mix of remote sensing and "conventional" techniques must also be identified. Remote Sensing is a tool best applied in concert with others; it is not an end in itself. In this regard, remote sensing data are currently being used extensively in computer based GIS. The GIS environment permits the synthesis, analysis and communication of virtually unlimited sources and types of biophysical and socio-economic data–as long as they can be geographically referenced (Georgiadou et al., 2004).

The three most common methods of measuring the reflectance of a material are by (a) using hand-held spectrometer, (b) using aircraft mounted sensors or by (c) using spacecraft mounted sensor over the earth surface. Typically, hyperspectral spaceborne imaging spectrometers have been developed to measure the solar reflected upwelling radiance spectrum from 350 nm to 2560 nm at 5 to 10 nm resolution. Reflectance data in each spectral channel are pictorially represented as an image composed of discreet elements – pixels. Hyperspectral imagers collect data in contiguous narrow bands (up to several hundred bands) in the electromagnetic spectrum. They produce vast quantities of data because of the number of bands simultaneously imaged. Hyperspectral data provide unique capabilities to discern physical and chemical properties of Earth surface features not possible using current broad-band multi-spectral satellites. High spectral resolution allows identification of materials in the scene, while high spatial resolution locates those materials (Gross and Schott, 1998). Hence, hyperspectral data have enormous potential in target detection, high quality mapping, material mapping and identification.

One of the most promising and advanced remote sensing technique which is meant solely for mineral exploration is hyperspectral remote sensing or otherwise known as imaging spectrometry. Imaging spectroscopy is a relatively new technology that is currently being investigated by researchers and scientists with regard to the detection and identification of minerals, terrestrial vegetation, and man-made materials and backgrounds. Imaging spectroscopy has been used in the laboratory by physicists and chemists for over 100 years for identification of materials and their composition. Spectroscopy can be used to detect individual absorption features due to specific chemical bonds in a solid, liquid, or gas. Recently, with advancing technology, imaging spectroscopy has begun to focus on the Earth. The concept of hyperspectral remote sensing began in the mid-80 and to this point has been used most widely by geologists for the mapping of minerals. Actual detection of materials is dependent on the spectral coverage,

spectral resolution, and signal-to-noise of the spectrometer, the abundance of the material and the strength of absorption features for that material in the wavelength region measured (http://www.csr.utexas.edu/projects/rs/hrs/hyper.html)

Imaging spectrometers typically acquire images in a large number of spectral bands (more than 100). These bands are narrow (less than 10 nm to 20 nm in width), and contiguous (i.e. adjacent), which enables the extraction of reflectance spectra at pixel scale. Such narrow spectra enable the detection of the diagnostic absorption features which are not represented or manifested by the multispectral sensors. When light interacts with a mineral or rock. The objectives of these hyperspectral imaging spectrometers are to use the molecular absorptions and constituent scattering characteristics expressed in the spectrum to (1) detect and identify the surface and atmospheric constituents present; (2) assess and measure the expressed constituent concentrations; (3) assign proportions to constituents in mixed spatial elements; (4) delineate spatial distribution of the constituents; (5) monitor changes in constituents through periodic data acquisitions; and (6) to validate, constrain and improve models (Pantazis et al., 1998). Imaging spectrometers have been designed to meet spectral, spatial, and radiometric requirements, enabling measurements from spaceborne imaging spectrometers in terms of the range, sampling, response, stability, uniformity, precision, and accuracy. Spectral remote sensing has the potential to provide the detailed physico-chemistry (mineralogy, chemistry, morphology) of the earth's surface. This information is useful for mapping potential host rocks, alteration assemblages and regolith characteristics. In contrast to the older generation of low spectral resolution systems, such as the Landsat Thematic Mapper with only six "reflected" bands, the new generation of hyperspectral systems enable the identification and mapping of detailed surface mineralogy using "laboratory-grade" spectroscopic principles (clark.et.al., 1990).

With the aid of hyperspectral remote sensing, an extensive range of minerals can be remotely mapped, including iron oxides, clays, micas, chlorites, amphiboles, talc, serpentines, carbonates, quartz, garnets, pyroxenes, feldspars and sulphates, as well as their physico-chemistries such as the cation composition and long and short range order (Cudahy, 2002).There are many applications which can take advantage of hyperspectral remote sensing. The major general applications of hyperspectral remote sensing for the various application fields are as follows.

- Atmosphere: water vapor, cloud properties, aerosols
- Ecology: chlorophyll, leaf water, cellulose, pigments, lignin
- Geology: mineral and soil types
- Coastal Waters: chlorophyll, phytoplankton, dissolved organic materials, suspended sediments
- Snow/Ice: snow cover fraction, grain-size, melting
- Biomass Burning: sub-pixel temperatures, smoke
- Commercial: mineral exploration, agriculture and forest production

Hyperspectral data (or spectra) can be thought of as points in an n-dimensional scatterplot. The data for a given pixel corresponds to a spectral reflectance for that given pixel. The distribution of the hyperspectral data in n-space can be used to estimate the number of spectral endmembers and their pure spectral signatures and to help understand the spectral characteristics of the materials, which make up that signature.

1.2 Atmospheric correction

Raw calibrated imaging spectrometer data have the general appearance of the solar irradiance curve, with radiance decreasing towards longer wavelength, and exhibit several absorption bands due to scattering and absorption by gases in the atmosphere. The major atmospheric water-vapour bands (H_2O) are centered approximately at 0.94μm, 1.14 μm, 1.38μm and 1.88 μm, the oxygen (O_2) band at 0.76 μm, and carbon dioxide (CO_2) bands near 2.01 and 2.08 μm. Additionally, other gases in the atmosphere including ozone (O_3), carbon monoxide (CO), nitrous oxide (N_2O) and methane (CH_4), produce noticeable absorption features in the 0.4 – 2.5 μm wavelength region. The effect of the atmospheric calibration algorithm is to re-scale the raw radiance data provided by imaging spectrometers to reflectance by correcting for atmospheric influence thus shifting all spectra to nearly the same albedo. The result is a data set in which each pixel can be represented by a reflectance spectrum, which can be directly compared to reflectance spectra of rocks and minerals acquired either in the field or in the laboratory. Reflectance data obtained can be absolute radiant energy or apparent reflectance relative to a certain standard in the scene. Calibration to reflectance can be conducted to result in absolute or relative reflectance data. Radiation reaching the sensor can be split into four components: path radiance, reflected direct radiance, and reflected radiance from neighborhood. Radiative transfer RT codes model the atmosphere's optical behavior given user defined boundary conditions. The inverse problem of atmospheric correction of imaging spectrometer data with the aim of obtaining radiance and/or reflectance at the ground surface can be achieved in three ways, 1. Emperical correction methods for apparent surface reflectance, 2. Use of RT codes to obtain apparent absolute reflectance, 3. In-flight calibration of airborne optical sensors.

1.2.1Atmospheric correction models

A number of atmospheric correction models are available in read to use softwares. Some of the most commonly used atmospheric correction models are as follows. Atmospheric CORrection Now (ATCOR), Fast Line-of-Sight Atmospheric Analysis of Spectral Hypercubes (FLAASH) developed on Moderate Resolution Atmospheric Radiance and Transmittance Model (MODTRAN); Atmosphere REMoval Program (ATRIM), ATCPRO and High Accuracy ATmospheric Correction for Hyperspectral data (HATCH) developed on 5S Code (Simulation of the Satellite Signal in the Solar Spectrum) and 6S code (Second Simulation of the Satellite Signal in the Solar Spectrum) respectively.

The method to be used for atmospheric correction is a function of nature of problem, the type of remote sensing data, the amount of in situ historical atmospheric information available, and how accurate the bio-physical information is to be extracted from the remote sensing data (Jensen, 1996). To process hyperspectral image datasets, statistical based relative atmospheric correction methods and physics based absolute correction models are available.

An image comprises of a series of spectral bands, the pixels of which each have a digital number (DN). In a raw unprocessed image, pixel DN is a linearly transformed representation of at-sensor radiance for a discrete resolved area of the Earth's surface (Lillesand and Kiefer, 1999). Image spectrometric studies and atmospheric correction operations, however, need at-sensor radiance. The radiance-to-DN procedure of image acquisition for each spectral wavelength must be inverted to derive radiance from DN.

$$DN = \left(\frac{DN_{\max}}{L_{\max} - L_{\min}} \right) \times \left(L - L_{\min} \right)$$

$$L = \left(\frac{L_{\max} - L_{\min}}{DN_{\max}} \right) \times DN + L_{\min}$$

As pixel DN is a simple linear transformation of radiance, the slope and offset of this linear transformation (which is specific for each spectral band, each sensor and initial calibration) can be used to calculate radiance L (measured in $W/m^2/sr/\mu m$) using equation-2-2, and inversely used to calculate pixel DN using equation-2-1. The gain and offset values are unique for each spectral band acquired by a particular sensor. These values change over the life span of a sensor, so the most recent values are used. For Hyperion, these values are made available to the user with the dataset.

At sensor-reflectance involves taking into account temporal changes in solar illumination due to Earth-Sun geometry, as it changes with time of the year of imaging. The solar spectral irradiance (incident energy reaching the target) of the light reaching the atmosphere is reasonably well characterized; however, the spectrum of the solar radiation reaching the ground is altered temporally and geographically because of changing atmosphere. Such atmospheric modulation effects have to be accounted for in order to recover reliable reflectance spectra of materials on the ground. The effect of scattering on remotely sensed solar radiation reflected by the ground surface is most commonly given by:

$$\rho_p = \frac{\pi . L_\lambda . d^2}{ESUN_\lambda . \cos\theta_S}$$

Where

ρ_p = Unitless planetary reflectance

L_λ = Spectral radiance at the sensor's aperture

d = Earth-Sun distance

$ESUN_\lambda$ = Mean solar Exo-atmospheric irradiances

θ = Solar zenith angle in degrees

The following flowchart describes the various atmospheric correction techniques available for the retrieval of reflectance from radiance.

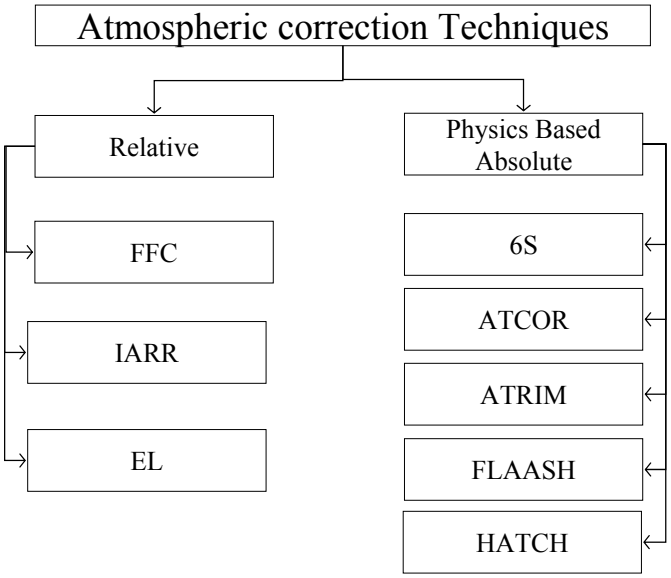

Figure 1.1 various atmospheric correction techniques

1.2.2 Relative reflectance

The correction methods involved in the retrieval of relative reflectance are as follows.

1. Flat field correction
2. Internal average relative reflectance correction
3. Empirical line correction

The purpose of the flat field correction is to reduce the atmospheric influence in the raw imaging spectrometer data and eliminate the solar irradiance drop-off, as well as any residual instrument effects. This is achieved by dividing the whole data set by the mean value of an area within the scene which is spectrally and morphologically flat, and spectrally homogeneous. The flat-field chosen should have a high albedo to avoid decreasing the signal-to-noise ratio. This can also be achieved by increasing the number of pixel spectra used to produce the flat field spectrum.

The Internal Average Relative Reflectance (IARR) correction method allows the calibration of raw imaging spectrometer data to reflectance data when no calibration information is available. This procedure uses an "Average Reference Spectrum" (ARS) calculated as the average pixel spectrum of the entire scene. This spectrum is divided into each image radiance spectrum to produce a relative reflectance spectrum for each pixel.

Conversion of raw imaging spectrometer data to reflectance data using the Empirical Line method requires the selection and spectral characterization of two calibration targets, thus assuming a priori knowledge of each site. This empirical correction uses a constant gain and offset for each band to force a best fit between sets of field spectra and image spectra

characterizing the same ground areas thus removing atmospheric effects, residual instrument artifacts and viewing geometry effects.

1.2.3 Absolute reflectance

Absolute reflectance data without a priori can be obtained using atmospheric correction models. These models correct for scattering and absorption in the atmosphere due to water vapor and mixed gases as well as for topographic effects and different illumination conditions. The 0.94 μm and 1.1μm water absorption bands are used to calculate water vapor in the atmosphere while transmission spectra of the mixed gases in the 0.4 – 2.5 μm wavelength region are simulated on basis of the water vapor values found and the solar and observational geometry. Scattering effects in the atmosphere are modeled using radiative transfer codes. A typical atmospheric correction algorithm using RT(Radiative Transfer) codes typically models the atmosphere's behavior on incident radiation through deriving transmission spectra of the main atmospheric gases and water-vapor which is integrated with effects of atmospheric scattering from aerosols and molecules. User input on atmosphere condition required is the date, time and location of data take, ozone depth, aerosol type, visibility, elevation. This is derived from radiosonde data or meteorogical stations in the area to be imaged. One of the earliest absolute atmospheric correction method using radiative transfer approaches to simulating the atmosphere–surface system was presented by Turner and Spencer in 1972. During the 1980s, considerable work was done on the atmospheric correction of satellite imagery and improvements in modeling and computational capabilities led to the development of the 5S atmospheric radiation model in 1990s, which was used extensively for the atmospheric correction of airborne visible/infrared imaging spectrometer (AVIRIS) datasets. Since 1990 numerous radiative transfer models have been developed, the most popular amongst these is a publicly available code MODTRAN, developed by Spectral Science, Inc. and Air Force Research Laboratory. The normally used RT codes are LOWTRAN, MODTRAN, 5S and 6S. The atmospheric correction for the reflective (VIS-SWIR) and thermal spectral regions are dealt separately since the influence of the sun dominates the solar reflective region while it can be neglected in the thermal region. The basic relation defining spectral radiance in the VIS-SWIR region is given by

$$L\lambda = L0(\lambda) + \frac{Eg(\lambda)}{\Pi}\left[\tau(\lambda) + \tau(\lambda)\right]\rho(\lambda)$$

where, $L_0(\lambda)$ is the path radiance for a black body (ρ=0), $E_g(\lambda)$ is the global irradiance on the ground, $\tau_{dir}(\lambda)$ is the direct atmospheric transmittance (ground to sensor), $\tau_{dif}(\lambda)$ is the diffuse atmospheric transmittance (ground to sensor), and $\rho(\lambda)$ is the reflectance of a Lambert region.

For spaceborne sensor, the following relation can be demonstrated to relate ground reflectance, ρ, to the DN value.

$$\rho = {}^{1}\!/_{a1}\left[\frac{\Pi\left(C0 + C1DN\right)}{E5Cos\theta s} - a0\right]$$

where E_5 is the terrestrial solar irradiance, θ_s is the solar zenith angle, and a0 and a1 are atmospheric functions relating planetary albedo, ρ_p to ground albedo, ρ, as

$\rho_p = a_0 + a_1 x \rho$

1.3 Moderate Resolution Atmospheric Transmission (MODTRAN)

The Moderate Resolution Transmittance (MODTRAN) Code calculates atmospheric transmittance and radiance for frequencies from 0 to 200nm at moderate spectral resolution of 0.0001 μm (1 cm^{-1}). MODTRAN was developed for higher spectral resolution for molecular band parameterization, spherical refractive geometry, solar and lunar source functions, scattering (Rayleigh, Mie, single and multiple), and default profiles (gases, aerosols, clouds, fogs, and rain) (Kneizys et al., 1996). The upgraded MODTRAN4 corrects for water line parameter errors parameters led to a very small increase in the retrieved water column amount, from 1550 to 1570 atm-cm, due to a ~1% change in the 1130 nm band strength (Matthew et al., 2000).
The standard mathematical expression for spectral radiance at a sensor pixel applicable to SWIR through UV wavelengths, where thermal emission is negligible is expressed as:

$$L^* = \left[\frac{A\rho}{(1-\rho eS)}\right] + \left[\frac{B\rho e}{(1-\rho eS)}\right] + L^* a$$

Where, L^* is spectral radiance at sensor, ρ is the pixel surface reflectance, ρe is an average surface reflectance for the pixel and the surrounding region, S is the spherical albedo of the atmosphere, L*a is the radiance backscattered by the atmosphere and A and B are coefficients that depend on atmospheric and geometric conditions. The first term in the above equation corresponds to the radiance from the surface that travels directly into the sensor, while the second term corresponds to the radiance from the surface that is scattered by the atmosphere into the sensor. The distinction between ρ and ρ_e accounts for the "adjacency effect" (spatial mixing of radiance among nearby pixels) that is caused by atmospheric scattering. The adjacency effect correction can be turned off by setting $\rho_e = \rho$. For a specified model atmosphere the values of A, B, S and L*a in above equation can be determined empirically from the standard MODTRAN4 outputs of total and direct-from-the-ground spectral radiances computed at three different surface reflectance values, such as 0, 0.5 and 1. The viewing and solar angles of the measurement and nominal values for the surface elevation, aerosol type and visible range for the scene are used. To account for possible variations in column water vapor across the scene these calculations are looped over a series of varying water profiles. The water retrieval is performed rapidly with a 2-dimensional look-up table (LUT) constructed from the MODTRAN4 outputs using “Delaunay triangulation” procedure. After the water retrieval is performed, Equation 2-4 is solved for the pixel surface reflectance in all of the sensor channels. A procedure analogous to the water vapor determination can be used to retrieve a scene elevation map. Here the MODTRAN4 calculations are looped over elevation rather than water vapor concentrations and an absorption band of a uniformly mixed gas such as O_2 or CO_2 is interrogated.

MODTRAN4 options can be selected that control the tradeoff between accuracy and computational speed. These include the number of water vapor column amounts, the multiple scattering algorithm (Isaacs 2-stream or DISORT n-stream) (Matthew et al., 2000). The two most commonly used atmospheric correction models FLAASH (Line-of-Sight Atmospheric Analysis of Spectral Hypercubes) and ATCOR (Atmospheric Correction) were used in the present study which will be discussed in the later sections.

1.4 Mineral mapping using hyperspectral remote sensing

One of the major applications of hyperspectral remote sensing is the mineral exploration. It was Goetz et al. (1982) who demonstrated that spectroscopy may aid in surface mineral mapping. This led to the greatest breakthrough in the application of hyperspectral remote sensing when Murphy (1995) for the first time succeeded in mapping jasperoid in the C mountains. Reflectance spectra have been used for many years to obtain compositional information of the earth surface. Spectral reflectance in visible and near-infrared offers a rapid and inexpensive technique for determining the mineralogy of samples and obtaining information on chemical composition. Electronic transition and charge transfer processes associated with transition metal ions determine largely the position of diagnostic absorption features in the visible – and near-infrared wavelength region of the spectra of minerals (burns, 1970). In addition, vibrational processes in H_2O and OH produce fundamental overtone absorptions (Hunt, 1971). The position, shape, depth, width and asymmetry of these absorption features are controlled by the particular crystal structure in which the absorbing species is contained and by the chemical structure of the mineral. Thus, variable characterizing absorption features can be directly related to the mineralogy of the sample. The most common electronic process revealed in the spectra of minerals is the crystal field effect which is the result of unfilled electron shells of transition elements (e.g., Fe, Cr, Co, Ni). All transition elements have identical energies in an isolated ion, but the energy levels are split when the atom is located in a crystal field. This splitting of the orbital energy enables an electron to be moved from a lower level into a higher one by absorption of a photon having an energy matching the energy transfers. These absorption bands are diagnostic of mineralogy. Some minerals exhibit two energy levels in which electrons may reside: a higher level called the conduction band, where electrons move freely throughout the lattice, and a lower energy region called the valence band, where electrons are attached to individual atoms. Changes in these result in absorption features in the visible portion of the electromagnetic wavelength spectrum. These vibration features results in absorption features at high (SWIR-MIR) wavelengths with deep and narrow features. Reflectance spectra of minerals are dominated in the visible to near-infrared wavelength range by the presence or absence of transition metal ions. The presence or absence of water and hydroxyl, carbonate and sulphate determine the absorption features in the SWIR region due to the so called vibrational process. The atmospherically corrected hyperspectral reflectance data enables as to map the various minerals present in the exposed rock surface due to these vibrational process, which is diagnostic for each mineral. This study attempts to map the various minerals present in the exposed rock surface in the study area.

1.5 Problem Definition

Geologic remote sensing has always a challenge to prove itself because of the nature of application in geologic fields. Present study was taken up in a challenging fashion to show the degree of application of geologic remote sensing in highly contrasting locations using the most modern technology of hyperspectral remote sensing. Mineral exploration is becoming increasingly difficult, especially in obtaining ground access to sensitive or remote areas. The multispectral sensors that are most commonly used in remote sensing systems acquire data in a number of relatively broad wavelength bands. The typical diagnostic absorption features, characterizing materials of interest in reflectance spectra, are on the order of 20 nm to 40 nm in width. Hence, the broadband sensors under-sample this information and do not allow to exploit the full spectral resolving potential available. Hyperspectral remote sensing combines imaging and spectroscopy in a single system which often includes large data sets and requires new processing methods.

Hyperion sensor is a hyperspectral imager on-board of EO-1 satellite. The product is distributed by USGS, and the level one product, which is only radiometrically corrected, is available. The EO-1 satellite was launched on November 21, 2001. Processing of high dimensional hyperspectral data is a challenging task and the computational complexity is a result of vast data volume in numerous spectral bands.

Hyperspectral imaging sensors have been used for more than a decade to aid in the detection and identification of diverse surface targets, topographical and geological features but the datasets are not immune to the effects of the intervening atmosphere. Various atmospheric constituents attenuate the incident and up-welling reflectance and finally degrade the signal corresponding to the feature being sensed. Thus, if this atmospheric attenuation could be identified and corrected for by using existing radiative transfer models, better understanding of the earth features should be possible. In absence of these models the inferences would lead to erroneous detection, identification and quantification of the features of interest. Thus atmospheric correction refers to the removal of unwanted atmospheric components of the measured radiance.

The apparent reflectance should be derived because the data released from USGS is the level one, radiometrically corrected only, for spectral analysis based applications. This process is named atmospheric correction.

Deriving absolute reflectance for space borne platforms is of interest to all geoscientists as it offers an opportunity to know the composition, spectral property of material and compare field measured reflectance values. Absolute reflectance is a ratio of reflected to incident flux. The signals received at the satellite are an integrated spectral response of the target within the designed spectral width of the sensor; this signal is provided to the user in form of digital numbers (DN). In raw unprocessed image DN values do not quantitatively correspond to the physical units such as radiance, reflectance or temperature. Thus, remote sensing studies which intend to utilize satellite data for estimation of quantitative spectral surface characteristics need to convert the DN to target reflectance/absolute reflectance (Pandya et al., 2002). Various atmospheric correction models have been in use to estimate reflectance. Existing atmospheric correction models can be grouped in two basic categories: statistical or empirical, and absolute or physics based. Most widely used statistical models like Empirical Line Method (ELM), Internal average relative reflectance (IARR), Flat Field Correction (FFC) works similarly, normalizing the hyperspectral data to an area of known flat reflectance, and convert DN to relative reflectance. The primary output product of all Physics based atmospheric correction models, is the surface reflectance. In the present study, the two of the most commonly used physics-based models used are ATmospheric CORrection now (ATCOR2) and Fast Line-of-Sight Atmospheric Analysis of Spectral Hypercubes (FLAASH), developed on MORTRAN radiative transfer code have been used.

1.6 Research Objectives

The main aim of the study is to map the mineral abundance in the study area using the hyperion data set.
The objectives of the present study are as follows.

1. Atmospheric Correction of the data set using two radiative transfer models (FLAASH and ATCOR).
2. Laboratory spectra generation of different rock samples from the representative horizons using ASD spectroradiometer.

3. Mineral Abundance mapping using the various endmembers extracted from the image.
4. Validation of the Hyperion image spectra with the spectra generated from the field using the various spectral similarity measures such as the SAM, NED.
5. Lithological differentiation using the various classified mineral images.

1.7 Research Questions

Some of the research questions that have been addressed in the present study are as follows.

1. Can the existing the pre-processing techniques used in the multispectral images sufficient for the efficient feature extraction in hyperspectral data?

2. How good are the atmospheric correction models that have been used for the retrieval of reflectance in hyperspectral (Hyperion L1R) data?

3. Which among the various mapping techniques are the most efficient for the mineral mapping?

4. Can the statistical parameters like SAM (Spectral Angle Mapper) and NED (Normalised Euclidean Distance) be used as the validation parameters for the various atmospheric correction models?

1.8 Outline of the report

This thesis comprises of five chapters. The thesis commences with the abstract followed by the introduction and objectives of the study in Chapter 1, followed by the geological/geomorphologic, physiographical and climatic details of the study area and data used in Chapter 2. Chapter 3 deals with the methodology adopted for the present study and followed by results and analysis in chapter 4. The conclusions of the present study are given in chapter 5.

Chapter 2

Study Area

Two study areas have been selected for the present study. The Hyperion scenes which include the Udaipur city of Rajasthan and its surroundings as well as the Jamda-Koira valley of Keonjhar, Orissa have been the two study areas selected for the present study. Two study areas have been chosen for the present study keeping in mind the contrasting topography. Jamda-Koira valley of Keonjhar, Orissa is a densely vegetated terrain with large number of hillocks and dissected hills spread out throughout the valley. The Udaipur city of Rajasthan comes under the semi-arid terrain with negligible amount of vegetation. Geologically both the regions come under the Pre-Cambrian era of the geological time scale.

The Aravalli range, one of the oldest mountain ranges of the world runs along the NE–SW direction for more than 720 km, covering nearly 40,000 km^2. The study area (Longitude 73° 32′ 58″ to 73° 49′ 35″ E and Latitude 24° 08′ 18″ to 24° 59′ 53″ N) covers an area of about 750 km^2 of this main block of the Aravalli range corresponding to path and row number 146/40 corresponding to full scene of Hyperion. The available Hyperion scene covers major parts of Udaipur city, and part of the Hindustan Zinc Limited-Zawar mines area, which are geologically part of Zawar formation of Upper Arawalli Group. The region is dry for most of the year except the rainy season, and exhibits semiarid climate. Monsoon winds mainly contribute to the rainfall in this region mainly during June–September; non-monsoon rainfall is limited and irregular. Annual rainfall in this region varies from 10 cm in the north-west to 90 cm in the south east. Water resources, vegetation, agriculture and aquifer condition in this region vary mainly due to variations in physiographic, geomorphic and climatic conditions.

2.1 Study area 1

Jamda-Koira valley of Orissa state is well covered by the hyperion scene. The selected project area includes the South-Eastern margin of the famous Iron Ore super Group syncline, mainly consisting of iron ore group, is bounded by latitude 21^0 45’ to 22^0 00’ N and longitude 85^0 15’ to 85^0 30’ E occupying an area of approximately 770 sq. Km. To the north of this area are the main townships of Joda, Barbil, Noamundi, Bolani, Kiriburu, Meghahatuburu and so many other mining centers of Fe and Mn ores. Most of the above mentioned towns are connected by railway and roadways routes to Jamshedpur, Rourkela, Keonjhar, Chaibasa and Bhubaneshwar. The area under the present study is unfortunately not provided with easily motorable road except north eastern and north-western parts.

2.1.1 Climate and Habitat

The selected area having hills upto 800 meters height, experiences maximum temperature of 45^0 C and minimum temperature of 23^0 and annual rainfall ranges between 1200 to 1400 mm, between months of June and October. So it experiences a tropical climate.

The sal trees dominate the floral cover and generally mixed vegetation predominates some reserved forests. Besides Sal (Sorea robusta) other plants include – Dhor, Assan, Kendu, Mahua, Bija, Mango, Jackfruit and Kusum etc.

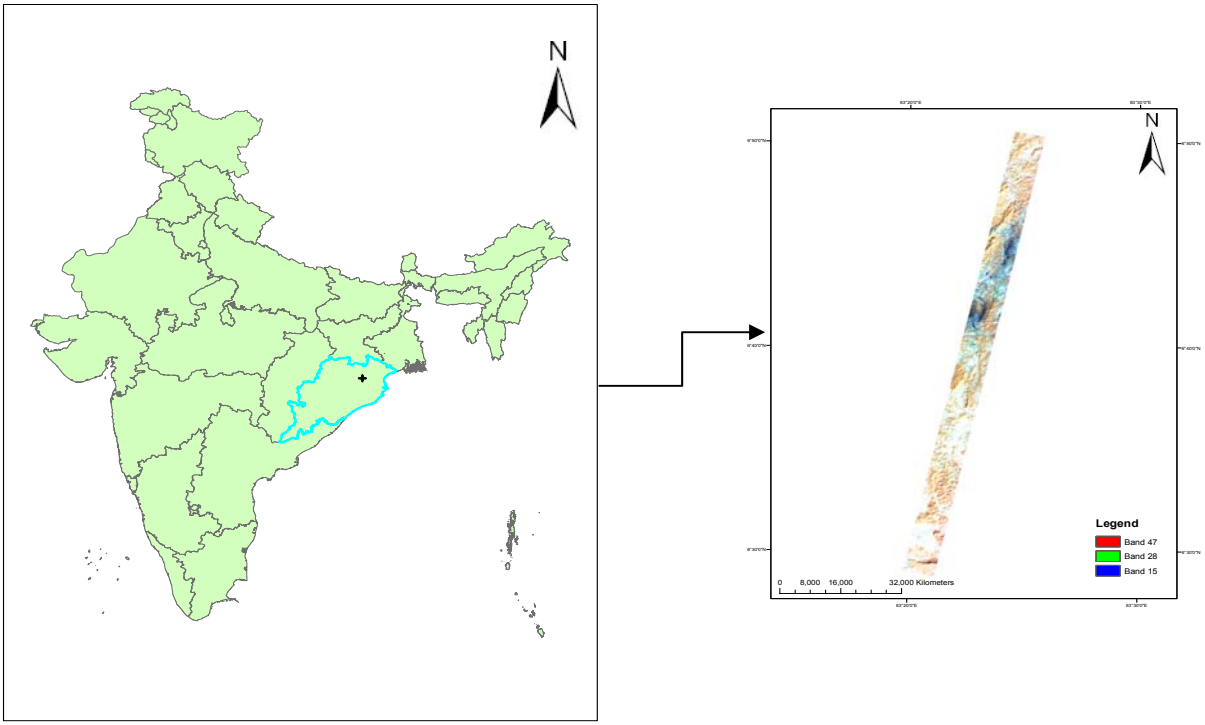

Figure 2.1 Study area Jamda-Koira (Orissa), Hyperion (FCC 47 28 15)

2.1.2 Physiography and Drainage

The area in general shows ridge and valley topography. The area exhibits high altitude zones rangng from 400 to more than 1000 meters from mean sea level (msl). Western part includes the overturned limbs of the iron ore syncline forming hogback structures while eastern part includes residual and subdued cuesta hills of the sandstone and orthoquartzites. The main river is Baitarani river flowing south to north having a east meandering trend. Kundra and Suna are the main tributaries to feed it. River Karo also feeds Baitarani. Assemblages of smaller orders of drainages merging towards the north indicate general slope towards north.

2.1.3 Geological Setting

The study area holds leading position in Iron and Manganese deposits in national scenario, so mostly the works of various experts have been done on the gensis and association of Fe and Mn deposits. The stratigraphy and structure are still debatable issues. Although various reknowned workers have tried to establish the geology of the region, claiming the regional structure to be a synclinorium with NE plunge.

On record Jones (1934) was the first to initiate the study in the belt, proposing the regional structure as a north plunging horse shoe shaped synclinorium with an overturned western limb. Dunn (1940) suggested three alternate stratigraphic sequences. Sarkar & Saha (1962-63) proposed them as NE plunging synclinorium overturned towards SE. Prasada Rao, Murthy and Deekshitulu (1964) established that it is U shaped basin open to the north, including lower lava as basement for Iron ore group, Shale composing of sediments, Banded Iron Formations (B.I.F) and

upper shale formation. However, they missed to incorporate sandstone formation in eastern margin. Banerjee (1977) supports this idea.

Saha and Sarkar (1977) based on the structural as well as radiometric data have tried to establish the chrono-stratigraphy of the region, suggesting the older metamorphics as basement, on which iron ore group of sediments formed this basin, starting with sandstone and conglomerates as the basal part. Afterward the singhbhum granite was intruded into the older metamorphics and IOG of rocks.

Murthy and Acharya (1975) called it koira Group and propose the structure as a low north plunging synclinorium slightly overturned towards east. Generally the workers, except few have worked in separate small patches, so entire area with regional geology is not fully explored.
The area under investigation is part of SE margin of the horse-shoe shaped, NE plunging synclinorium, also termed Bonai-Keonjhar-Singhbhum Iron-Manganese belt. It unconformably overlies the older metamorphic groups (OMG and probably later intruded by Singhbhum Granitic batholiths). It is bounded by the copper thrust belt in the north and Sukinda thrust in the south.
The belt is a narrow, NNE-SSW trending area, approximately 60 km. long and 25 km wide, defined by a spectacular 'U' shaped band of the resistant iron formation. The topography is generally very rugged with a high relief in the western and southern parts of the belt.

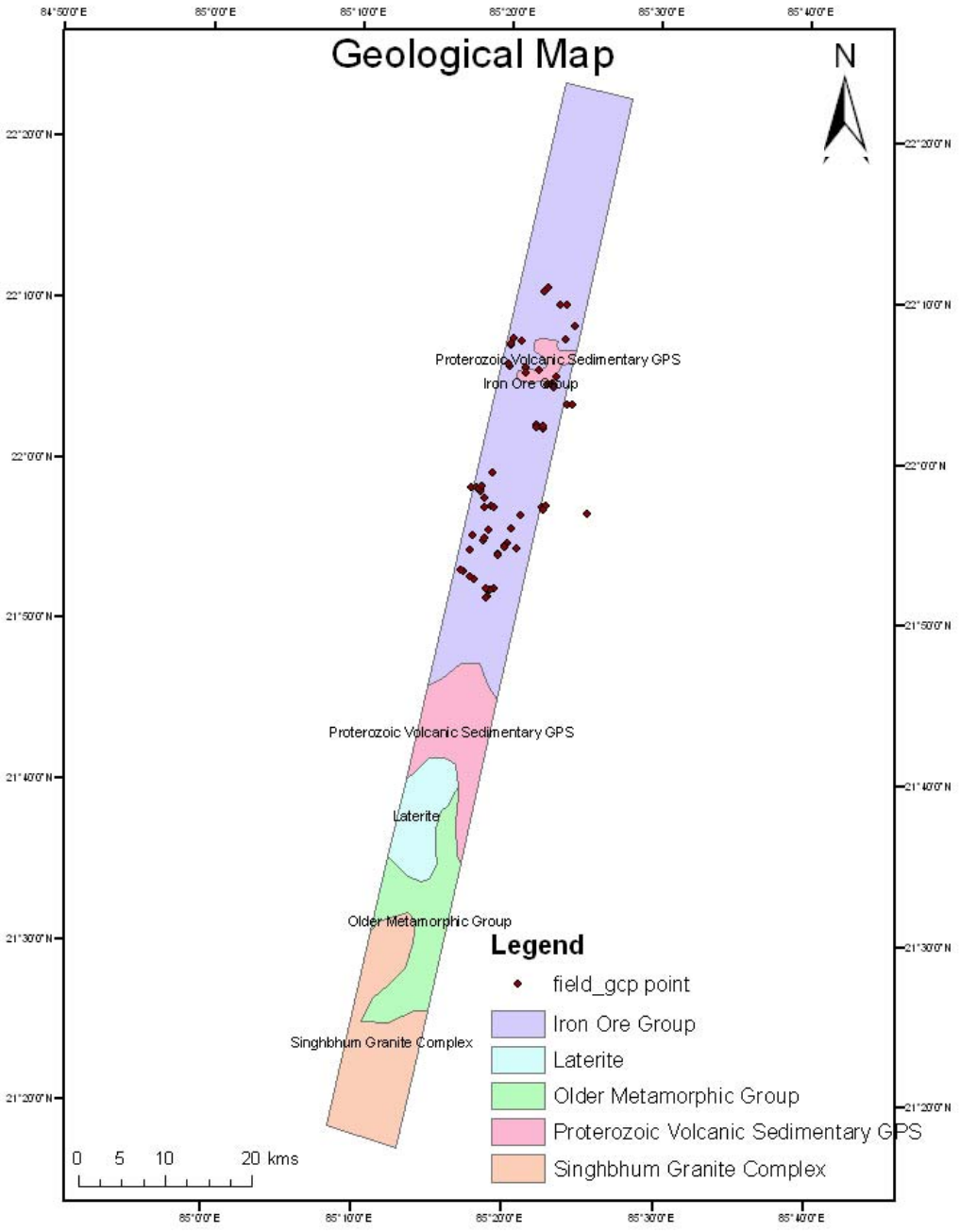

Figure 2.2 Geological map of study area (Orissa) modified after

2.1.3.1 Basal Sandstone:

It depicts lighter tone, gently dipping subdued hills forming cuesta landforms, with subdendritic to subparallel drainage, coarser texture with separately vegetated and having three sets of prominent joints in the directions E-W, N-S and NE-SW. It forms the basement of the lithological pile of the belt and occurs in the eastern and southern parts of the region. It has been

mapped around south of Basantpur, east of the Mahaparbat, Unchabali, north of Bamebari and along the Baitarani river. This formation comprises mainly of gritty sandstone, even grained orthoquartzite, characterized by white to reddish brown and gray hues. The bottom portions of the sandstone are interbedded with lenticular bands of conglomerate. The framework in the gritty sandstone is made up chiefly of white and gray quartz grains, rounded to well rounded, and the matrix is sillaceous and in the individual framework, the quartz grains show quartz overgrowths, It shows narrow beddings. The general strike is NE-SW dipping 8^0 - 10^0 (NW).

2.1.3.2 Volcanic formations:

Towards the top, the basal sandstone is interbedded with basic lava flows until ultimately it gives way to volcanc formation. Occuring to the south and east of the belt the volcanic formation occupies large areas around the "U" shaped closure. It generally forms low lying hills and flat or undulating area. The nearest exposures of the formation near Joda are, east of Bamebari, south of Dubna and Basanthpur and most of Lower Shale horizon south and east of lower part of the IOSG syncline. The pillow structure is observed around Namira lava hillock. They support sparse vegetation and smaller residual patches, with extensive soil cover and laterisation.

2.1.3.3 Lower Shale Formation:

This formation is underlain by volcanic formation. It is characterized by lack of banding or lamination, which is well marked in upper shale formation. It is of tuffaceous nature and altered into buff or purple coloured shaly rock. They are highly cultivated and associated with lava exposures. It has been reported in the right eastern and lower southern part of flanks of IOSG syncline of Iron Ore Group.

2.1.3.4 Banded Iron Formation:

The banded iron formation is characterized by the banded nature of hematite and Jasper. In the satellite image they are characterized by the ridge-valley topography, resistant linear ridges, forming hogbacks with high relief, parallel to subparallel drainage, moderate drainage density, coarse texture, sharp contact with other lithounits, generally forms anticlinal hills. The thick vegeatation on BHJ gives darker tone in the imagery. Also active mining areas are well identified due to its peculiar bluish to greenish tinge inside the BHJ area. On the slopes and eroded areas laterite cappings are marked. Due to their high resistance to erosion jaspilites of the iron ore formation forms the dominant control over the topography of the belt. Practically all the hill ranges and plateaus of this belt are composed of this formation only. The high hill ranges occur in 'U' shaped pattern. The jaspilites form the proto-ore for the large iron ore deposit of the belt. BHJ consists of three members i.e. from bottom to top by coarse and irregular banded jaspilite, fine and even banded jaspilite and chert-shale members.

2.1.3.5 Upper Shale Formation:

The rocks of this banded upper shale formation occupying the core of the IOSG syncline, cover the large areas of the Banai – Keonjhar – Singhbhum belt. This is characterized as marker horizon for manganese mineralization. Below this shale formation no manganese mineralization is reported. In the imagery they are identified by their light gray colour, smooth texture, subdendritic to trellis drainage with medium drainage density, weathered terrain with good landuse practices occupying the valley portion (core of the banded iron formation syncline) and

frequently identifiable features being the manganese mines giving bluish colour in Hyperion data set, (FCC 47, 28, 15)
This formation is made up of alternate band of pink, purple, buff and white shale, which are supposed to be alteration products of black shale. The variegated and weathered shale members are poor in manganese and at times covered with laterite. Also cherts and quartzites have been noticed. The shales exhibit clayey kaolinitic composition inferred to be altered ash beds. The evenly banded nature of the banded shale formation, representing depositions under the quite water condition, give way to features characteristic of stable conditions of deposition, and is reported as mixed facies formation by some workers. The clastic components are represented by silty claystone and fine grained sandstone. The chemical component comprises of rare lenses of dolomite, jaspilite, cherts, manganese and iron ore. Amygdaloidal basic lava and tuffaceous breccia, conglomerate with contemporaneous soft sediment deformational structures are reported in dolomite and chert.

2.1.3.6 Upper Basic Lava:

Along the river Karo, near Barbil these groups have been encountered.

2.1.3.7 Laterite:

An extensive laterite cover varying from 2 meter to 10 meter is found occupying in almost all the rocks. It is a massive cavernous, vermicular and ferrugeneous but when the laterite occurs on manganiferrous shale, the pisolites become manganiferrous.

2.1.3.8 Soil an Alluvium:

Low lying hills, plateaus and river banks are covered with soil cover and alluvium of recent origin, while in the low lying flat valleys in the southern and eastern part of the study area, 3 – 6 meters thick alluvium has been encountered.

2.1.4 Stratigraphy

Based on the lithological details, as described earlier and their associations and characteristics the local stratigraphy has been established as follows.

Upper Basic Lava

Upper Banded shale formation with manganese and cherts etc.

Banded iron Formation

Lower massive shale

Volcanics

Basal sandstone

2.1.5 Geology of Iron Ores

Iron ore occurs as massive and extensive beds occupying definite stratigraphic levels distinct from those pertaining to jaspilite (BHJ). These beds are conformally disposed with respect to other members in a sedimentary sequence to which they physically belong.

The restricted occurrence of iron ore bodies within these Banded Hematite Jasper (BHJ) beds indicate a profound stratigraphic influence over ore localization. The effect of

metamorphism is not significant in the iron ore group. The sedimentological structures such as bedding have been preserved in their original form in iron ore (After A.K. Sen, GSI, 1982).

It is a prevalent notion that the Jaspilite happens to be the parent rock from which residual surficial enrichment of iron minerals, called iron ore bodies, have resulted from mere removal (leaching) of silica by circulating supergene (meteoric) waters.
The iron formation is composed of two distinct rock types.

i. Jaspilite – a banded rock (Banded Hematite Jasper/Quartzite), consisting of alternate bands of Jasper (Chert/silica) and oxide minerals of iron (Hematite/Magnetite).

ii. Hematite – A rock consisting of oxide minerals of iron, with subordinate but variable quantities of iron rich clays and particularly no free silica.

In the just north to the study area near Noamundi and Joda, bore holes have been drilled (A.K.Sen, GSI, 1982), the descending order of stratigraphy, is as follows.

Laterite / Canga : Forms capping over all the members of iron ore formation.

Hard Ore : Finely bedded but compact; sometimes interbedded with soft ore.

Laminated soft Ore : Finely bedded. Occasionally nterbedded with hard ore and or other Types.

Flaky friable : Often interbedded with blue dust.
Blue dust : Often interbedded with flaky friable ore.

Blue dust/or Flaky Ore : Associated with shaly ore.

Shaly ore : Associated with blue dust and/or flaky ore.

Shaly ore and/or Jaspilite : May or may not be present.

Shale/Jasplilte : Often interbedded with blue dust and sometimes with flaky ore.

The distribution and thickness of ore bodies depends on structure, thickest in synformal canoe folds and thinnest in structural high i.e. inverted canoe. The plunge direction and amount are also controlling factors for ore body localization.

2.1.6 Geology of Manganese deposits

Manganese oxide deposits are intimately associated with unmetamorphosed shales (occasionally tuffaceous) and cherts of Pre-cambrian Iron Ore Group (Sarkar & Saha, 1977) in Orissa and Bihar. Thus the Iron Ore Group is the oldest recognizable geological sequence in India and in the world. In the study area the Manganese deposits are confined to restricted belts which are in conformity with major fold pattern. The outcrop pattern of variegated shale and chert member, generally covered with laterite have been observed. Manganese mineralization is restricted to either the shale (Upper) or laterite covering it and chert bands. There seems a very

clear relationship with stratigraphic control. It has been established that the bedded Manganese oxide deposits were the donors of metals during weathering processes. The manganese and other metals from the bedded deposits were taken into solution and remobilized within the weathering profile. During remobilization, separation of Manganese from iron took place. In most cases, the manganese ores in the weathering zones are depleted in iron with respect to their ancestors in the bedded deposits. In some deposits of the Fe-Mn belt (Iron Ore Group) manganese has replaced highly fractured cherts. Inspite of the known occurrences of bedded deposits (in Banded Upper Shale) below the weathered profile, practically most of the production of manganese ores is restricted to supergene remobilized zone. The average composition is as Mn 36.6 – 51.3%, Fe 6 – 16%, SiO_2 – 1.6 – 4.5%, Al_2O_3 1.6 – 4.5 %, P-O0.08 – 0.12% 9 (IBM, Nagpur, 1974).

Chronostratigraphy of the region Koira – Noamundi and surrounding area

KOLHAN GROUP	Newer Dolerite
	Shale
	Limestone
	Sandstone – Conglomerates
----------UNCONFORMITY----------	
SINGHBHUM GRANITE	
IRON ORE OROGENY	
KOIRA GROUP	
(IRON ORE GROUP)	Upper Shales with volcanics
	Banded Iron Formation
	Lower Shale Formation
	Maffic lava and tuffs
	Sandstone and Conglomerates (local)
----------UNCONFORMITY----------	
OLDER METAMORPHIC GNEISSES (>Ca 3200 Ma)	
OLDER METAMORPHIC OROGENY	
OLDER METAMORPHIC GROUP	

2.1.7 Geomorpholgical setup

The study and evaluation of all the landforms is regarded as geomorphology, which solves many geological and environmental issues such as lithological discrimination, mineral and ground water exploration and geological hazards like erosion, mass movement and sedimentation. This also gives an insight into the localization of ore deposits in the region.

In the present study area, in Jamda-koira valley, Keonjhar, Orissa, the role of chemical alteration and disintegration of various rock types result in weathering deposits of iron and manganese in the form of lateritoid deposits. The following geomorphologic units were encountered during the field investigation.

2.1.7.1 Structural hill units

Typical ridge-valley topography is prevalent in the area with doubly plunging folded and faulted structures with hogback landform on BHJ hills, cuesta landform on basal sandstone, and isolated hills on volcanics. In the Banded Hematite Jasper, litho-unit linear hill ridges with high relief, steep slopes, with dark red colour, flat crest, densely vegetated cover are characteristics of hogback landforms.

The linear to curvilinear pattern, bedding with 10-15^0 dip towards NW, low relief, less slope, joint controlled sub-parallel drainage. Alternate ridge valley topography are characteristic of cuesta structures in Basal sandstone.

2.1.7.2 Denudo-structural hill unit

The entire area is covered with highly dissected hills and rugged topography due to weathering and leaching on the hill tops. The laterisation on hill tops occurs generally on Banded Hematite jasper (BHJ) denudational hills, sometimes manganese bearing Upper Shale units. These are the prominent denudational hills in the study area. On the basis of structural and lithological data, this unit can be subdivided nto anticlinal and synclinal hills.

2.1.7.3 Intermontane valley Units

The area is intersected with linear to flat; narrow and wide valleys differentiated as IV1, IV2 and IV3. Based on tonal contrast, landuse, vegetation cover and association, it is very easy to differentiate it from other units. These valleys are subdivided into anticlinal and synclinal valleys, based on lithological and structural interpretation. BHJ comprises of the anticlinal hills, while upper shale forms synclinal valleys. It is formed between the structural and denudo structural hill ranges forming different landforms.

2.1.7.4 Erosional Landforms

Three major types of erosional landforms have been identified in the study area. They are the 1. Residual hill unit 2. Weathered hill slope unit and 3. Pediplain surface unit.

2.2 Study Area 2. (Udaipur)

Col. James Tod (1829) described the valley of Oodipoor (Udaipur), the most diversified and most romantic spot on the continent of India. Udaipur city is within the Girwa Tehsil of

Udaipur district. The name Girwa denotes a basin like land morphology wherein water flows from the surrounding hills (Gir = hills, Wa = flow of water).

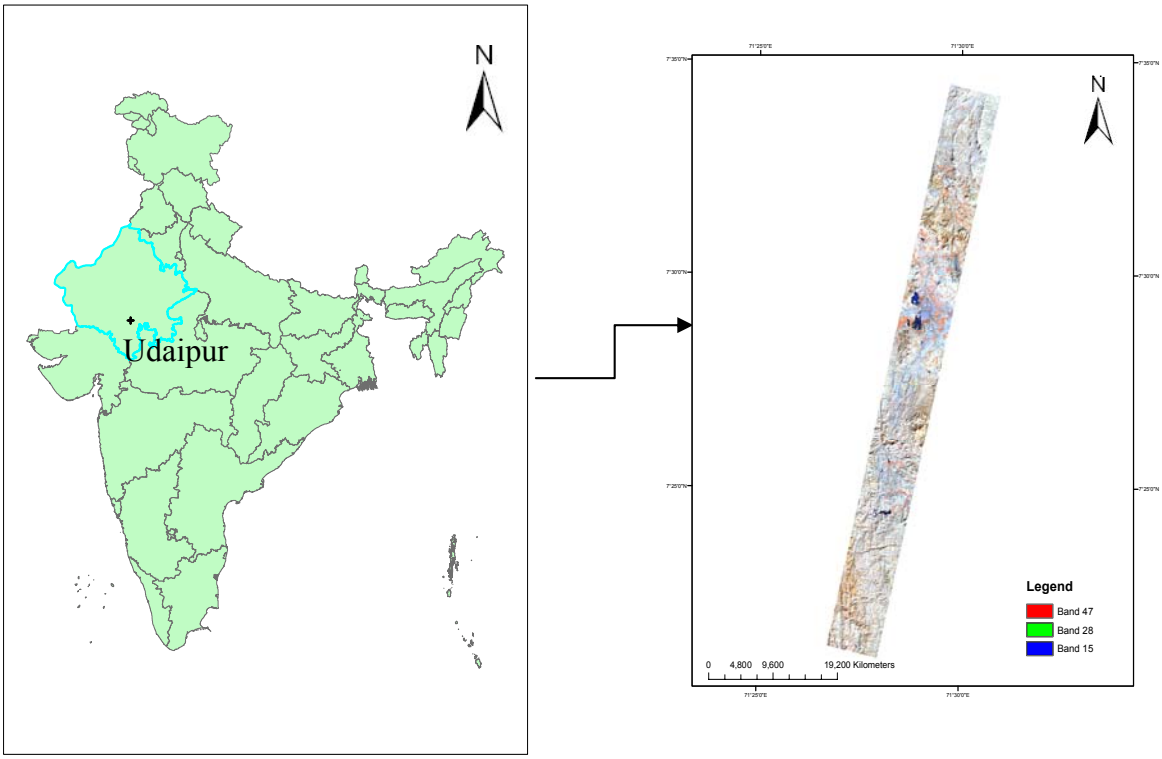

Figure 2.3 Study area (Udaipur), Hyperion (FCC 47 28 15)

2.2.1 Physiography and climate

Physiographically, Udaipur has undulating and rocky topography with high and low hills. The city is surrounded by the hills of Aravalli ranges of various heights. The important hills within the area are:

Northern hills: Nimach Mata Hill (767 m), Bhuwana Hill (708 m).

Southern hills: Balicha Hill (636 m), Odi Hill (688 m).

Eastern hills: Eklingpura Hill (683 m), Chorbavari Hill (769 m).

Western hills: Thoria Hill (756 m), Machhala Magra (753 m), Sajjangarh Hill (936 m).

Besides these, the area also has depressions in form of lakes like Pichola, Fatehsagar, Rangsagar, Swaroopsagar and Goverdhanvilas-ka-Talab etc. The area has 234 water bodies The River Ayar flows diagonally in the area from northwest to southeast direction.

Udaipur has a semi-arid climate, which prevails over most of the year. It has a hot dry summer and bracing cold winter. The cold season is generally from November to February and is followed by the summer season from March to June. The southwest monsoon follows from last week of June to the mid September. In the area, 90% of its total rainfall occurs during June to September period. July and August are the wettest months of monsoon. The average annual rainfall for the area is 640 mm and average number of rainy days is 42. The annual rainfall for last 100 years ranges from 300 mm (1936) to 1133 mm (1973), with the coefficient of variability of rainfall (C.V.%) being 42%. The annual potential evapo-transpiration values in the area ranges from 1300 mm to 1400 mm.

2.2.2 Existing land use

An estimated distribution of existing land use categories is as follows:

1. Forest land use including land under trees (~7%).
2. Agricultural land use including cropland, orchards (16%).
3. Residential and Mixed land use including commercial, hotels, institutions, etc.(39%)
4. Industrial land use (10%).
5. Recreational land use including Parks and Zoo (2%).
6. Surface water bodies including lakes, streams, nallas (8%).
7. Unclassified land use (including wasteland, uncultivable land (18%).

Rapid change in land use is one of the important geo-environmental issues that demand attention in the area. It is noted that in last two decades the urban development activities in the area have grown at a high rate, resulted in the rapid but unplanned development of residential as well as industrial areas. This development directly influenced the agriculture and forestland.

2.2.3 Slope

The average slope data analysis reveals that in Udaipur area the average slope angle varies between 00 to as high as 17°. The slope Uniform slope is noted in N-E direction near Bari and Nimachmata area. Concave slopes are observed near Sajjangarh, in western side of area. Convex slope occurs at the Machhla Magra and Bhuwana Hills sites. In the rest of the elevated area i.e. to the southwest sites and northwest sites the slope are undulated type.

2.2.4 Pedology

The hills and ridges of the area are mostly covered by the rock outcrops associated with very shallow, well-drained, skeletal soils occurring on slopes and are prone to severe soil erosion. The soils on the foothill and highlands are shallow to moderately shallow, well drained, loamy in texture and moderate to severely prone to erosion problem. The texture of these soils varies from sandy loam to clayey loam. The soil of the area can be classified as Ustochrepts Group. Broadly, the soil of the area can be grouped into four types:

A. **Hill soils:** Found on and around the main hills in the area. The color of soils varies from yellow to brown and red. Presence of stones and lithic fragments is commonly observed in these soils.
B. **Alluvial soils:** Found along the Ahar river. Significant deposits of alluvial light brown to yellowish soils are found around Ayad and Pahara.
C. **Red soils:** Found in high lands and plain area of the regions and are dark brown to reddish brown in color.
D. **Brown soils:** Occupy low grounds in plains. It is yellowish brown to light brown in color.

The soils of the area are saline to alkaline and have normal EC values, low potash and phosphate concentration (accept the soil near Bargaon). The organic carbon content shows wide variation having medium to high organic carbon status.

2.2.5 Geological setting

The geological setting of Udaipur area is not only unique in the state but also shows wide complexity. It is considered as one of the "type area" of the Aravalli Super group of rock.

The study area broadly has two main stratigraphic units i.e. rocks of Aravalli Supergroup and pre-Aravalli Formations Aravalli Supergroup of rocks around Udaipur city show a high degree of structural complexity and polyphase deformation history. However at some places (near Fatehsagar) the graywacke and phyllite rocks have escaped the severity of metamorphism and deformation and display some typical sedimentary characters like ripple marks, mud cracks, rain prints etc.

Table 2.1 General Geological Succession of Precambrian Formation of Rajasthan (after Heron, 1953) (source: Department of Geology, MLS University, Udaipur)

	Recent & Sub recent	Alluvium and blown sand	
	Vindhyan System	Sandstone, limestone & boulders	Dolerite and basalt (age uncertain)
	Malani Rhyolites	Rhyolite, tuffs	Granite, ultrabasic rock Erinpura granite, pergmatite, aplite Epidiorite and hornblende schist
Delhi System	Ajabgarh Series	Upper phyllite Limestone Biotitic limestone and calc-schist Phyllites, biotite schist and composite gneiss	

	Alwar Series	Quartzites Arkose, grit and conglomerates	
	Raialo Series	Garnetiferous biotite schist Limestone (marble) Local basal grit	Aploganite, epidiorites and hornblende schists, ultrabasics
Aravali System		Impure limestone, quartzites, phyllites, biotite-schist, composite gneiss	
		Quartzites, grits and local soda-syenites, conglomerate	
		Local amygdaloids and tuffs	
	Banded Gneissic Complex (BGC)	Schists, gneisses and composite gneiss	Pegmatites, granite, aplites and basic rocks
		Quartzites	

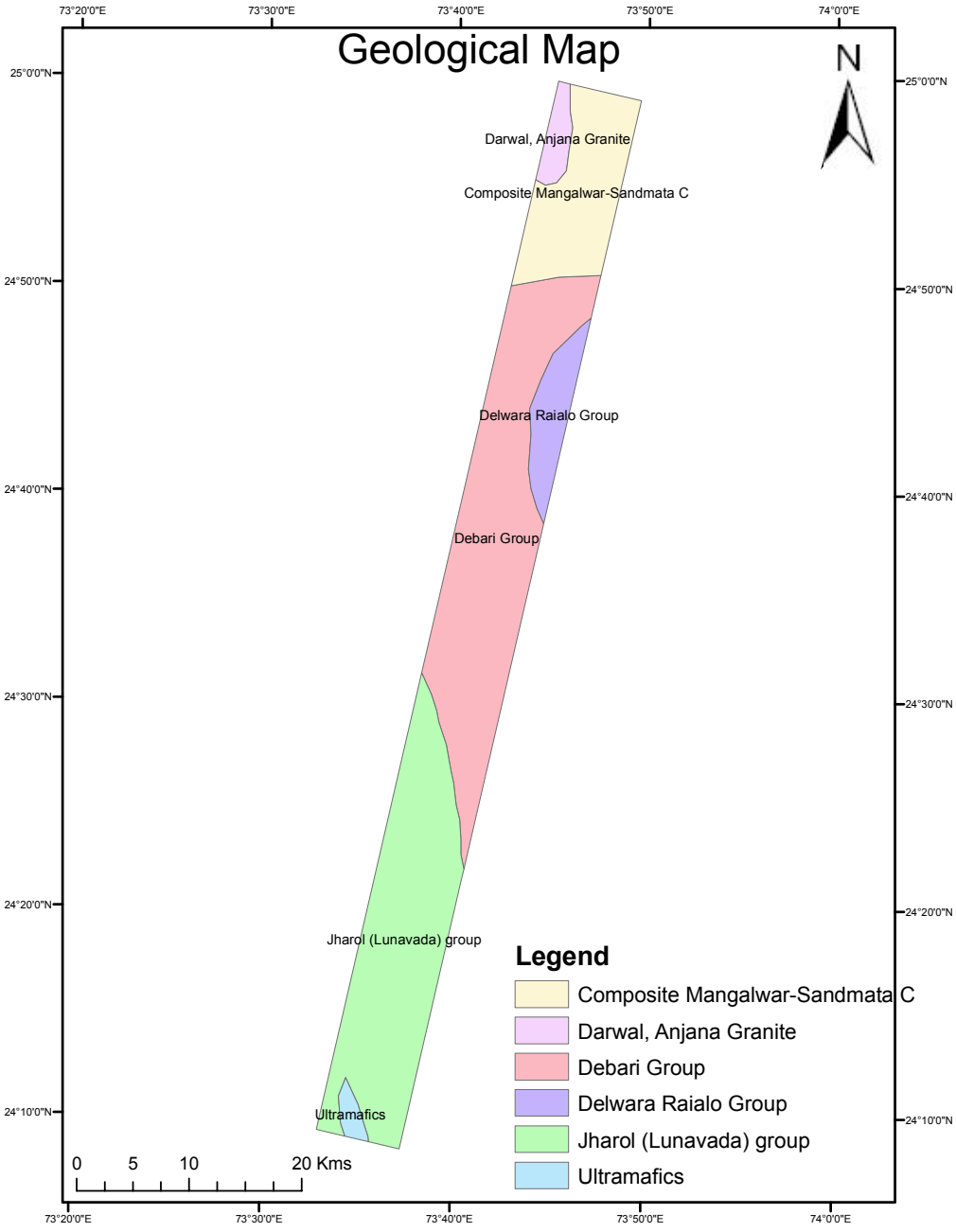

Figure 2.3 Geological map of Udaipur study area Modified after S.Sinha-Roy, G. Malhotra, M. Mohanty (Geological Society of India)

Udaipur, the capital of a princely state of pre-independence time is perhaps the only place in India where artists, historians tourists, naturalists, geoscientists get a lot to fulfill their interests. Glorious history of Mewar echoing from all corners on one hand and the scenic beauty of the city and still waters of its fascinating lakes surrounded by Aravalli hills on the other stun a visitor. Rocks carving this blissful valley easily turn a geoscientist into a philosopher. Time has put its magnificent signatures on the rocks of this fascinating valley and its surrounding environs. The

oldest rocks, perhaps, the remnants of the primordial crust, the Mewar Gneiss popularly known as the Banded Gneissic Complex with pockets of paleosols (that altered to fine'-grained, talcose white mica) form a flat terrain at the eastern entrance of the city: Basement rocks also crop out between Neemach Mata and Bari Lake and around Titari and Udai Sagar areas. At the foot hill side of Neemach Mata, the basement granite shows metasomatized remobilization making its contact with the cover rocks quite interesting. In fact, all these granitoid bodies were considered by earlier workers to be intrusive into the Aravalli rocks. Surprisingly, the boundaries of the amphitheater encircling the historic town form the replica of the epicontinental sea in which the sediments of the Aravalli Supergroup, divisible into Lower, Middle and Upper Groups, were deposited about *two* and a half billion years ago. The two high ridges, Iniamagara-Sajjangarh in the west and Debari in the east, that include *two* linear "outliers of Delhi Formations" (now considered part of the Aravalli Supergroup) and define the limits of the Udaipur valley; have emerged at the same place where the *two* deep seated liastric faults, that had develop during the beginning of the Aravalli basin formation, out poured basic lava. All along these ridges basic volcanic with vesicles and pillow structures are spread in the form of green schist that is noticeable east of Debari Zinc Smelter, Bari Lake and at the northern termination of Iniamagara. Sedimentation of Aravalli rocks began with dumping of large assorted blocks in the basic lava along the margins of the graben so formed. Diamictites of the Lower Aravalli Group so formed are exposed along the hills to the east of Debari Zinc Smelter, to the south of Nandeshwer and in a river section at Koriyat. Tuffaceous material associated with the lava can easily be seen displaying paper-thin laminations and micro grading along the Koriyat-Nai section. Around Koriyat the basal volcanics have been observed to be interlayer with carbonates. The basal sequence of coarse and fine clastics, represented by conglomerate, quartzite; phyllite is exposed on the either sides of Udaipur valley: Most of the high ridges around Koriyat, Bari, Nai and Undri on western side and Udai Sagar, Debari, and Girwa on the eastern and northern sides represent these lithounits. These linear outcrops of conglomerate-arkose-quartzite sequence, exposed on either sides of the Udaipur valley, were thought to be the "outliners" of Delhi "System" (now Supergroup) by earlier workers(Heron, 1953) .This interesting coarse clastic sequence to the east of Udaipur City, popularly known as Debari Formation, has seen several ups and downs during the history of geological research in the area. Banerjee (1971) , dividing the Aravalli rocks in to Debari, Maton, and Udaipur Formations, assigned it the lower most position in the sequence. On the other hand Roy and Paliwal (1988) equated this sequence with the greywacke-phyllite sequence of Udaipur Valley Formation-C. This sequence suffered a lot of oscillation in its stratigraphic position in subsequent publications. Similar sequence, popularly known as lniamagra sequence is exposed around Koriat, Bujara, Undari etc. to the west of Udaipur city has retained its basal status. Good exposures of the basal sequence are seen in sections along the road connecting Udaipur City with the Maharana Pratap Airport particularly around Debari tunnel and Zinc Smelter. The diamictite with large rounded boulders exposures are seen at Nandeswar on way to jharol, in river sections at Bujara, Sajjangarh and Koriyat and at Bari Lake where basic volcanics, now altered to green schist, show well preserved vesicular and amygdular structures. In a ridge west of Sajjangarh an outcrop of banded hematite quartzite has been noticed. The Basal sequence of coarse clastics passes upward into a carbonate sequence comprising dolomites, ortho-quartzite, stromatolitic phospharite and carbonaceous phyllite. Perhaps it was the time when the source area reached peneplanation and the weathering and erosional agencies calmed down. Chemicals started precipitating and carbonates got deposited in the epicontinental sea. Of course in deeper trenches, with reducing environment owing to profuse development of micro-organisms, black shale was deposited to give rise the carbonaceous phyllite. Uraniferrous carbonaceous phyllite has been located around Umra, hardly a few km, east of Udaipur. In a road cutting near Berwas (Pratapnagar) carbonaceous phyllite can be seen on way to Debari Zinc Smelter (where Zinc from Zawar group of mines, located about 50 km southeast of Udaipur, is smelted). Carbonate with algal stromatolites, both phosphatic and non-phosphatic, forms a marker

horizon in the Aravalli Supergroup of rocks exposed in its type locality around Udaipur. In fact, blue-green algae grows profusely up to a depth of 30 meters (a depth to which sunlight can penetrate) effectively for the photosynthesis. The prolific growth of the algae together with other microbiota gave rise to a large variety of algal stromatolite in carbonate(s) deposits encircling Udaipur valley, particularly around Sisarama, Neemach Mata, Bargaon, Kanpur, Kharbaria-Ka-Gurha, Maton,]hamarkotra, and Dakankotra. At Jhamarkotra and Maton, hardly a few km west of Udaipur, the rock phosphate is being exploited commercially for fertilizer industry. Other prospects, of low-grade ore, may prove to be of economic significance in future. While enjoying boating in the Pichola Lake, phosphorite bearing carbonate hills of Sisarama can be viewed forming silhouette, which gives the Lake Palace a look of an iceberg with a smoky cloud in its background. Some geoscientists believe that rocks of the Udaipur area show a constant westerly younging and therefore the carbonates with phosphorite on either sides of the city form two separate stratigraphic horizons. Prolific development of blue-green algae in the epicontinenteal sea contributed a lot of oxygen to the atmosphere through photosynthesis through out the world. It is believed that our atmosphere lacked oxygen prior to the development of the blue-green algae in the seawater. A variety of stromatolites, the structures produced by these algae, are seen at a number of places around Udaipur City: In addition to a well preserved stromatolite park at the H-block of Jhamarkotra, these deformed and undeformed stromatolites. (http://www.geolmlsu. org/geology.html)

2.2.5.1 Banded Gneissic Complex

The basement rocks in Rajasthan occur in an arcuate terrain between the Aravalli hill ranges in the west and the Vindhyan plateau in the east. The Gneissic complex has the shape of a V with its apex pointing westward and its northern limb bounded by the Delhi fold belt and the southern limb by the Aravalli fold belt.

The Banded Gneissic Complex (BGC) in Rajasthan can be divided into three major rock groups, i.e. Mangalwar complex, Sandmata Complex and the Hindoli Group. The BGC in Udaipur and its surroundings can be grouped under the Mangalwar and the Sandmata Complex. The mangalwar complex is a heterogeneous assemblage of amphibolite-facies metamorphites comprising of mignmatites, composite gneisses, feldsparthic mica schist, sillimanite-kyanite-mica-schist, hornblende schist, granite gneiss and amphibolite along with minor carbonates constitute the Mangalwar complex (Gupta et.al. 1981). The Sandmata Complex are the high-grade metamorphites, comprising of migmatites, composite gneisses, biotite-schist, garnet-sillimanite-staurolite-biotite schist, dolomitic marble, hornblende schist with associated granite, are included in the Sandmata complex. The boundary between the Sandmata Complex and the Mangalwar Complex is marked by isograd roughly along the Delwara Lineament. Sinha-Roy et al. (1992) suggested that the Sandmata Complex constitutes only the high pressure granulite facies rocks having tectonic contact with the encompassing Mangalwar complex rocks.

2.2.5.2 Debari Group

The lithoassemblage comprising coarse clastics, carbonates and pelites constitute the Middle Aravalli sequence and is designated as the Debari Group Sinha-Roy et. Al. (1993b).

The shelf-facies Aravalli sequence is punctuated by a prominent polymictic conglomerate which separates the Delwara Group at the base and the Debari group at the top. The polymictic conglomerate-arkose-grit-quatrzite horizon, ocuring as a linear band from Kailashpuri in the north

to Banswara in the south, is an important stratigraphic marker horizon which marks the base of the Debari Group and is designated as the debari conglomerates. The stratigraphic positon of the thick carbonate sequence above the Debari Group has been described differently by various workers. The dolomite unit containing phosphoritic stromatolites occurring at Jhamarkotra, Matun, Kanpur, Badgaon and Sisarama either overlies the basement rocks with an intervening thin arkosic conglomerate or unconformably overlies the Delwara Group rocls. The overlying Umra formation containing carbon phyllite is best developed at Umra, and is also well developed at Parsad, Sisarama, Nerach, Jahamarkotra area as a facies variant of dolomite. It contains Cu-U mineralization Roy et al (1988). The lithosequence comprising greywacke and phyllite is best developed around Udaipur, and hence it is designated as the Udaipur Formation Sinha-Roy et. Al (1993b). It shows the extensive development in Nathdwara and Dungarpur areas constituting the bulk of the shelf-facies rocks. The rhythmic sequence of Greywacke-slate/phyllite laterally passes into lithic arenite as at Jhamarkotra. The Udaipur Formation is overlain by a carbonate sequence hosting Pb-Zn mineralization at Zawar and Katar, and is designated as the Zawar Formation Sinha-Roy et al (1993b).

2.2.5.3 Delwara Group

The Aravalli Supergroup can be divided into two principal facies sequences. One is the Delwara group which are volcanic dominated and the volcanics free Debari Group.

The Delwara group occupies the lowermost position in the Aravalli stratigraphy. It comprises of mafic volcanics, clean-washed quartzite, quartz pebble conglomerate (QPC), minor carbonates and BIF.

2.2.5.4 Jharol Group

The carbonate free and pelite dominant sequence with arenite bands constitute a large part of the Aravalli sequence and it is named as the Jharol Group Gupta et al (1981). It is interpreted as distal turbidities or flysch of the Aravalli deepsea sequence. The rock sequence comprising of coarse pelitic schist and quartzite with phosphoritic dolomite that occur in a roughly polygonal area in southern Rajasthan is referred to as Lunavada Group.

2.2.5.5 Ultramafics

Ultramafic rocks represented by serpentinite, talc-tremolite schist, antigorite-tremolite schist and monomineralic chloro-schist occur along two regional lineaments, i.e. Rakhabdev Lineament in the east and Kaliguman Lineament in the west Bakliwal and Ramaswamy, (1987). Although these bodies occur as lenses and linear bands of variable dimensions, their disposition marks a linearity. These Ultramafic rocks were variably described as ‘Magnesian rocks’ (Middlemiss, 1921) and as ‘talc-serpentine-chlorite rock’ Ghosh(1933). Based on the field and petrochemical studies Gathania et al. (1995) divided the Ultramafics into three groups; the first group consisting of coarse grained carbonate-talc dominated rock occurring near the contact with the metasediments, while the second group consists of dark coloured antigorite-chlorite bearing rocks, while monomineralic chlorite rich forms the third group. The latter occurs as intrusive bodies within other ultramafic groups and metasediments.

The above mentioned facts regarding the geologic setting of Udaipur study area have been referred from “Geology of Rajasthan” by S. Sinha-Roy, G. Malhotra and M. Mohanty, Geological Society of India, Bangalore, 1988.

The following chapter deals with the materials and the methodology adopted for the present study.

Chapter 3

Materials and Methods

The methodology for the present study has been formulated by keeping in mind the primary objectives of the work. During the literature review for the present study it came to the limelight that very few works have been conducted in the field of hyperspectral remote sensing in India which could assist our efforts for the present study. This stood as a great challenge and a factor of inspiration for the study. The methodology adopted for the present study is given below as a flow chart.

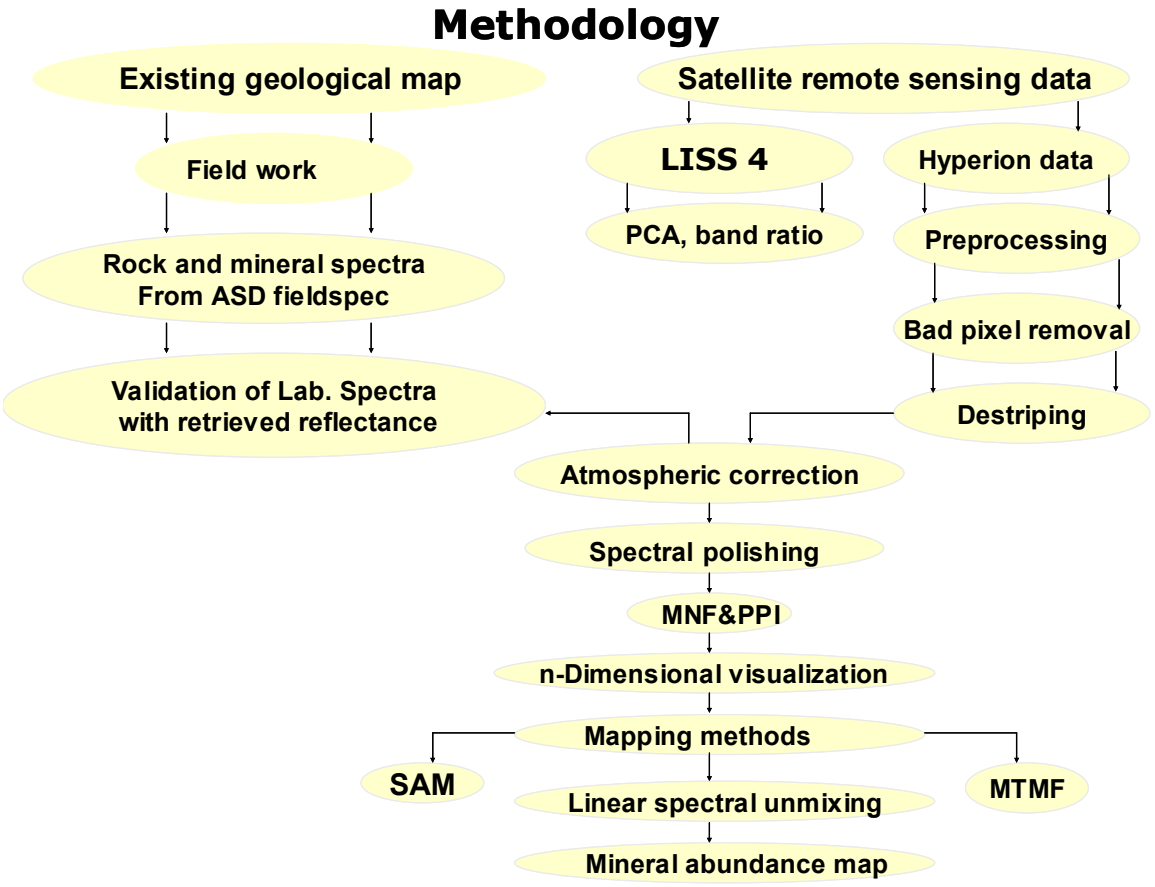

Figure 3.1 Methodology flow chart for the present study

3.1 Materials and Data

The materials and methods used in this research work are discussed in detail in the following sections.

3.1.1 Hyperion satellite data

The primary satellite data that has been used for the present study is the Hyperion data set. Hyperion sensor is a hyperspectral imager on-board of EO-1 satellite. There are 220 spectral

bands ranging from 400 – 2500 nm. The spatial resolution is 30 meter per pixel and swath width is 7.7 km. Each scene covers either 42 km, or 185 km. The product is distributed by USGS, and the level one product, which is only radiometrically corrected, is available. The EO-1 satellite was launched on November 21, 2001 as part of a one-year technology validation/demonstration mission. After the original EO-1 mission was successfully completed in November 2001, the remote sensing research and scientific communities expressed high interest in continued acquisition of image data from EO-1. Based on this user interest, an agreement was reached between NASA and the USGS to allow continuation of the EO-1 Program as an Extended Mission (Pearlman, et al., 2003; USGS, 2004a). The Hyperion satellite data was ordered from the USGS Earth explorer website and it was delivered within two months.

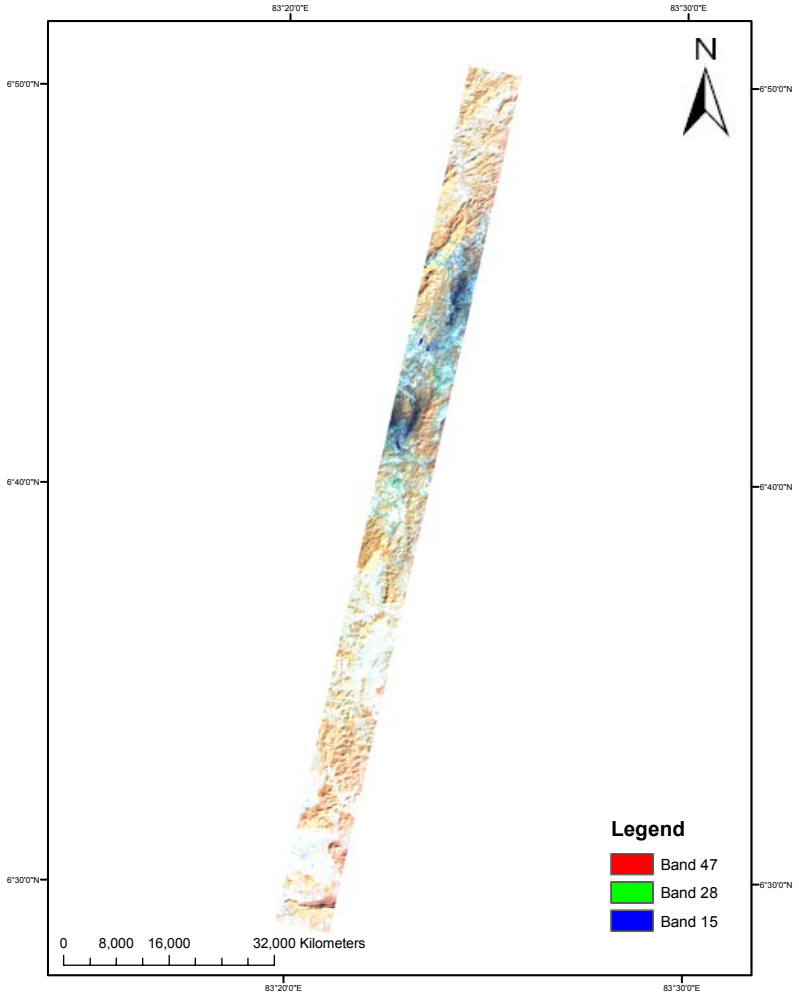

Figure 3.2 Hyperion strip of Orissa study area (FCC 47 28 15)

The metadata information for the Jamda-Koira Hyperion scene is given below.

Dataset Attribute	Attribute Value
Entity ID	EO1H1400452006016110PF_SGS_01
Acquisition Date	2006/01/16
NW Corner	22°23'34.50"N, 85°23'32.24"E
NE Corner	22°22'42.02"N, 85°27'55.77"E
SW Corner	21°18'17.31"N, 85°08'36.68"E
SE Corner	21°17'25.05"N, 85°12'58.23"E
Image Cloud Cover	0 to 9% Cloud Cover
Receiving Station	SGS
Scene Start Time	2006:016:04:30:43.205
Scene Stop Time	2006:016:04:31:02.205
Date Entered	2006/01/17
Target Path	140
Target Row	45
Orbit Path	140
Sun Azimuth	144.141461
Sun Elevation	38.450226
Satellite Inclination	98.21
Orbit Row	45
Look Angle	-6.984
Browse Available	Y

Figure 3.3 Metadata of Orissa hyperion dataset (Source: http://glovis.usgs.gov)

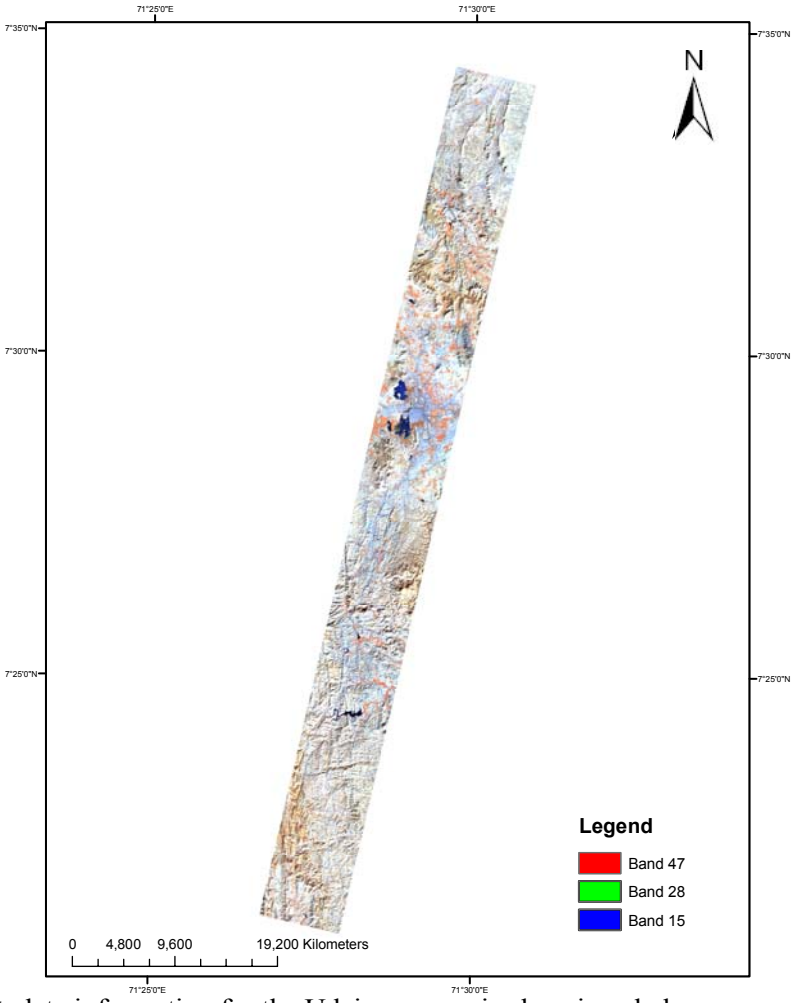

Similarlly the metadata information for the Udaipur scene is also given below.

Dataset Attribute	Attribute Value
Entity ID	EO1H1480432004019110PZ_SGS_01
Acquisition Date	2004/01/19
NW Corner	24°54'46.83"N, 73°44'13.48"E
NE Corner	24°53'52.78"N, 73°48'39.36"E
SW Corner	24°07'48.56"N, 73°32'51.51"E
SE Corner	24°06'54.75"N, 73°37'15.77"E
Image Cloud Cover	0 to 9% Cloud Cover
Receiving Station	SGS
Scene Start Time	2004:019:05:22:10.546
Scene Stop Time	2004:019:05:22:24.546
Date Entered	2004/01/29
Target Path	148
Target Row	43
Orbit Path	148
Sun Azimuth	145.987318
Sun Elevation	37.214824
Satellite Inclination	98.24
Orbit Row	43
Look Angle	-.4642
Browse Available	Y

Figure 3.5 Metadata of Udaipur hyperion dataset(Source: http://glovis.usgs.gov)

3.1.2 LISS IV Satellite Data

LISS IV satellite data has been procured for both the study areas and were used as a validation tool as well as to highlight the importance of hyperspectral dataset for mineral exploration. The LISS IV band specifications as well as the metadata of the dataset used is given below.

```
Satellite ID                :P6
Sensor                      :L-4
Path-Row                    :203-004
Date, Time and  Scene Id.   :07-FEB-05 05:51:40L4X ST00B234 F
Product Code                :STPC0026J
Orbit Number                :6807
Image Layout                :BIL
Number Of Bands             :3
Bands Present in Product    :2 3 4
Bands in this volume        :2 3 4
File Header                 :540
Line Header (Prefix Bytes):32
Line Trailer(Suffix Bytes):0
Scan Lines                  :5279
Pixels                      :4947
Image Record Length(Bytes):4979
```

The liss 4 images for the two study areas are given below in figure 3.6 and 3.7

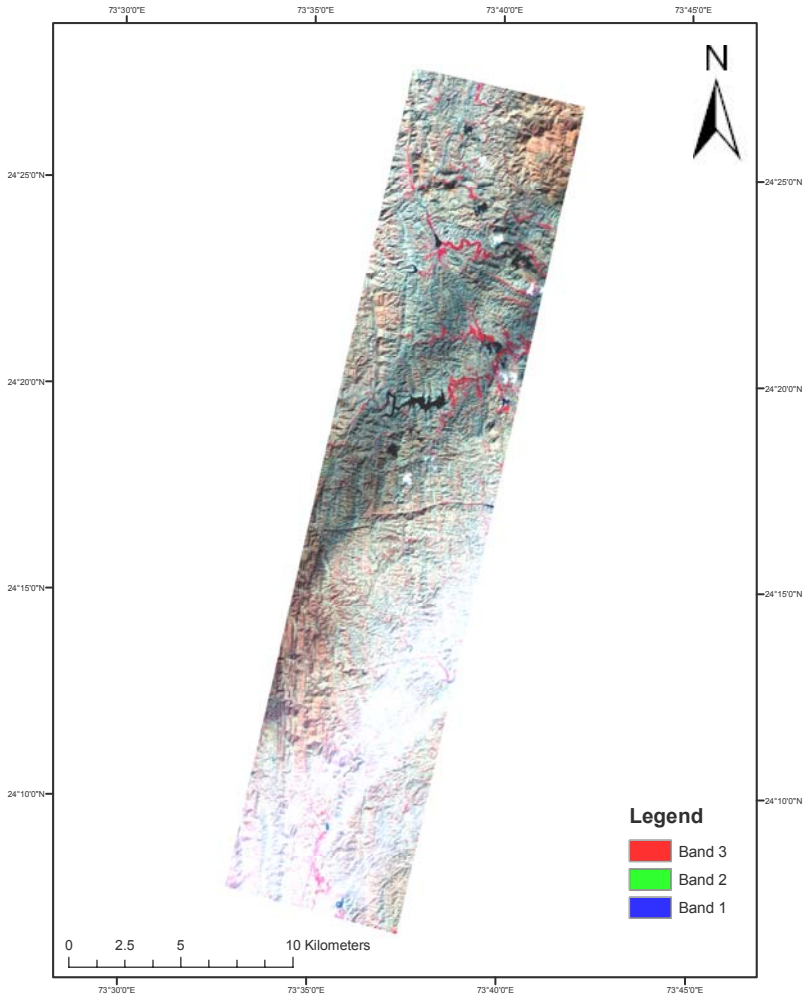

Figure 3.6 LISS 4 image of the Udaipur study area

The band wise spectral characteristics of the LISS 4 is given below.

Table 3.1 Band specification of LISS 4(Source: http://geo.arc.nasa.gov/sge/health/sensor/sensors/irsp6.html)

Band	Wavelength region μm	Resolution
2	0.62 – 0.68	6
3	0.77 – 0.86	6
4	1.55 – 1.70	6

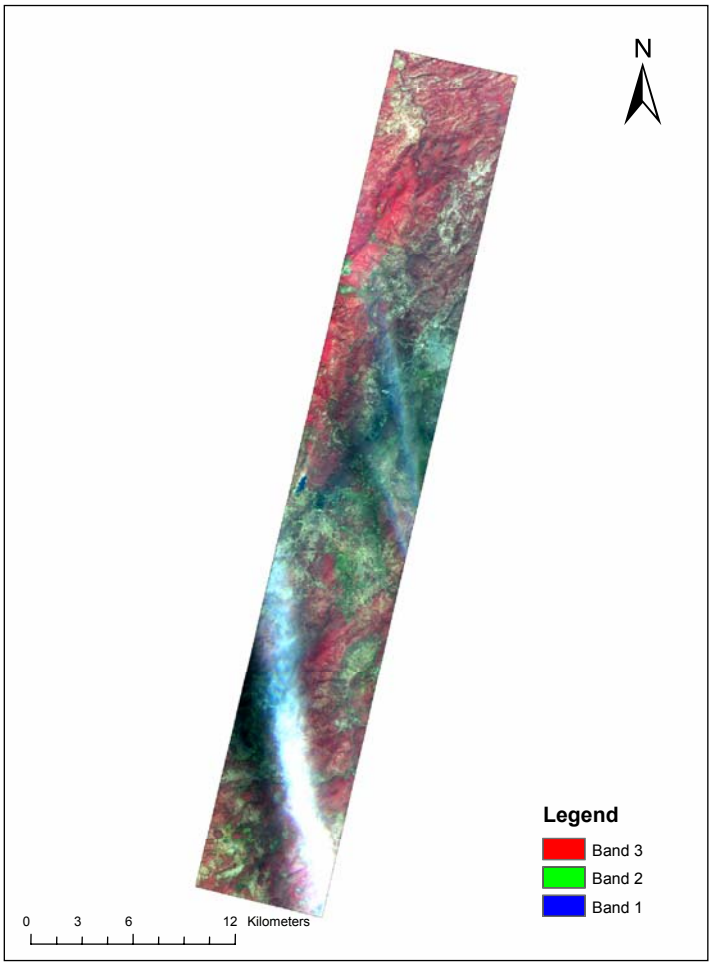

Figure 3.7 LISS 4 image of Orissa study area

3.2 Hyperion data file

There are five files coming with the distributed scene. They are as shown in the below figure as seen in the ENVI software.

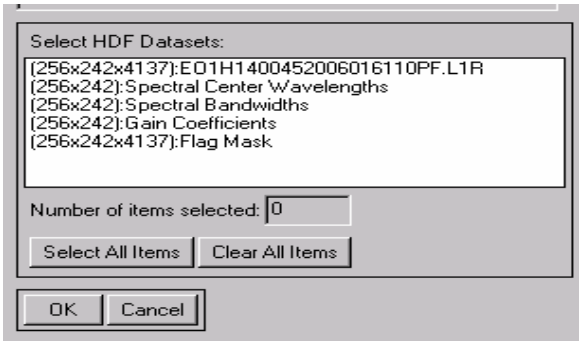

Figure 3.8 Primary Hyperion dataset delivery files

The first file is the Hyperion satellite data file (L1R) followed by the spectral center wavelength file, which gives information about the central wavelength value for each bands in the Hyperion data set. The spectral bandwidth file gives information regarding the bandwidths of each bands (220 bands) present in the data set. These files are followed by the gain and offset value information for each bands.

3.3 Data importing

The distributed image file in the CD is in the standard hyperion L1R data format. This L1R data format is been imported to the Hyperion-ENVI standard hdr format. This is done by customizing the ENVI tool bar using the Hyperion import file which has been downloaded from the ITT website.

3.4 Preprocessing of hyperspectral data

Processing of high dimensional hyperspectral data is a challenging task and the computational complexity is a result of vast data volume in numerous spectral bands. Since Hyperion sensor operates from a space platform with modest surface signal levels and a full column of atmosphere attenuating the signal, the data demand careful processing to manage sensor noise. The errors are said to be caused due to calibration differences in the detector array (Goodenough et al., 2003). The Hyperion dataset has to be corrected for abnormal pixels, striping and smiling prior to the atmospheric correction. Pre-processing of hyperspectral images is required not only for removing sensor errors during acquisition but also for display, band selection (to reduce the data dimensionality) and to reduce computational complexity.

3.4.1 Spectral subsetting

The Hyperion sensor covers the visible and near infra-red (VNIR, or 400 nm to 1000 nm) and shortwave infra-red (SWIR, 900 nm to 2500 nm) ranges. The instrument has a single telescope but two spectrometers – one for the VNIR and the other for the SWIR data. The VNIR spectrometer has 70 bands and the SWIR 172 bands providing 242 potential bands which are normally about 10 nm apart in each spectrometer and have spectral response functions with approximately 11 nm full-width at half maximum (FWHM). If every band were operating, the spectral range covered would be from 356 nm to 2577 nm with a common area of overlap between the spectrometers between 852 nm and 1058 nm. In practice a number of the bands were not illuminated and others correspond to areas of low sensitivity of the spectrometer material so that of the 242 a subset of 198 bands spectrally subsetted from the hyperion data set.

VNIR Range : Bands 8-57 (436-926nm)
SWIR Range : Bands 77-224 (892-2406nm)

This results in 198 useable channels or bands with 196 unique wavebands and 2 pairs of channels remaining in the overlap between the two main detector sets. It is usual to disregard the SWIR overlap bands (77-78) as their SNR is slightly lower than their VNIR equivalents. The overlap is kept mainly to check caliberation. Hence the redefined spectral ranges of the hyperion image set is as follows.

VNIR Range : Bands 8-57 (436-926nm)
SWIR Range : Bands 79-224 (933-2406nm).

This datset now provides the basic 196 unique data channels that will be further used as a base set of unique hyperion bands.

3.4.2 Destriping of VNIR and SWIR region

A vertical stripe is said to occur where the statistics indicate that the image information is likely to be valid, ie. the pixel is not bad but have significantly modified gain and offset. In a pushbroom sensor, a poorly calibrated detector in either VNIR or SWIR arrays leaves high frequency errors ("vertical stripes") on the image bands. In Hyperion striping pixels have been classified in four categories: i) continuous with atypical DN values, ii) continuous with constant DN value, iii) intermittent with a typical DN values and iv) intermittent with lower DN values. The first two categories of stripes are the most extreme type as they contain very little or no valid data about the ground feature (Goodenough et al., 2003). In the level1R product these stripes are left unmodified, allowing the users to handle or replace the pixels as per the requirement. In order to facilitate extraction of calibrated spectra from Hyperion dataset it is significant to carefully balance for the striping in the dataset. In the present study a tool was developed to compensate for the striping by visually identifying bad columns and develop a filter to balancing for the bad columns.

3.4.2.1 Identification of bad columns

In order to compensate for striping in Hyperion datasets global and local de-striping approaches have been suggested. In the present study the bad columns were identified visually to avoid enforcing severe change in the spectra. A total of 36 bad columns were identified in 13 VNIR bands of Udaipur dataset and 48 bad columns in 16 VNIR bands of Spain dataset. SWIR bands were found devoid of visible stripes. Table 3.1 lists the detected bad columns in Udaipur and Orissa datasets.

Table : 3.2 Location of detected bad columns in L1R product of Udaipur and Orissa scene

Band	Bad Column in Udaipur	Band	Bad Column in Orissa
8	6, 68, 114	8	6, 68, 114, 167, 187, 238, 247
9	6, 68, 114, 246	9	6, 68, 114
10	6, 114, 119	10	6, 114, 199
11	6, 114, 119	11	6, 114, 199
12	114	12	6, 114
13	114	13	6, 114
14	114	14	114
15	114	15	114
16	114	16	114
54	13	17	114
55	13, 17, 20	18	114
56	8, 13, 17, 20, 32, 37, 39	19	114
57	8, 13, 17, 20, 33, 36, 38	20	114
		21	114
		22	114

		27	47
		28	47
		56	17, 20, 32
		57	13, 40
		79	186, 254
		80	188, 246
		81	248
		82	242

3.4.2.2 Balancing for bad columns

A bad column removal filter was developed to target the bad columns in each band. The bad columns were replaced by the 3×3 neighbourhood mean, without taking into account the bad column value. In order to implement this a 3×3 filter was designed with positional values as (-1,1) =1, (-1,0) =1, (-1,-1) =1, (0,1) =0, (0,0) =0, (0,-1) =0, (1,1) =1, (1,0) =1 and (1,-1) =1. The filter runs on the bands identified as containing bad columns. The user interface allows the user to enter the band numbers that contain bad columns and column number of the specified band.

1	0	1
1	0	1
1	0	1

Figure 3.9 Filter design for local de-striping of Hyperion dataset

The values of the image data for sample (bad column) *i*, line *j*, and for band *k* (x_{ijk}) are modified to

$$\sum_{j=1}^{n}((x_{i-1,j,k})+(x_{i+1,j,k}))/2n,$$

Where

i = identified bad column

n = total number of rows in the predefined filter

3.5 Atmospheric correction of the datasets

Two atmospheric correction models were used in the present study for the retrieval of reflectance from radiance. There are certain inputs that need to be generated for both the atmospheric correction models (FLAASH an ATCOR2). The input parameters required for ATCOR2 and FLAASH are to be computed before the image is subjected to atmospheric correction. The parameters required from the user to run the two models successfully are sensor specific and specific to ground situation. Table 3.2 shows the list of input parameters required by the two atmospheric correction models. Selection of the input parameters has a direct bearing on the output of the atmospheric correction models. The parameters selected for atmospheric correction of the datasets is discussed here based on the user manual of the ATCOR and FLAASH.

Table 3.3 Input parameters for ATCOR2 and FLAASH

ATCOR2 parameters	**FLAASH parameters**
Sensor type	Sensor type
Pixel size	Pixel size
Ground elevation	Ground elevation
Solar Zenith angle	Scene centre Latitude/Longitude
Visibility	Sensor altitude
Flight date	Visibility
Atmospheric file	Flight date & flight time
Adjacency range	Atmospheric model
Zones	Aerosol model
Region for water vapour	Water vapour retrieval
Water vapour absorption	Spectral polishing
Haze removal	Wavelength calibration
Shadow removal	**Advanced parameters**
Reflectance scale factor	Output reflectance scale factor
Value added product	MODTRAN resolution
Index map	MODTRAN multi scattering model

3.5.1 Generation of scale factor as ASCII files

The scale factors for the VNIR and SWIR bands are 400 and 800 respectively in the case of nanometers (nm) while 40 and 80 for micrometers (μm). They are written in the notepad file from top to bottom in a single column with the number of rows corresponding to the number of bands in the dataset.

3.5.2 Sensor type

The option of selecting sensor type is provided to the user as both ATCOR2 and FLAASH are used for wide range of sensors. Sensor type, for the present study is selected as Hyperion.

3.5.3 Pixel size

The Hyperion data ordered to EPGS was specified as nadir looking product. Therefore the pixel size selected is 30 meters, as per the data description of Hyperion.

3.5.4 Ground elevation

Ground elevation input required by ATCOR2 and FLAASH is an average elevation of the imaged terrain. For Udaipur the average elevation of the imaged terrain was taken as 0.6 km above MSL (Roy et al., 1998). For Orissa dataset, average elevation was calculated as 0.65.

3.5.5 Solar zenith angle/ Flight date and time

Solar zenith angle at time of the satellite pass is provided by the EPGS in the product description. For Udaipur the solar zenith angle is 37.214824 degrees and for Orissa the solar zenith angle is 38.450226 degrees. Flight date and time for Udaipur and Spain dataset are selected as per the data description of Hyperion

3.5.6 Scene centre latitude and longitude

The scene centre latitude and longitude is provided in the header file of the dataset.

3.5.7 Sensor altitude

The sensor altitude for hyperion scene is not provided for each scene. Hence the altitude information is derived from the topo-sheet and from the GPS that has been used in the ground truth investigation.

3.5.8 Visibility

The visibility selected for Udaipur and Orissa was inferred as "clear" in the range of 40 km.

3.5.9 Flight date and Flight time

Flight date and time is provided with the description/metadata of Hyperion.

3.5.10 Atmospheric model

The user has to make a choice, based on the geographic location of the scene to atmospherically correct the image. FLAASH supports six atmosphere types based on a seasonal-latitude surface temperature MODTRAN modelled atmospheres which is given in table 3.3

Table 3.4 Column water vapor amounts and surface temperatures for the MODTRAN model atmospheres (Source: FLAASH user guide).

Model Atmosphere	Water Vapour (std atm-cm)	Water Vapour (g/cm2)	Surface Air Temperature
Sub-Arctic Winter (SAW)	518	0.42	-16 °C or 3 °F
Mid-Latitude Winter (MLW)	1060	0.85	-1 °C or 30 °F
U.S. Standard (US)	1762	1.42	15 °C or 59 °F
Sub-Arctic Summer (SAS)	2589	2.08	14 °C or 57 °F
Mid-Latitude Summer (MLS)	3636	2.92	21 °C or 70 °F
Tropical (T)	5119	4.11	27 °C or 80 °F

Selection of MODTRAN model atmospheres is based on latitudinal/seasonal dependence of surface temperature of the study area. To help the user to select a model latitudinal ranges (0 to 80ºN and 0 to -80º S) and month of scene capture FLAASH recommends the use of a specific model for use. Based on the location of Udaipur 24º36′ N latitude for a January scene "Tropical"

model was selected. For Orissa location is at 21.7″ N latitude for January "Tropical" was selected.

3.5.11 Aerosol model/ atmospheric file

ATCOR supports four basic aerosol types: rural, urban, maritime, and desert. The user has to make a choice, based on the geographic location. Rural is recommended for areas with visibility greater 40 km. For FLAASH the Rural model represents the aerosol found in areas not strongly affected by urban or industrial sources. For both Udaipur and Orissa datasets "Rural" aerosol model was selected.

3.5.12 Water vapor retrieval

ATCOR and FLAASH include a method for retrieving the water amount for each pixel. The selection of wavelength at which the water retrieval is to be carried out is based on the availability of bands in the dataset to be atmospherically corrected. As Hyperion has bands in 356–2577 nm range the recommended 1135 nm is used for water retrieval for both Udaipur and Orissa datasets.

3.5.13 Adjacency range and zone

In order to accommodate for the adjacency effect, due to which radiances of adjacent fields of different reflectance. ATCOR allows adjacency range of 0.5 to 1 km. As the two dataset in use belong to a heterogeneous area an adjacency range of 0.5 km is selected with weight factor of 1. This same effect is treated as "adjacency correction" toggled to yes in advanced setting parameters of FLAASH. Three multiscatter models are available in FLAASH Isaacs, Scaled DISORT, and DISORT. The recommended Scaled DISORT with 8 streams (signifying 8 directional adjacency) is selected for the present study.

3.5.14 Reflectance scale factor

In order to scale the output reflectance image from floating-point into 2-byte integer data space the recommended scale factor of 10,000 is used for Udaipur and Spain datasets in ATCOR and FLAASH.

3.5.15 Additional optional parameters

More additional parameters available in ATCOR are Haze removal, Shadow removal, Value added product, and Index map. The scene of the study area is not seen to be affected by haze or shadows, these options were not utilized during atmospheric correction.

3.5.16 Wavelength calibration

The wavelength re-calibration was applied as in FLAASH, where as no such option is available in ATCOR2. This option helps in determining the shift in the wavelength (central wavelength position for each band). This certainly helps in the interpretation part when very accurate analyses of the absorption spectrums are dealt.

Once the atmospheric correction model is run, the reflectance is retrieved from the radiance.

3.6 Applying gain and offset

The spectra generated after the atmospheric correction reflects the intrinsic characteristics of the earth materials that were captured by the sensor. But it is not a continuous spectrum with breaks in certain specific locations like at 0.9μm and 1.4μm which are basically due to high water absorption and low signal factors respectively. After applying the gain and offset values the spectrum becomes continuous without any breaks.

3.7 Spectral Polishing

EFFORT polishing is a spectral polishing technique by which the artifacts present in the reflectance spectra are removed by smoothening the spectra. But before running the EFFORT polishing algorithm it is made sure that they are merely artifacts and doesn't manifest any information of the material imaged.

3.8 Field Investigations

The field investigation for Orissa and Udaipur are conducted from 28th August to 5th September 2006 and 21st November to 24th November 2006 respectively. The following sections deals with the pre-fieldwork preparation adopted for the present study.

3.9 Georeferencing of the satellite images.

Georeferencing of Udaipur and Orissa satellite dataset were carried out using the orthorectified ETM+ dataset in UTM/WGS 84 datum, zone 43N. In order to avoid spectral interpolation, nearest neighbourhood re-sampling method was used (Janssen et al., 2004).

3.10 Generation of vector database

Geological map of both the study areas were generated before the field investigation which facilitates in determining the sampling locations in the ground-truth investigation.

3.11 Sampling Plan

The spectral signature within a pixel of the image consists of an average of the reflectances of all materials within that pixel. At Hyperion's spatial resolution (15 x 15 meter) the spectral response for a geological sample will consist of a combination of spectra of all vegetation types and the soil, ground litter, etc., within the picture element. Prior to field work a random stratified sampling strategy was employed to decide on the location of sample points. Comparatively large and homogenous lithological outcrops in the study area were selected on the basis of existing geological map prepared by Geological survey of India and updated by (Roy et al., 1998). The other factors taken into consideration are the local terrain elevation the slope (to avoid shadow areas on the image), and accessibility to the area keeping in mind the fact that the data collection would have to be done in a limited period of time. Based on the above mentioned criterias 32 sampling points were selected in the study area of Udaipur and 64 locations in Orissa.

The rock samples were identified in the field and the corresponding co-ordinate locations from GPS is noted with their approximate height information.

Table 3.5 Brief description of Rock sample collected with corresponding field locations of Udaipur

Sample code	Field location in UTM coordinates		Rock/Sample collected
	Easting	Northing	
1	369700.33	2744947.16	Chlorite Schist
2	369656.95	2744965.19	Biotite Chlorite Schist
3	369484.09	2743138.45	Chlorite Schists with carbonate bands
4	371323.84	2742768.33	Quartzite
6	371871.04	2740153.14	Quartzite
7	370295.41	2738487.48	Quartzite
8	370293.09	2737232.19	Chlorite Schist
9	372026.28	2731618.40	Quartzite
12	369001.19	2735653.65	Quartzite
13	369818.04	2735084.92	Quartzite

Table 3.6 Brief description of rock sample collected with corresponding field locations of Orissa

Sample code	Field locations in Geographic coordinates		Rock/Sample collected
	Latitude	Longitude	
1	22 10 56.2 N	85 22 28.0 E	Shale
2	22 10 38.9 N	85 22 16.3 E	Banded Hematite Jasper (BHJ)
3	22 05 58.6 N	85 21 05.7 E	Banded Hematite Jasper (BHJ)
4	22 07 34.3 N	85 20 48.6 E	Laterite
5	22 05 46.1 N	85 21 56.0 E	Mine tailings
6	22 05 23.8 N	85 23 08.5 E	Laterite
7	22 02 08.3 N	85 22 14.7 E	Iron ore (Hematite)
8	22 02 20.7 N	85 21 49.9 E	Fine blue dust
9	21 59 23.0 N	85 18 52.5 E	Mine tailings
10	21 58 17.8 N	85 18 08.9 E	Weathered laterite
11	21 57 13.5 N	85 19 03.5 E	Manganese Ore
12	21 55 56.2 N	85 20 13.1 E	Banded Hematite Jasper (BHJ)
13	21 56 46.4 N	85 20 50.8 E	Iron rich soil
14	21 52 09.7 N	85 18 30.3 E	Mine tailings
15	21 53 16.2 N	85 16 50.0 E	Mine tailings

3.12 Field Spectra collection

The validation of the reflectance spectra is very important in this study. The analytical spectral device Fieldspec has been used to generate the laboratory spectra of the rock samples that have collected from the field. The spectral collection of the rock samples were conducted almost

at the same time of the sensor image capturing time. This was done to regenerate the same illumination conditions that persisted at the time of the image capture. The instrument and procedure for collection of field spectra is discussed below.

3.12.1 Instrument

In order to make measurements of surface reflectance of geological samples, an analytical spectral device, a FieldSpec®-Pro spectroradiometer, was used. The ASD radiometer is a portable array-based spectrometer consisting of a spectrometer unit, computer interface, and fiber optic probe. The instrument has two integrated radiometers covering 350 to 2500 nm. The radiometer consists of one silicon photodiode array and two fast scanning thermoelectrically (TE) cooled spectrometers with a spectral resolution 10 nm. The instrument was operated with 5° full-field-of-view (FFOV) foreoptics. A laptop interface with the instrument allows real time viewing of the spectrum recorded. The ASD instrument records the spectra in 2151 continuous bands. The spectral range and spectral resolution of the ASD instrument meet the present study requirement on Hyperion datasets. Table shows the characteristics of the instrument used.

Table 3.7 Analytical Spectral Device FieldSpec-FR specifications (source: FieldSpec® Pro User Guide)

Spectral Range	350 - 2500 nm
Spectral Resolution	FWHM 3 nm for 350-1000 nm FWHM 10 nm for 1400 -2100 nm
Sampling Interval	1.4 nm for 350 - 1050 nm 2 nm for 1000 - 2500 nm
Scanning Time	100 milliseconds
Detector	One 512 element (Si photodiode array 350 - 1000 nms) Two separate, TE cooled, InGaAs (Indium-Gallenium-Arsenide) photodiodes 1000 - 2500 nm
Input device	Foreoptics gun

3.12.2 Instrument calibration

A certain amount of electrical current is generated by thermal electrons within the ASD and always added to the incoming photons of light during spectra collection. This adversely affects the spectra collection and has to be removed. This process is known as “Dark Current Correction”. Spectral data collection requires instrument calibration using a reference panel (“Spectralon” white reference) provided along with the instrument. During the white reference collection, a reference 100% line is available to the user to check the status of the instrument performance. White reference collection includes dark current correction and was repeated every 20 minutes during the collection of sample spectra. This minimises the effects of the changing lighting conditions on the recorded spectra. This calibration was repeated several times during the sampling period to establish changing light conditions or instrument drift.

Before the field spectra collection, to test the performance of the instrument a comparison for vegetation spectra was done. Figure 3.4 shows an example of tree foliage spectra (Dhoke variety of tree found abundantly in Udaipur environs) taken in IIRS campus compared with

atmospherically corrected image spectra extracted from Udaipur image. The vegetation spectra from ASD and image exhibit similar trends, indicating precision of the instrument.

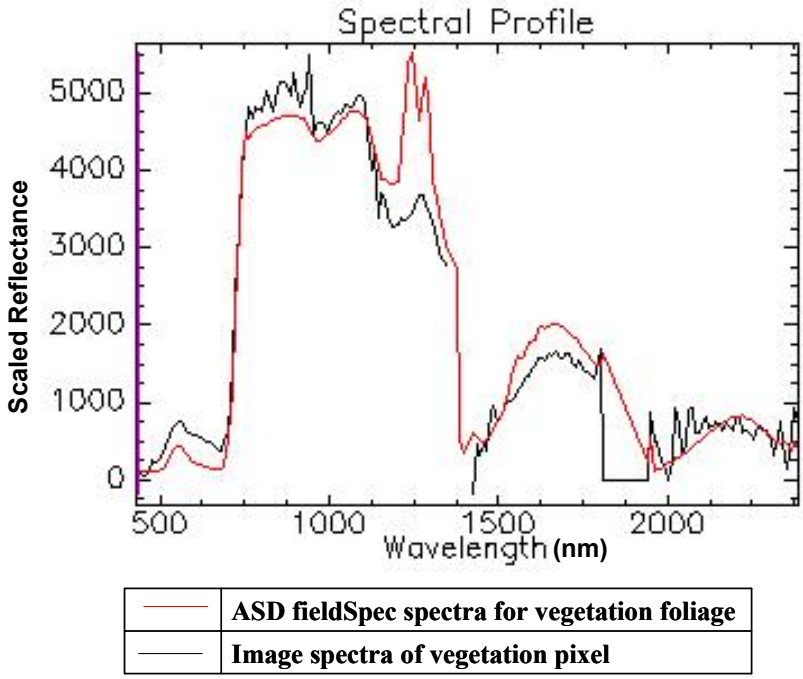

Figure 3.10 Image spectra and their corresponding ASD target spectra

3.12.3 Spectral data collection

The northern part of the study area has been under survey by various National organizations for the last few years, and is considered a potential mineralization zone. Out of 32 spectra collected from ASD spectro-radiometer, 13 samples of the northern part of the study area were taken up for further processing. The field spectra collections was undertaken within 2 hours before and after solar noon to simulate the similar illumination conditions as during the satellite pass. The rock types were identified as Grey Quartzite and Chlortite schist.

3.12.4 Creation of ASD and image spectral library

The ASD records spectra in 1251 bands at 2 nm band width. To compare the ground-measured spectra collected from ASD with that of atmospherically corrected image spectra, the ASD spectra were re-sampled to the Hyperion FWHM and bandwidth. A spectral library of re-sampled ASD spectra was created. The spectra from the ASD library were used as standard to compare image reflectance spectra extracted using the two atmospheric correction models. The ground control points collected during the ground truth investigation were used to locate the exact pixel in the image which corresponds to the respective sample location. The image spectra for all the major sampling locations were generated similarly and saved in spectral library.

3.13 Hyperspectral Processing for mineral mapping

Mineral targeting using hyperspectral data is now a proven fact internationally thought it is yet to take off in full fledged manner in India because of the non –availability of such data. Hyperspectral remote sensing combines imaging and spectroscopy in a single system which often includes large data sets and requires new processing methods. Hyperspectral data sets are generally composed of about 100 to 200 spectral bands of relatively narrow bandwidths (5-10 nm), whereas, multispectral data sets are usually composed of about 5 to 10 bands of relatively large bandwidths (70-400 nm). The increase in the number of bands is both a blessing and a curse. The large number of bands provides the opportunity for more materials to be discriminated by their respective spectral response. However, this large number of bands is the characteristic which leads to complexity in analysis techniques. The techniques described in the following sections are those which are widely used by the USGS, NASA's Jet Propulsion Laboratory, ENVI, and others. There are, however, other methods and algorithms to extract information from hyperspectral sensors.

One difficulty in working with hyperspectral data is to understand the differences associated with working in n-dimensional space. One must be careful about using two or three dimensional conceptual truths as a basis for conclusions in higher dimensional spaces (Langrebe, 1997). AIG has developed standard methods for analysis of hyperspectral data. The Hyperion data were processed to geologic products using AIG developed approaches for extraction of mineralogical and geological information. This hyperspectral analysis methodology includes 1) Data Pre-processing, 2) Correction of data to apparent reflectance using the atmospheric correction software, 3) Linear transformation of the reflectance data to minimize the noise and data dimensionality, 4) Location of the most spectrally pure pixels, 5) Extraction and automated identification of endmember spectra, 6) Spatial mapping and abundance estimates for specific image endmembers. A key point of this methodology is the reduction of data in both the spectral and spatial dimensions to locate, to characterize, and identify a few key endmember spectra that can be used to explain the rest of the hyperspectral data set. Once these endmembers are selected, then their location and abundance can be mapped from the original data set. These methods derive the maximum information from the hyperspectral data, themselves minimizing the reliance on a priori or outside information (Kruse, 2002).

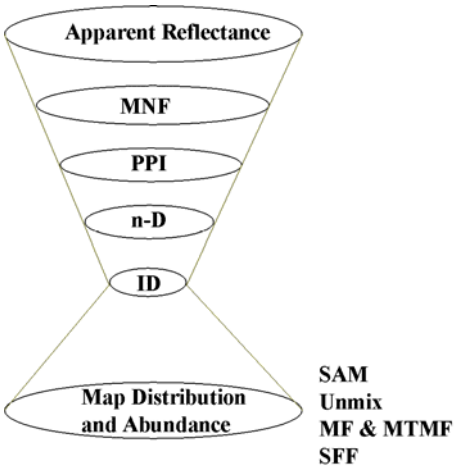

Figure 3.11 Methodology for mineral mapping using spectral analysis

Hyperspectral processing for mineral mapping includes the spectral processing and manipulation of the Hyperion data set with the correspondence to the geology of the study area. As it is observed in the nature, there are n-numbers of materials randomly distributed over the earth surface. Imaging space borne satellites acquire the information about the earth materials in different ranges of electromagnetic spectrum (spectral resolution) with certain amount of energy coming out of a specific area (spatial resolution) in a particular direction. Depending upon the spatial and spectral resolution of the imaging sensors the spectral information was modified in the images. Several techniques were applied for the differentiation of the materials based on their spectral variability present in the image. Pure endmembers were selected from the image on the basis of field observation in the area.

3.13.1 Process of selection of image end members

3.13.1.1 Creation of Minimum Noise Fraction (MNF) image

Hyperspectral imagery is capable of providing a continuous spectrum ranging from 0.4 to 2.5 microns (in the case of AVIRIS) for a given pixel, it also generates a vast amount of data required for processing and analysis. Due to the nature of hyperspectral imagery (i.e. narrow wavebands), much of the data in the 0.4-2.5 micron spectrum is redundant.
The minimum noise fraction (MNF) transformation is used to determine the inherent dimensionality of image data, to segregate noise in the data, and to reduce the computational requirements for subsequent processing (Boardman and Kruse, 1994). The MNF transform is essentially two cascaded Principal Component transformations. The first transformation, based on an estimated noise covariance matrix, de-correlates and rescales the noise in the data. This first step results in transformed data in which the noise has unit variance and no band-to-band correlations. The second step is a standard Principal Components transformation of the noise-whitened data (Green et. al., 1985). For the purposes of further spectral processing, the inherent dimensionality of the data is determined by examination of the final eigen values and the associated images. The data space can be divided into two parts: one part associated with large eigenvalues and coherent Eigen images, and a complementary part with near-unity eigen values and noise dominated images. By using only the coherent portions, the noise is separated from the data; thus improving spectral processing results. The MNF transform can also be used to remove noise from data by performing a forward transform, determining which bands contain the coherent images (by examining the images and eigen values), and running an inverse MNF transform using a spectral subset to include only the good bands, or smoothening the noisy bands before the inverse.

Minimum Noise Fraction images created for the 196 unique bands of hyperion in the present study for both the study areas extracted around 20 bands with the maximum information. The remaining bands contain maximum noise. Hence the first 20 bands were used for further processing and finding out pure pixels in the image.

3.13.1.2 Pixel Purity Index

The Pixel Purity Index (PPI) is a means of finding the most “spectrally pure” or extreme pixels in the multispectral and hyperspectral images (Boardaman et al., 1995). The most spectrally pure pixels typically correspond to mixing endmembers. The Pixel Purity Index is computed by repeatedly projecting n-dimensional scatterplots onto a random unit vector. The extreme pixels in each projection are recorded and the total number of times each pixel is marked as extreme is noted. A “Pixel Purity Image” is created in which the digital numbers in each pixel

corresponds to the number of times that pixel was recorded as extreme. The PPI is typically run on a Minimum Noise Fraction (MNF) transform result excluding the noise bands.

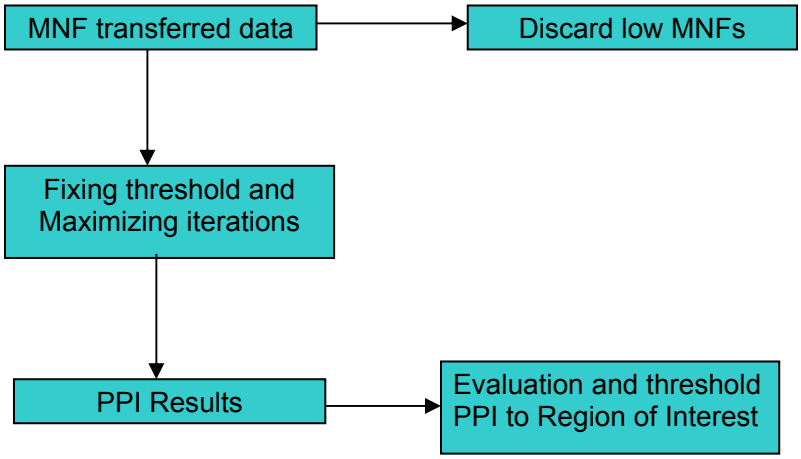

Figure 3.12 Methodology for endmember selection

In this study, number of iterations with different threshold limit was carried out interactively to isolate the position of most pure pixels in the image. A threshold of three was fixed for the identification of pure pixels in the image which can be explained as, all the pixels having 3 DN values (maximum limit) greater than the extreme pixel is considered as being pure. Different sets of iterations 50, 100, 500 and 1000 were carried out on this dataset with keeping the threshold at 3. It was observed that more the number of iterations more the number of extreme pixels found with more variability in the dataset. The value in the Pixel Purity Index image indicates the number of times each pixel was discovered as extreme in some projection. The higher values in PPI image indicate pixels that are nearer "corners" of the n-dimensional data cloud, and are thus relatively purer than the pixels with lower value. In the last step one region of interest (ROI) was created for the PPI image keeping the minimum threshold limit at 5, after comparing the pixel purity index image with calibrated image to get a better idea about the position of the pure pixels.

3.13.1.3 Using PPI images in a n-dimensional visualiser for endmembers collection

Spectra can be thought of as points in an n-dimensional scatterplots, where n is the number of bands. The coordinates of the points in n-space consist of "n" values that are simply the spectral radiance or reflectance values in each band for a given pixel. The distribution of these points in n-space can be used to estimate the number of spectral endmembers and their pure spectral signatures. The n-Dimensional visualizer provides an opportunity for interactive selection of the endmembers in n-space. The n-D visualizer is used in conjunction with the Minimum Noise Fraction Transform (MNF) and Pixel Purity index (PPI) tools to locate, identify and cluster the purest pixels and most extreme spectral responses in a data set. The n-Dimensional visulizer allows for interactive rotation of data in n-D space, selection of groups of pixels into different classes (Boardman, 1993; Boardman and Kruse, 1994). Here in this study this procedure was followed to isolate different group of pixels representing different endmembers. Several groups of pixels were isolated mostly projected at the corners of the scatter plot or completely isolated in the interactive scatterplots. The selected classes were exported to Region of Interest (ROI) and used as input for further spectral processing.

3.14 Mineral Mapping Techniques

Classification and feature extraction methods have been commonly used for many years for the mapping of minerals and vegetative cover of multispectral data sets. However, conventional classification methods, such as a Gaussian Maximum Likelihood algorithm, cannot be applied to hyperspectral data due to the high dimensionality of the data. Several mapping techniques were applied in the present study to map the abundance of minerals present in the two study areas.

3.14.1 Band Rationing

Ratio transformation is another technique of extracting information from highly correlated dataset. The major advantage of ratio images is that they convey the spectral or colour characteristics of image features regardless of variations in scene illumination condition. Ratio images are often useful for discriminating subtle spectral variations that are masked by the brightness variations in individual spectral bands. Ratio images are created by calculating the ratios of DN values from two image bands and mathematically it can be expressed as

$$RDN_{ij} = DN_i/DN_j$$

Where DN is the intensity in the ith and jth channel of the satellite images and RDN is the ratio value in the resulting images. The ratio image range from 0 to infinity and shows the variations in the slope of spectral reflectance curves between two bands involved. The most commonly used band ratios and their target minerals are given in the figure below.

Commonly used ratios

Feature	Band or Ratio	Comments	Reference
Iron			
Ferric iron, Fe^{3+}	2/1		Rowan; CSIRO
Ferrous iron, Fe^{2+}	5/3 + 1/2		Rowan
Laterite	4/5		Bierwith
Gossan	4/2		Volesky
Ferrous silicates (biot, chl, amph)	5/4	Fe oxide Cu-Au alteration	CSIRO
Ferric oxides	4/3	Can be ambiguous*	CSIRO
Carbonates / Mafic Minerals			
Carbonate / chlorite / epidote	(7+9)/8		Rowan
Epidote / chlorite / amphibole	(6+9)/(7+8)	Endoskarn	CSIRO
Amphibole / MgOH	(6+9)/8	Can be either MgOH or carbonate*	Hewson
Amphibole	6/8		Bierwith
Dolomite	(6+8)/7		Rowan, USGS
Carbonate	13/14	Exoskarn (cal/dolom)	Bierwith, Nimoyima, CSIRO
Silicates			
Sericite / muscovite / illite / smectite	(5+7)/6	Phyllic alteration	Rowan (USGS); Hewson (CSIRO)
Alunite / kaolinite / pyrophyllite	(4+6)/5		Rowan (USGS)
Phengitic	5/6		Hewson
Muscovite	7/6		Hewson
Kaolinite	7/5	Approximate only*	Hewson
Clay	$(5x7)/6^2$		Bierwith
Alteration	4/5		Volesky
Host rock	5/6		Volesky
Silica			
Quartz rich rocks	14/12		Rowan
Silica	(11x11)/10/12		Bierwith
Basic degree index (gnt, cpx, epi, chl)	12/13	Exoskarn (gnt, px)	Bierwith, CSIRO
SiO2	13/12	Same as 14/12	Palomera
SiO_2	12/13		Nimoyima
Siliceous rocks	(11x11)/(10x12)		Nimoyima
Silica	11/10		CSIRO
Silica	11/12		CSIRO
Silica	13/10		CSIRO
Other			
Vegetation	3/2		
NDVI	(3-2)/(3+2)	Normalised difference vegetation index	

Figure 3.13 Various band ratios and their applications

The correlation between ratio images are lower than the correlation between the original LISS IV images resulting from the reduction of a wide range of DNs to a single RDN. The source

of variation which can be attributed to illumination differences in the scene, is reduced after rationing, which means that the spectral shape become proportionally more important. However, reducing variance due to illumination also implies that additive noise as well as effects of multiple reflections and atmospheric scattering will be exaggerated in ration images (Van der Meer, 1995).

3.14.2 Spectral Angle Mapper Classification

The Spectral Angle Mapper Classification (SAM) is an automated method for directly comparing image spectra to a reference (usually determined in a lab or in the field with a spectrometer) or an endmember. This method treats both (the questioned and known) spectra as vectors and calculates the spectral angle between them. This method is insensitive to illumination since the SAM algorithm uses only the vector direction and not the vector length. The result of the SAM classification is an image showing the best match at each pixel. This method is typically used as a first cut for determining the mineralogy and works well in areas of homogeneous regions. The USGS maintains a large spectral library, mostly composed of mineral and soil types, which image spectra can be directly compared.

The spectral angle mapper (SAM) has been widely used as a spectral similarity measure. It calculates spectral similarity between the reference reflectance spectrum (ASD spectrum) and the test spectrum (image spectrum). The angle between two spectra is used as a measure of discrimination (equation 5-1). The spectral similarity between the image spectrum (t) and reference spectrum (r) can be expressed as an average angle (θ) between the two spectra for each channel (i) (Van der Meer and De Jong, 2003).

$$\theta = \cos^{-1}\left[\frac{\sum_{i=1}^{n} t_i r_i}{\sqrt{\sum_{i=1}^{n} t_i^2 \sum_{i=1}^{n} r_i^2}}\right]$$

The result of SAM is an angular difference measured in radian ranging from zero to $\pi/2$ which gives a qualitative estimate of similarity between image spectrum and ASD spectrum (Van der Meer and De Jong, 2003). Small spectral angle values correspond to high similarity between image spectra and ASD spectra. Larger angle values correspond to less similarity.

3.14.3 Mixture Tuned Matched Filtering

Mixture tuned matched filtering (MTMF) performs a partial unmixing- finding the abundances of user defined endmembers. Not all of the endmembers in the image need to be known. This technique maxmises the response of the known endmember and suppresses the response of the composite unknown background, thus “matching” the known signature. The matched filtering results will appear as a series of gray-scale images with values ranging from 0.0 to 1.0 (zero to one). This image provide a means of estimating relative degrees of match to the reference spectrum and approximate sub-pixel abundance, where 1.0 is a perfect match with the reference spectrum and 0.0 is no match situation. It provides a rapid means of detecting specific materials based on matches to library or image endmember spectra and does not require knowledge of all the endmembers within the image scene. This technique may find some “false positives” that shows high values in terms of matching score for rare materials which is taken care of by an output “infeasibility” image to the results. The infeasibility image is used to reduce the number of “false positives” that are sometimes found using matched filtering technique. Pixels with a high infeasibility are likely to be matched filter false positives. Correctly mapped

pixels will have a high matched filter score and a low infeasibility value where as Pixels with a high matched filter result and high infeasibility are "false positive" pixels and do not match the target. The infeasibility values are in noise sigma units which vary in digital number scale with matched filter score and indicate the feasibility of the matched filter results (Harsanyi & Chang, 1994; Chen & Reed, 1987).

Mixture Tuned Matched Filtering technique combines the best part of the linear spectral unmixing model and the statistical matched filter model while avoiding the drawbacks of each model. From matched filtering it inherits the advantage of its ability to map a single known target without knowing the other background endmember signatures, unlike traditional spectral mixing models. From spectral mixture modeling it inherits the leverage arising from the mixed pixel model, the constraint on feasibility including the unit sum and positively requirements unlike the Matched Filter which does not employ these fundamental facts (Boardman, 1995). Hence this method can out perform either method in case of subtle, sub-pixel occurrences.

3.14.4 Linear spectral unmixing

Linear Spectral Unmixing is a means of determining the relative abundances of materials depicted in multispectral imagery based on the materials spectral characteristics. The reflectance at each pixel of the image is assumed to be a linear combination of the reflectance of each material (or endmember) present within the pixel. There are certain limitations that apply for the linear spectral unmixing technique. The number of endmembers must be less than the number of spectral bands and all of the endmembers in the image must be used for an efficient mapping result. Spectral unmixing results are highly dependent on the input endmembers and changing the endmembers will change the results.

A unit-sum constraint in the linear Mixing algorithm was applied in this study where the score varies between zero and one. This was implemented to allow for user-defined weighting of a sum-to-unity constraint on the abundance fractions. It also permits proper unmixing of MNF-transform data, with zero-mean bands. The weight factor, a default value of one is used for the extra constraint equation. This weighted unit-sum constraint is then added to the system of simultaneous equations in the unmixing inversion process (Boardman, 1989; 1992).

Linear spectral unmixing images produced for this area show similar feature like the MTMF images. As this model gives information about the relative abundances of the material considering each endmember present in a pixel. In this study we have chosen all the major endmembers which best describes the image, which are discussed in detail in the next chapter.

3.14.5 Spectral Feature Filtering

Spectral feature fitting is an absorption-feature based methodology for comparing the fit of the image spectra to selected reference spectra using least squares technique. The reference spectra are scaled to match the image spectra after continuum removal from both data sets. A scale image is output for each reference spectrum and is a measure of absorption feature depth, which is related to material abundance. The image and reference spectra are compared at each selected wavelength in a least-squares sense and the root mean square error (rms) is determined for each reference spectrum (Clark et al., 1990).

3.14.6 Band Absorption Depth Analysis

When light interacts with a mineral or rock, light of certain wavelengths is preferentially absorbed while at other wavelengths it is transmitted or reflected from the substance. Reflectance is defined as the ratio of the intensity of light reflected from a sample to the intensity of the light incident on it. Electronic and charge transfer processes e.g., changes in energy states of electrons bound to atoms or molecules associated with transition metal ions such as Fe, Ti, Cr, etc., determine largely the position of diagnostic absorption features in the visible- and near-infrared wavelength region of the spectra of minerals (Van der Meer and De Jong, 2003). Band positioning and absorption analysis have been successfully attempted in Airborne Visible and Infrared Imaging Spectrometer (AVIRIS) data for surface mineralogical information extraction (Van der Meer, 2004). This technique has been adopted in the present study for Udaipur and Orissa Hyperion dataset.

A spectrum has two components, continuum and the absorption feature itself. The continuum is defined as a piecewise-linear envelope enclosing the radiance spectra.The continuum or background is the over all albedo of the reflectance curve. Removing the continuum effectively normalizes the spectra (Van der Meer, 2004). The modified spectra exhibit a flat background, but absorption features are retained. The flat background means no absorption feature.

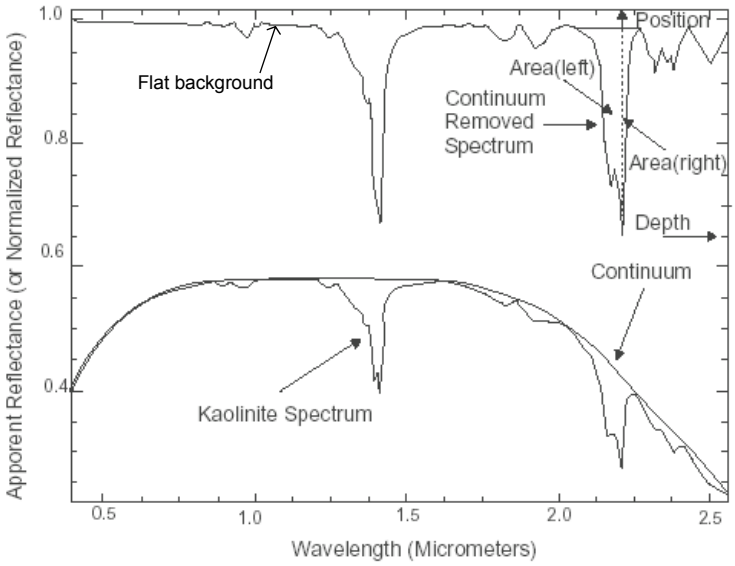

Figure 3.14 Continuum and absorption parameters (Van der Meer, 2004)

To carry out band absorption analysis three parameters (i) absorption band position, (ii) absorption depth and (iii) absorption band asymmetry have been proposed (Van der Meer, 2004). Figure 3.9 shows a schematic view of parameters used in the derivation of absorption characteristics. These parameters are derived from continuum removed spectra. Absorption band position is defined as the minimum reflectance value over the wavelength range. Absorption band depth is calculated relative to the continuum as

$$D = 1 - \frac{R_b}{R_c}$$

Where Rb is the reflectance at the band bottom and Rc is the reflectance of the continuum at the same wavelength. Estimation of absorption depth position provides useful information about the absorption feature that could be attribute to a mineral of interest. Absorption band asymmetry describes the shape of the absorption feature. The asymmetry factor is defined as

$$S = \frac{A_{left}}{A_{right}}$$

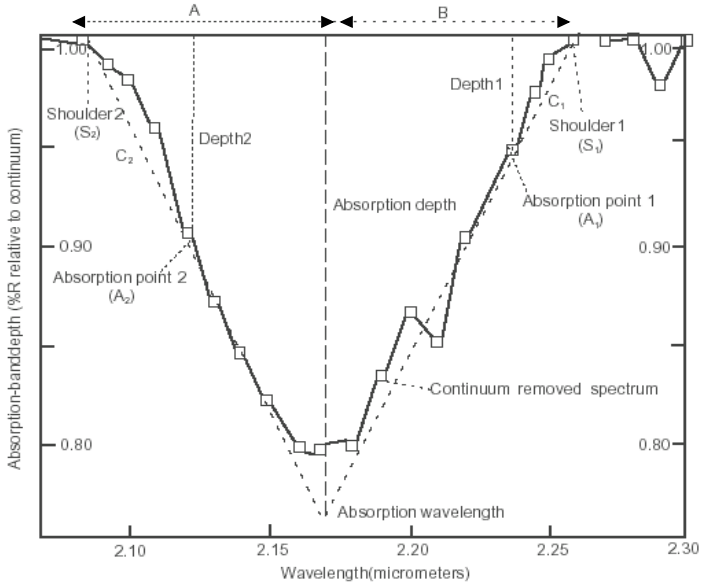

Figure 3.15 Schematic representation of parameters used derive absorption characteristics (Van der Meer, 2004)

The values of asymmetry range from 0 to infinity. Asymmetry value of 1 for symmetrical shape, value range greater than 1 for skewed shape towards longer wavelength and value range between 0 and 1 for skew towards shorter wavelength.

The absorption parameter definitions assume spectra to be continuous. To mathematically implement the derivation of these parameters (equation 3-8 and 3-9) a linear interpolation is suggested for hyperspectral discrete spectral bands. The inputs required are identification of short wavelength shoulder (S2), longer wavelength shoulder (S1), Short wavelength absorption band location (A2) and long wavelength absorption location (A1). A linear relationship is established using four points to calculate coefficients C1 and C2 (equation 3-8 and 3-9) (Van der Meer, 2004).

$$C_1 = \sqrt{\left[(depth)^2 + (S_1 - A_1)^2\right]}$$

and

$$C_2 = \sqrt{\left[(depth_2)^2 + (S_2 - A_2)^2\right]}$$

The absorption wavelength was mathematically be expressed as equation 3-12 (Van der Meer, 2004).

$$Absorption\_wavelength = -\left[\frac{C_1}{C_1 + C_2} \times (A_1 - A_2)\right] + A_1$$

The associated absorption-band depth was then derived using equation 3-14(Van der Meer, 2004).

$$absorption\_depth = \left[\frac{S_s - absorption\_wavelength}{S_s - A_s}\right] \times depth_1$$

The asymmetry factor of the absorption feature was calculated using equation 3-16 (Van der Meer, 2004).

Asymmetry = (absorption_wavelength-S_2) – (S1 – absorption_wavelength)

The derivation of the band positioning and absorption for Udaipur dataset were performed using ENVI-IDL script developed during the study. The parameters S_1, S_2, A_1, and A_2 required for the band positioning and absorption analysis were derived from the Udaipur dataset for quartzite rock and Banded Hematite Jasper from the Orissa dataset.

The output result for the entire mapping techniques used in the present study is discussed in the next chapter, results and discussions.

Chapter 4

Results and Analysis

This chapter discusses with the various results of this project. The results were attained at different levels, some during the pre-processing of the dataset and while others in the latter stage of the project work. Different methods as well as various permutations have been adopted in the study to obtain the best possible results. This led to so many results which helped us during the final interpretation directly and indirectly which ultimately facilitated the completion of this work.

4.1 Band De-stripping

Both global as well as local band stripping techniques were used in this study to remove the stripes present in the various bands of the Hyperion dataset. Both the de-stripping techniques were employed in this work and the local de-stripping came up with better result. These stripes in the bands resulted in spike or aberrations in the spectra. These aberrations neither represent any characteristic feature of the target under the study nor the atmospheric attenuations. They are due to the vertical stripes present in the various bands of the Hyperion dataset which can be attributed to the sensor incapability.

The existing methods to identify the stripes use cumulative mean, variance, minimum and maximum of each pixel in each column. Detection of bad columns is carried out using set thresholds based on median values from its neighbourhood. The bad pixel is then replaced with the median value of its neighbourhood (Datt et al., 2003). The value of threshold is scene dependent and different for each band containing stripes. Setting up of the threshold is at the cost of changing the spectra.

The missing line filter designed in the present study only targets the visually identified bad columns (section 3-1), other pixel values remain unchanged. Hence the filter has a local balancing effect on the image. Examination of difference between the level 1R product and de-striped image indicates that the stripes in VNIR are removed and the image appears smooth. Figure 4.1 shows the effect of de-striping on the image and the corresponding DN values of one stripe on the image using the designed filter on the Hyperion datasets (as discussed in section 3.2.1). Form the visual inspection of the two images there is an over all contrast difference between the two. This difference is mainly due to the change in image statistics resulting from the de-striping of bad columns.

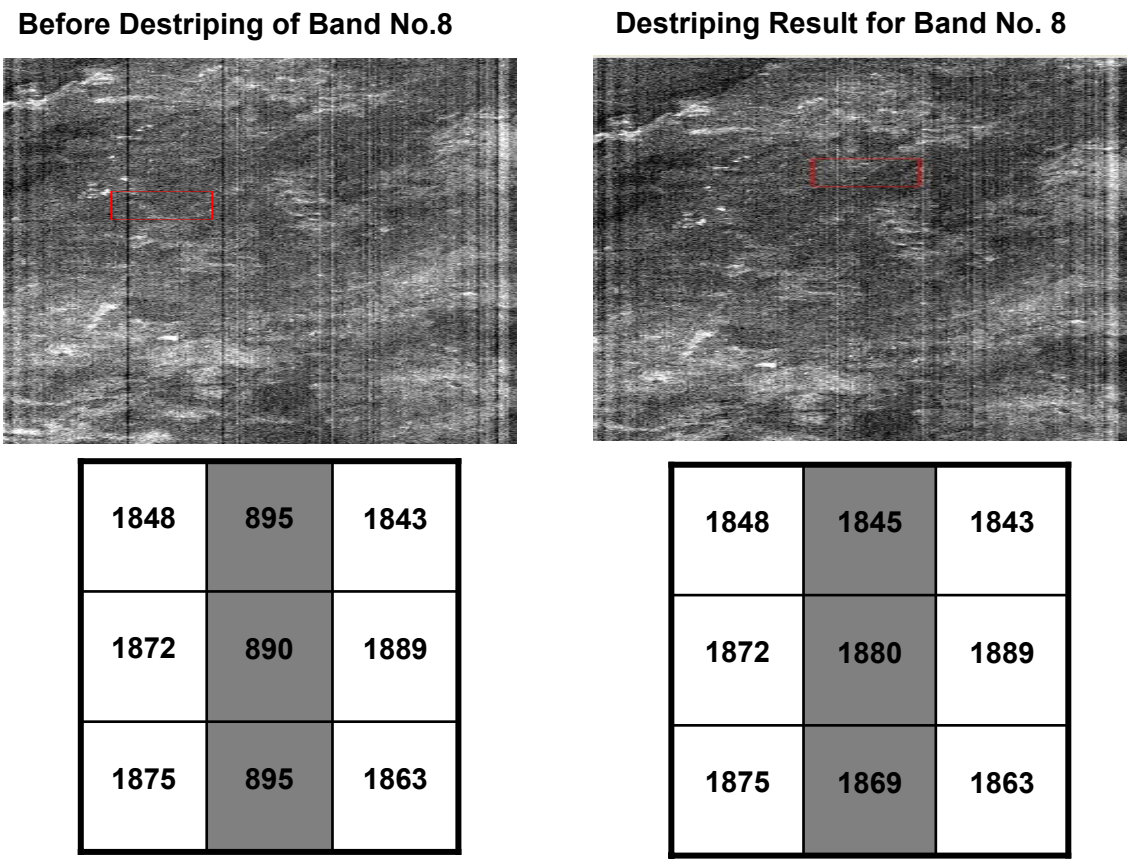

Figure 4.1 Destriping results of Orissa datasets

The destriping results are very well manifested in the resultant spectra. The comparison of spectras before and after destriping manifest remarkable improvement in the spectral smoothening which was primarily due to sensor incapability. The spikes or deep absorptions which are not characteristic of the target under study in both the datasets (Udaipur and Kheonjhar) were removed to a large extent by the process of destriping.

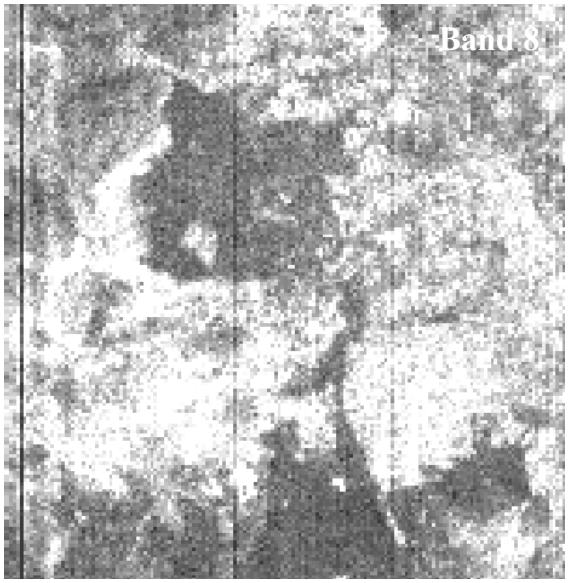

1075	1063	805	1213	1222
1163	1063	850	1037	1308
987	1063	895	1213	1308

(a)

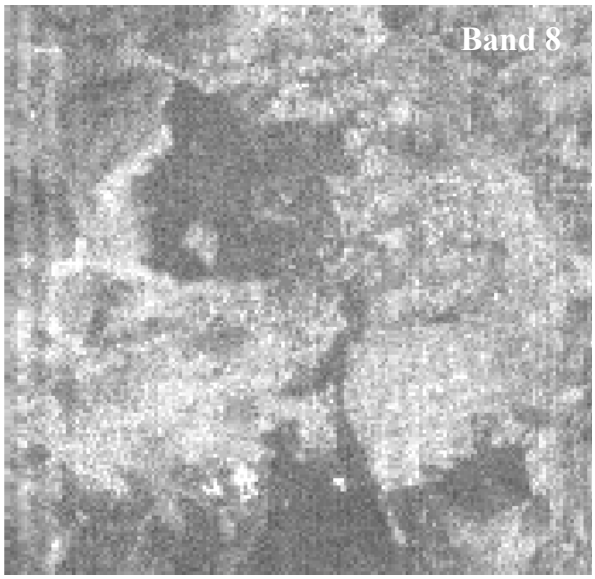

1075	1063	1109	1213	1222
1163	1063	1123	1037	1308
987	1063	1145	1213	1308

(b)

Figure 4.2 Destriping results; (a) before and (b) after

The local balancing effect can also be seen on the image spectra. The image spectra improves after performing de-striping and spurious spikes in the VNIR region (300 to 700 nm) are reduced, while no change in the spectra is seen in SWIR region. Figure 4.2 (a), (b) illustrates spectra taken at bad column in level 1 R product and post de-striping processing (pixel 6, 1148).

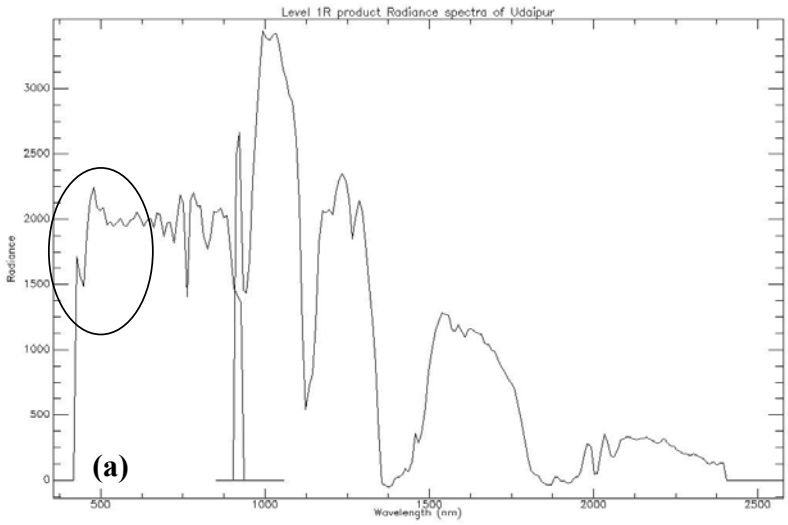

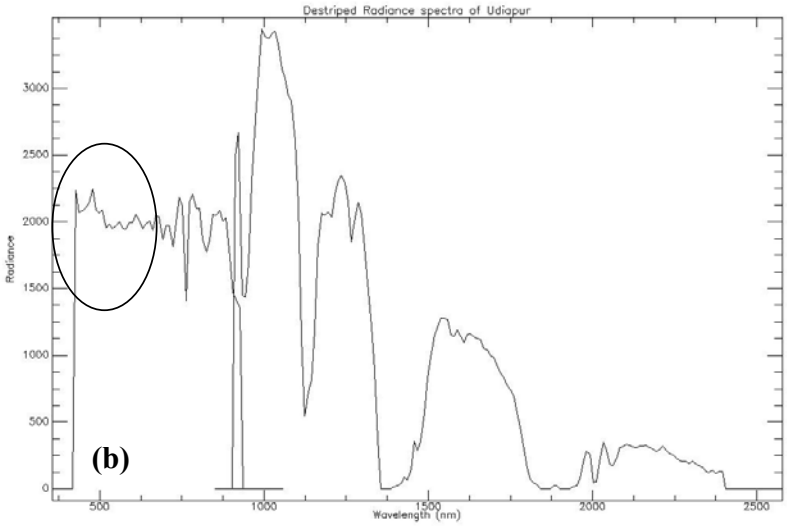

Figure 4.3 Local balancing effect of de-striping on the image spectra taken over know bad column. The encircled region shows the region of improvement. (a) spectra of Level 1 R product (b) spectra after de-striping.

4.2 Radiance Spectra

The spectra extracted from Hyperion L1R dataset exhibits atmospheric gaseous absorption features. These absorptions can be observed in the spectral region from 400 to 2500 nm. The known absorption regions of the atmosphere are used here to identify the effects on image spectra.

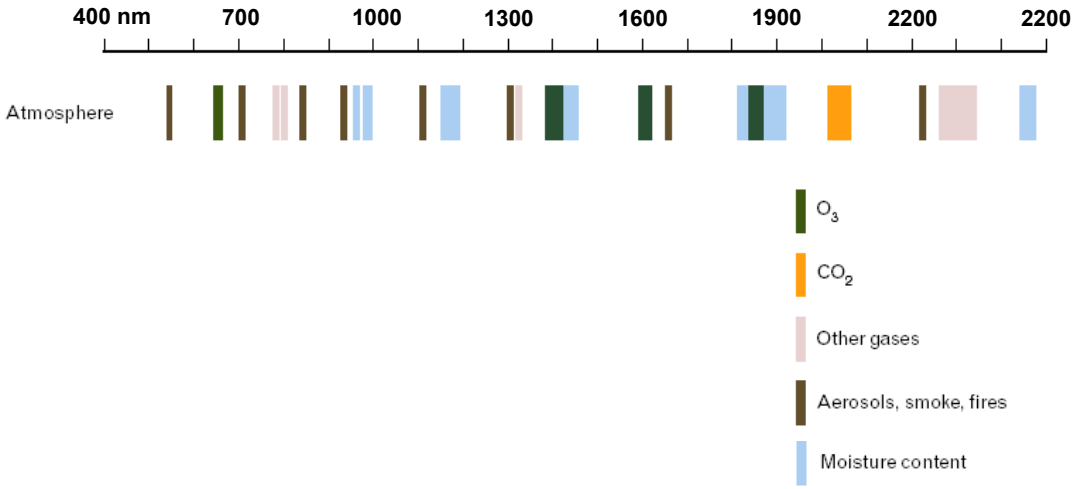

Figure 4.4 Known absorption regions of atmospheric constituents (Griffin and Hsiao-hua, 2003).

To understand the absorption regions in the radiance spectra radiance dataset of Udaipur was taken. A spectrum over vegetation was extracted to visually analyze the effects of the intervening atmosphere before the radiance image was subjected to atmospheric correction.

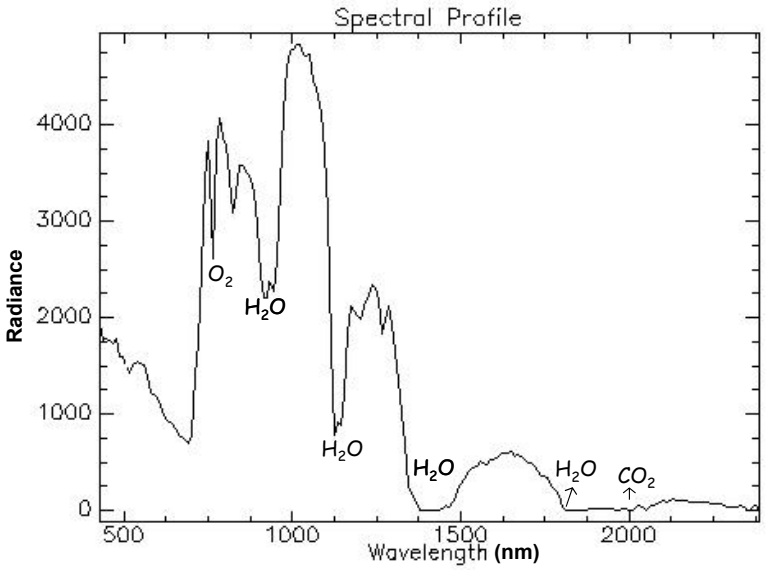

Figure 4.5 Radiance spectra of vegetation over Udaipur showing absorption features of oxygen, carbon di oxide.

At 760 nm, a strong, narrow oxygen absorption line is present. CO_2 is absorbed strongly from 1900 to 2055 nm. CO_2 also exhibits a weak absorption line at 1430 nm. At 940 and 1140 nm, water vapor absorption is strong and is used to derive the total column water vapor. Water vapor absorption near 1375 and 1900 nm is strong enough and makes retrieval of the surface reflectance difficult from the image. The water vapor has the largest effect on the radiance. Oxygen and other gases along with aerosols in the atmosphere also affect the radiance spectra. The atmospheric correction models include modeled atmosphere, aerosol models, water vapor retrieval and CO_2 concentration as input parameters. These input parameters along with image ratio methods adopted by the ATCOR and FLAASH to retrieve water vapor, CO_2 for the image itself should compensate for these absorption regions. ATCOR and FLAASH both use MODRTAN and has out performed other radiative transfer code especially in the water region 940 and 1130 nm and CO_2 at 2055nm (Staenz et al., 2002).

4.3 Atmospheric correction Results

FLAASH as well as ATCOR2 atmospheric correction models were applied on both the datasets. This section discusses the results achieved by atmospheric correction using both the models.

Table 4-1 ATCOR and FLAASH input parameters applied on radiance images of Udaipur and Kheonjhar, Orissa dataset

ATCOR2			**FLAASH**		
Parameters	**Udaipur**	**Orissa**	**Parameters**	**Udaipur**	**Orissa**
Sensor type	Hyperion	Hyperion	Sensor type	Hyperion	Hyperion
Pixel size	30	30	Pixel size	30	30
Ground elevation	0.6 km	0.65 km	Ground elevation	0.6 km	0.65 km

ATCOR2			**FLAASH**		
Parameters	**Udaipur**	**Orissa**	**Parameters**	**Udaipur**	**Orissa**
Solar Zenith angle	37.214824º	38.450226º	Scene centre Lat/Long	24.6º N, 73.7º E	21.7º N, 85.4º E
Visibility	40 km	40 km	Visibility	40 km	40 km
Sensor altitude	un-editable	un-editable	Sensor altitude	703.3166 km	707.3276 km
Flight date	19/01/2004	16/01/2006	Flight date & flight time	19/01/2004 5:22:17	16/01/2006 4:33:49
Atmospheric file	hyperion.cal	hyperion.cal	-	-	-
Atmospheric model	h99000_ wv10_rura	h99000_ wv10_rura	Atmospheric model	Tropical	Tropical
Adjacency range	1 km	1 km	-	-	-
Zones	0.5	0.5	Aerosol model	Urban	Tropical
Region for water vapour	940 to1130	940 to1130	Water vapour retrieval	1135 nm	1135 nm
-	-	-	Spectral polishing	No	No
Water vapour absorption	Yes	Yes	Wavelength calibration	Yes	Yes
Haze removal	Yes	Yes	Advanced parameters		
Reflectance scale factor	100	100	Output reflectance scale factor	10000	10000
-	-	-	MODTRAN resolution	15 cms-1	15 cms-1
-	-	-	MODTRAN multi scattering model	Scaled DISORT 8 Stream	Scaled DISORT 8 Stream
Reality spectra booster	Yes	Yes	-	-	-
CO_2 (un-editable)	360 ppm	360 ppm	CO_2 (user defined)	390 ppm	390 ppm

The FLAASH atmospheric correction model provides more options to the user than the ATCOR2 models which shows a direct bearing on the reflectance spectra. The option of user

defined sensor height is an addition in FLAASH. ATCOR2 establishes sun-sensor geometry on the basis on solar zenith angle and un-editable sensor height (defined as 705 km in hyperion.cal file). To accommodate for adjacency effect FLAASH allows selection of MODTRAN resolution and MODTRAN multiple scattering model. These settings can objectively be selected based on the variability in terrain conditions (uniformity or varying landuse). User defined CO_2 concentration level is also a useful input variable to be defined by the user in FLAASH, as the CO_2 levels varies with the presence of dense urban and industrial area in the scene. In ATCOR model CO_2 level is set at default 360 ppm and is un-editable. These differences that the model provides to the user helps in better radiative transfer model results. The results from the two atmospheric correction models were compared. The vegetation and water spectra are used for this purpose. The conventional absorption depths as well as reflectance peaks were analyzed to understand the performance of the two radiative transfer models.

4.3.1 Vegetation spectra

Reflectance properties of vegetation in the VNIR and SWIR part of the spectrum are dominated by the strong atmospheric absorption regions and absorption properties of the chlorophyll a and b pigments. The image spectra extracted from ATCOR and FLAASH exhibit no significant absorption at wavelengths 1900 and 2100 nm, indicating that, CO2 input of 390 ppm (default being 320) was sufficient to compensate for CO2. Narrow absorption at 760 nm corresponding to O2 is compensated by both the models, as no significant dip is seen in the spectra. Pigments in vegetation show absorption at 640 and 660 nm. The shape of the absorption feature is clearly seen in the FLAASH extracted spectra Figure 4-(a), (b). Similar observation have also been reported on HYDICE image corrected using FLAASH (Griffin and Hsiao-hua, 2003) (Datt et al., 2003). Spurious peaks in both the spectra at 940 nm indicated the strong water absorption is under estimated by both models, this signifies that stronger water absorption region at 1140 nm is over estimated and is seen as sharp dip at 1124 nm and 1146 nm in ATCOR and FLAASH, respectively. Earlier studies have shown similar results using FLAASH (Griffin and Hsiao-hua, 2003). The difference in the positions of the water vapour absorption could be attributed to the process of treating the water vapour in the two models. The approach by ATCOR is based on the differential absorption method, using the water absorption bands from the image; whereas in FLAASH water vapour is extracted using three image band ratio methods in combination with a spectral weighted average.

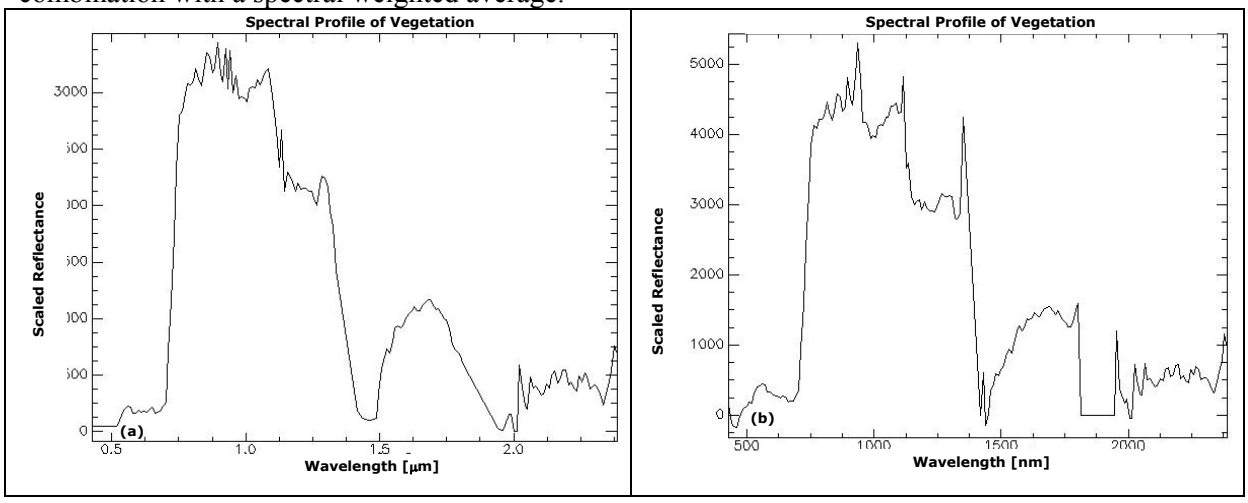

Figure 4-6 Atmospherically corrected vegetation Spectra of Udaipur (a) ATCOR corrected (b) FLAASH corrected

Reflectance from vegetation is dominated by the green leaf interaction with the EMR. ATCOR and FLAASH exhibit clear diagnostic dips at 660 and 668 nm which corresponds to the presence of chlorophyll-b in the healthy leaves (Van der Meer and De Jong, 2003). Shape of the red absorption in ATCOR extracted spectra indicate over estimation it is correctly estimated by FLAASH. Similar results were reported in FLAASH corrected Hyperion datasets (Griffin and Hsiao-hua, 2003). Cellulose causes absorption at 2280 nm in spectra derived from both the models. A diagnostic absorption dip is also seen at 2062 and 2064 nm, which corresponds to the presence of protein and nitrogen in the leaves in ATCOR and FLAASH, respectively.

4.3.2 Water spectra

Water bodies have a different response to EMR than water bound-up in molecules in that they do not exhibit discrete absorption features. Water has a high transmittance for all visible wavelengths, but the transmittance increases with decreasing wavelength. However, suspended material and pigments cause increased reflectance in the visible region (Van der Meer and De Jong, 2003). In the near infra red and in SWIR all EMR is absorbed by water. FLAASH and ATCOR corrected spectra exhibits spurious spikes in 1900 to 2500 nm wavelengths indication over estimation of water vapour absorption (Figure 4-(a) and (b)). Similar observations have been reported in SWIR region (Kruse, 2003).

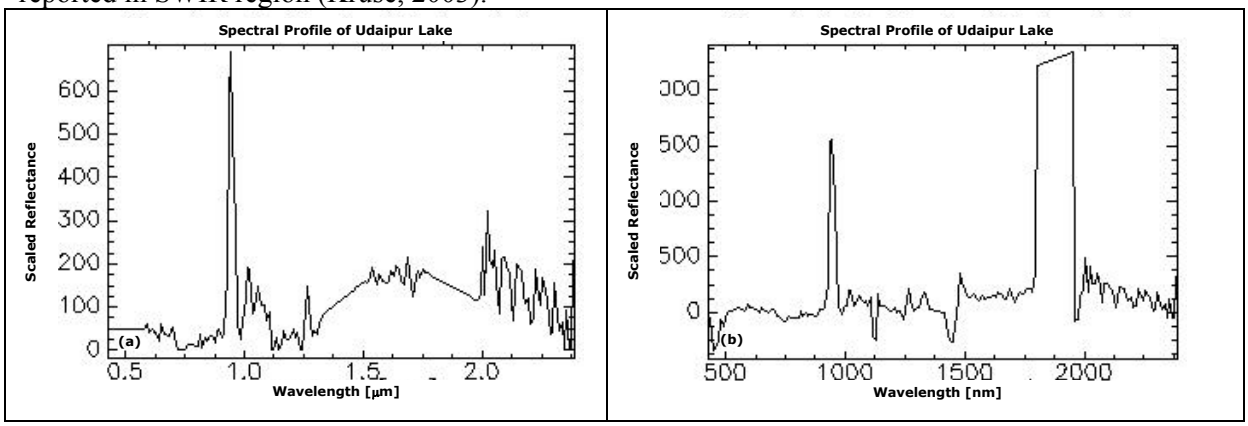

Figure 4-7 Atmospherically corrected waterbody spectra of Udaipur (a) ATCOR corrected (b) FLAASH corrected

This visual analysis of the atmospherically corrected spectra extracted from ATCOR and FLAASH indicate that the over all shapes of the vegetation and water considered here, match very well with each other. However the spectra still has spurious spikes in SWIR region that can not be attributed to any specific feature on ground.

4.3.3 Validation of Radiative Transfer Models

Since two models have been used in the present study, it is very important to estimate their comparative performance. The result from the better performing model can be taken up for further analyzis and mapping. Three statistical parameters were used to validate the performance of the two models. Techniques based on image ratio and difference such as Spectral Angle Mapper (SAM), Euclidean Distance (ED), Normalized Euclidian Distance (NED) provide useful information on spectral similarity between reference and test spectra.

The spectral angle mapper (SAM) has been widely used as a spectral similarity measure. It calculates spectral similarity between the reference reflectance spectrum (ASD spectrum) and

the test spectrum (image spectrum). The angle between two spectra is used as a measure of discrimination. The spectral similarity between the image spectrum (t) and reference spectrum (r) can be expressed as an average angle (θ) between the two spectra for each channel (i) (Van der Meer and De Jong, 2003).

$$\theta = \cos^{-1}\left[\frac{\sum_{i=1}^{n} t_i r_i}{\sqrt{\sum_{i=1}^{n} t_i^2 \sum_{i=1}^{n} r_i^2}}\right]$$

The result of SAM is an angular difference measured in radian ranging from zero to π/2 which gives a qualitative estimate of similarity between image spectrum and ASD spectrum (Van der Meer and De Jong, 2003). Small spectral angle values correspond to high similarity between image spectra and ASD spectra. Larger angle values correspond to less similarity.

Another popular spectral similarity measure is Normalized Euclidean distance (NED), which is also being used to calculate the distance between two spectra as a spectral similarity measure. The Euclidean distance between n-dimension spectra (x) and (y) is given in the equation below.

$$e(x,y) = \sqrt{\sum_{i=1}^{n} (x_i - y_i)^2}$$

The values of ED are positively defined and do not lie within a set range. As Normalized eucledian distance values are invariant to scalar multiplication, NED gives a better scaled measure for comparison (Robila and Gershman, 2005). Their equation is given below.

$$N_x = x / \bar{x}$$

$$NED_{x,y} = e(N_x, N_y)$$

The standard range of SAM calculated is 0 to 90. Lower the angle more is the similarity. The SAM values are rescaled between 0 and 1 in ENVI. The expected NED value ranges from 0 to 1 and is rescaled to 0 to 10 returns a very low value. ED values are positively defined and do not fall within as set interval. The larger number of bands leads to larger value for the distance (Robila and Gershman, 2005). The spectral angle is relatively insensitive to changes in brightness, whereas the normalized values of ED that is NED takes into account the brightness difference between the two vectors, thus giving a better estimate of spectral similarity. The Normalized Euclidean Distance (NED) derived from the Euclidean distance between the reference spectra and image spectra, outperforms most of the measures currently in used.(Robila and Gershman, 2005). SAM and NED values are not specified in value range, value of 0 indicates a perfect match and higher values indicate greater dissimilarity.

4.3.3.1 Spectra Matching Analysis

Use of NED as a spectral similarity measure has been strongly proposed for target detection and has been observed to out perform existing similarity measures. Owing to its computational simplicity and accuracy of results based on target detection experiments using HYDICE (Robila and Gershman, 2005) this measure is chosen for comparing ATCOR and FLAASH extracted spectra with the standard reference spectra. The ASD field spectra of 10 samples from Udaipur were re-sampled to Hyperion band width and were taken as input reference

spectra for the calculation of the spectral similarity measures that is SAM and NED. Table 4.2 shows the SAM and NED for each of the corresponding pixels of the 10 field samples for both the ATCOR as well as FLAASH processed images. Although the average SAM value (0.2015) for ATCOR processed image is smaller than the average SAM value (0.2919) for the FLAASH processed image, it is can not be decisively stated that the ATCOR model performs better than FLAASH model. The reason for this is that the spectral angle is relatively insensitive to changes in brightness (Robila and Gershman, 2005). Also much spectral class confusion have been reported while considering SAM as a similarity measure (Van der Meer, 2006). On comparing the average NED values for ATCOR and FLAASH processed images, it is seen that FLAASH performs better than the ATCOR because the average NED value for FLAASH is 0.7446 which is less that the average NED value for ATCOR (2.79). Since NED values takes into account the brightness difference between the two vectors, thus giving a better estimate of spectral similarity (Robila and Gershman, 2005) it can be inferred from this analysis that FLAASH out performs ATCOR in the case of the Udaipur data set.

Table 4.2 Values of spectral measures calculated for ACTOR and FLAASH corrected images for Udaipur

Sample code	**SAM ATCOR**	**SAM FLAASH**	**NED ATCOR**	**NED FLAASH**
1	0.2086	0.2625	4.1537	1.1014
2	0.2601	0.3308	1.6669	0.4109
3	0.2007	0.2853	1.1567	0.4242
4	0.3302	0.5111	3.7595	1.1763
6	0.0902	0.2095	3.7743	0.7764
7	0.1801	0.2763	1.57	0.3679
8	0.1934	0.2581	3.9349	0.9057
9	0.1803	0.2519	3.2694	0.8549
12	0.1338	0.2322	0.8805	0.4836
13	0.2385	0.3019	3.7696	0.945
Average	**0.2015**	**0.2919**	**2.79**	**0.7446**

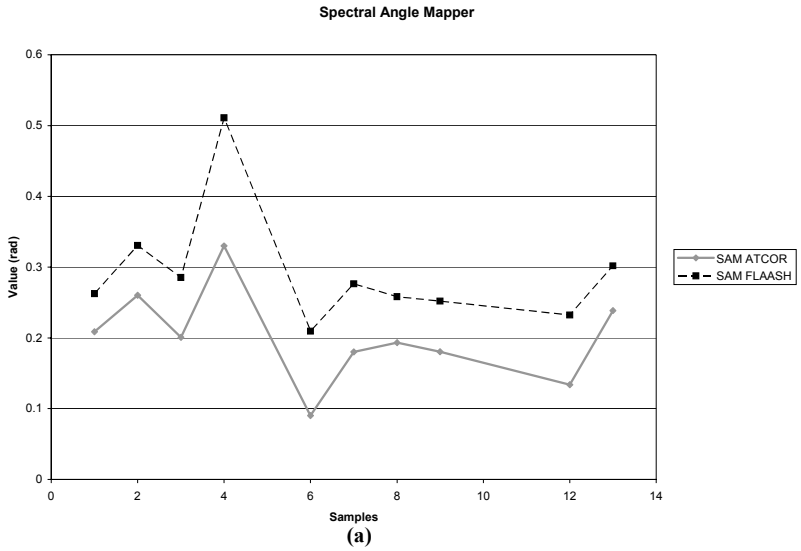

(a)

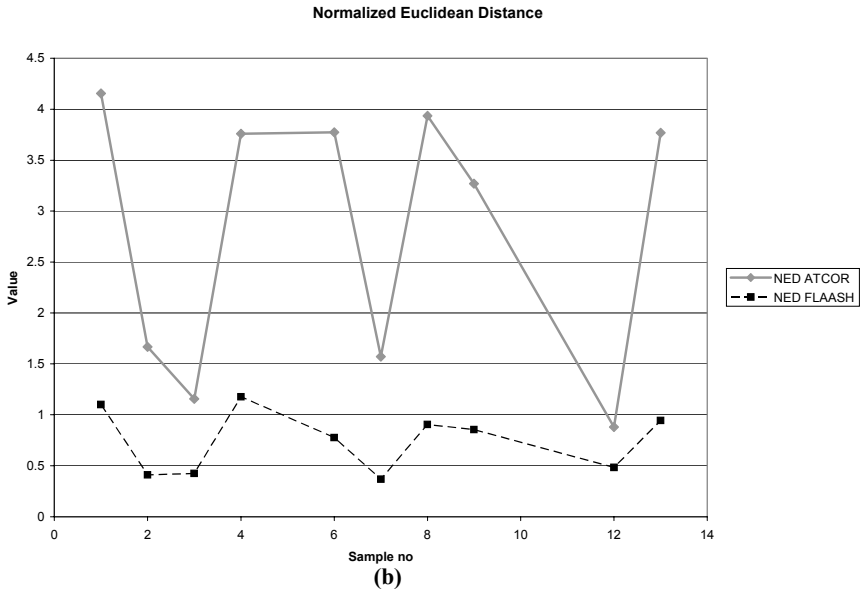

Figure 4.8 SAM (a) and NED (b) values for FLAASH and ATCOR models for Udaipur dataset

Expected ranges of values for SAM are 0 to 1 and for NED 0 to 10. Lower the value more is the similarity to the ASD reference spectra.

The ASD field spectra of 11 samples from Orissa were re-sampled to Hyperion band width and were taken as input reference spectra for the calculation of the spectral similarity measures such as SAM and NED. The average SAM value (0.1472) for the ATCOR processed image is lower than the SAM value (0.2086) for the FLAASH processed one, which explains that the ATCOR atmospheric correction model had performed better than the FLAASH model. Similarly the average NED value (1.0934) for the FLAASH processed image is much lower than the average NED value (3.096) for ATCOR processed image which reflects the better performance of the FLAASH model when compared to that of the ATCOR model.

Similarly the spectral matching measures for Orissa hyperion data set have been calculated for ATCOR and FLAASH results and given below.

Table 4.3 Values of spectral measures calculated for ACTOR and FLAASH corrected images for Orissa

Sample code	SAM ATCOR	SAM FLAASH	NED ATCOR	NED FLAASH
1	0.1043	0.1669	4.2357	1.6843
2	0.1625	0.2293	1.7143	0.4939
3	0.2014	0.2785	2.5764	1.4460
4	0.2142	0.2560	3.9872	1.4016
5	0.1419	0.2024	4.3851	1.4218

Sample code	SAM ATCOR	SAM FLAASH	NED ATCOR	NED FLAASH
6	0.1651	0.2252	2.8923	1.4336
7	0.1623	0.2218	4.2357	1.0837
8	0.0923	0.1514	2.3416	0.4016
10	0.0904	0.1438	2.8545	1.1049
11	0.1347	0.1866	2.1816	0.7883
Average	**0.1472**	**0.2086**	**3.096**	**1.0934**

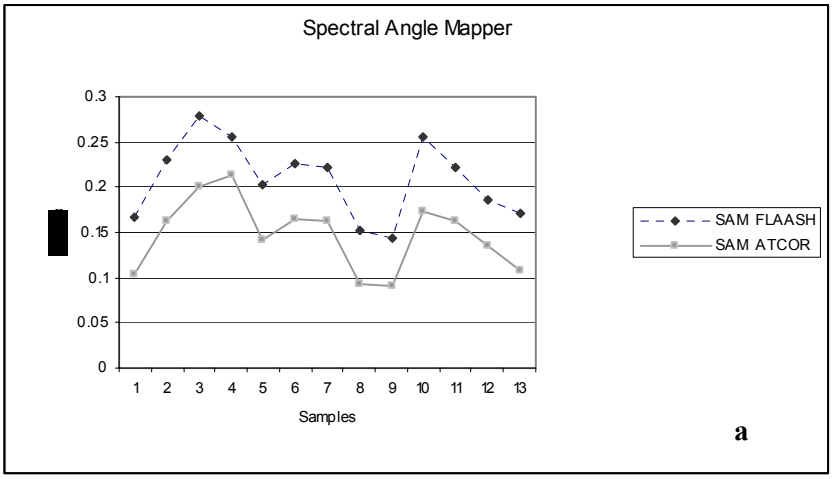

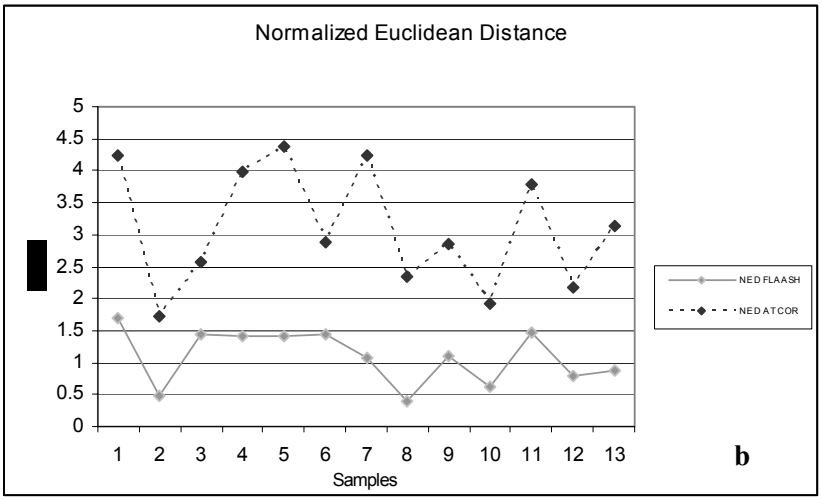

Figure 4.9 SAM (a) and NED (b) values for FLAASH and ATCOR models for Orissa dataset

The results show that the FLAASH atmospheric correction model had given much better results when compared to that delivered by the ATCOR2 model. As a result of this the reflectance image retrieved for the FLAASH model has been used for the further spectral analysis and

mineral abundance mapping. The choice of the two results is very much subjective to the kind of study aimed at. FLAASH results are preferred for the mineral targeting where as for the absorption depth analysis the ATCOR2 results are more useful.

4.3.4 ASD Reference Spectra

The samples collected during field investigation have been used to generate the reflectance spectra using Analytical spectral device (ASD). These spectras from both the study areas have been inturn used as reference spectra for the above mentioned spectral matching analysis. The 10 spectras from Udaipur and 11 spectras from Orissa have been used to generated the reference spectral library.

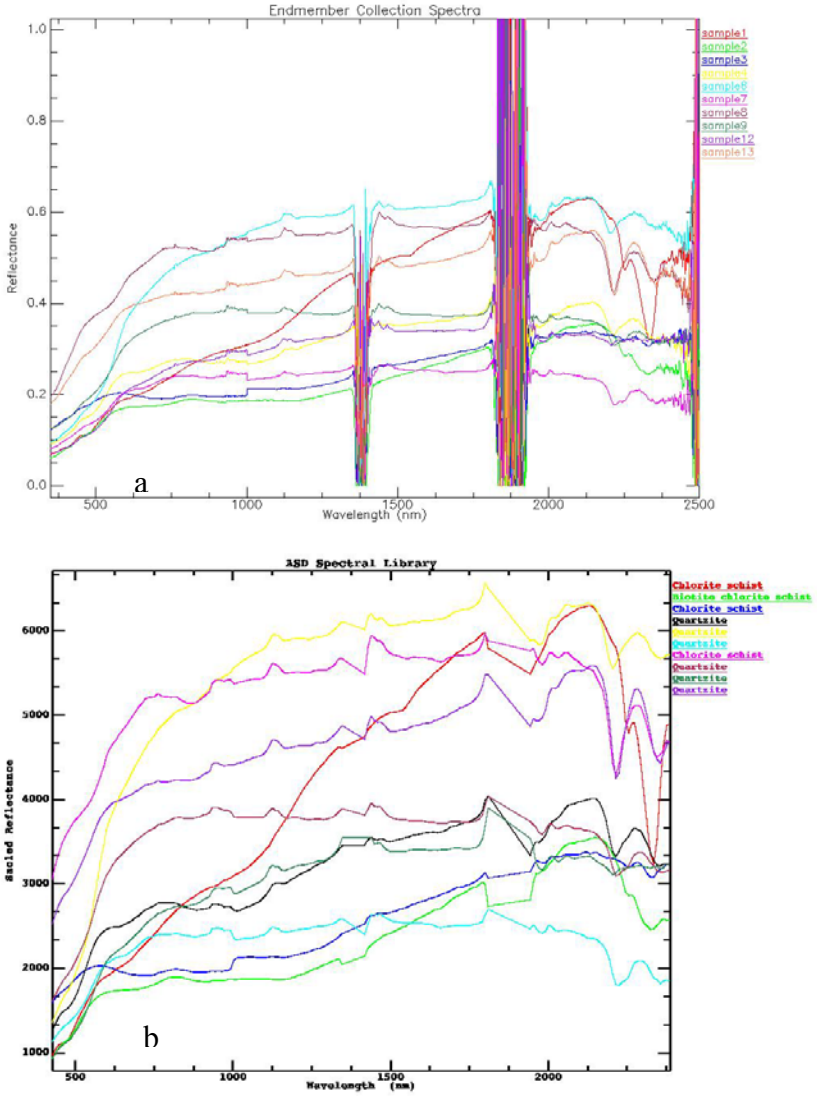

Figure 4.10 (a) Primary ASD spectra of the samples from Udaipur and (b) resampled spectra

4.4 Spectral Polishing

The spectra generated by the atmospheric correction model need to be optimized for their slight aberrations present here and there. As mentioned earlier they are not indicators of any intrinsic characteristics or properties of the object or target sensed. Hence it is advisable to remove these artifacts from the spectra using the EFFORT algorithm incorporated in the ENVI software. This results in smooth spectra which do not remove any specific absorption depths or reflectance peaks of the target specific spectra.

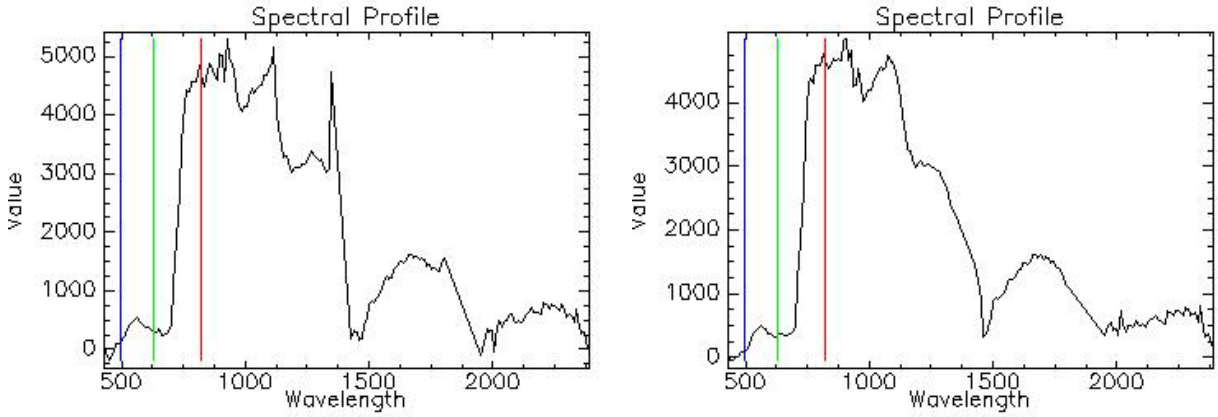

Figure 4.11 Unpolished and polished reflectance spectra

4.5 Spectral Analysis Results

4.5.1 Band Rationing Results

The band rationing technique was applied for both the LISS IV satellite dataset. For mineral mapping ratio images were prepared using the LISS 4 images of both the study areas. They were prepared by dividing the digital number (DN) in one band by the corresponding DN in another band for each pixel, stretching the result value and plotting the new values as an image. This method is used by (Weissbrod et al. 1985; Cappiccioni et al. 2003; Edgardo 1992) to extract spectral information from multi-spectral imagery. The ratio of LISS 4 band 2 and band 3 (2/3) renders most of the area in rather dark gray or bright grey, which corresponds to zones of strong hematitic alteration. The Spectral response of the weathered iron minerals has weak reflectance in the blue region (band2) and strong reflectance in the red region (band 3), so the ratio 2/3, which has high values can be used for iron oxide mapping in Orissa area.

Absorption caused by kaolinite, montmorillonite and clay minerals results in low reflectance in band 1 and high reflectance in band 2. So, the ratio image 2/1 would have bright signatures for clay minerals in udaipur study area. The ratio images of the both the study areas are given in figure 4.38 and 4.39

4.5.2 Minimum Noise Fraction Results

As explained in section 3.13.1.1 MNF transformation is used to reduce the dimensionality of the hyperspectral dataset by segregating the noise in the data. The MNF transform is a linear transformation which is essentially two cascaded Principal Component Analysis (PCA) transformations.

Forward MNF transformation has been run on both the Hyperion datasets of Orissa and Udaipur. Several trials of Minimum Noise Fraction transformation have been run to obtain the optimum results. The first 20 eigenvectors were chosen for both the datasets and the rest of them were more noise prone hence discarded from further spectral analysis.

The selected eigenvectors and eigenvalues are shown below that have been determined for the Orissa dataset.

MNF	Eigen value	Percent
1	28.4522	7.93%
2	23.3915	14.46%
3	19.1074	19.78%
4	14.1012	23.72%
5	7.6645	25.85%
6	7.2164	27.87%
7	5.5410	29.41%
8	4.6323	30.70%
9	4.3808	31.92%
10	4.1776	33.09%
11	3.3874	34.03%
12	3.2665	34.94%
13	3.1631	35.83%
14	2.8790	36.63%
15	2.6532	37.37%
16	2.6452	38.11%
17	2.5597	38.82%
18	2.4663	39.51%
19	2.4397	40.19%
20	2.3799	40.85%

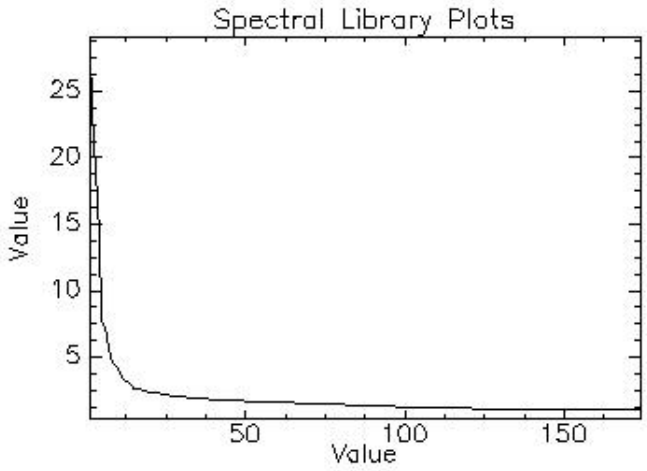

Figure 4.12 MNF Eigen value plot for Orissa

Similarly the Minimum Noise Fraction (MNF) for the Udaipur dataset was also estimated. The resultant Eigen values and their percentages are given below.

MNF	Eigenvalue	Percent
1	129.0848	29.76%
2	23.0186	35.06%
3	12.4663	37.94%
4	8.1733	39.82%
5	7.1416	41.47%
6	6.5286	42.97%
7	5.3989	44.22%
8	5.1247	45.40%
9	3.9245	46.30%
10	3.5608	47.12%
11	3.4748	47.93%
12	3.4215	48.71%
13	3.0756	49.42%
14	2.9336	50.10%
15	2.6197	50.70%

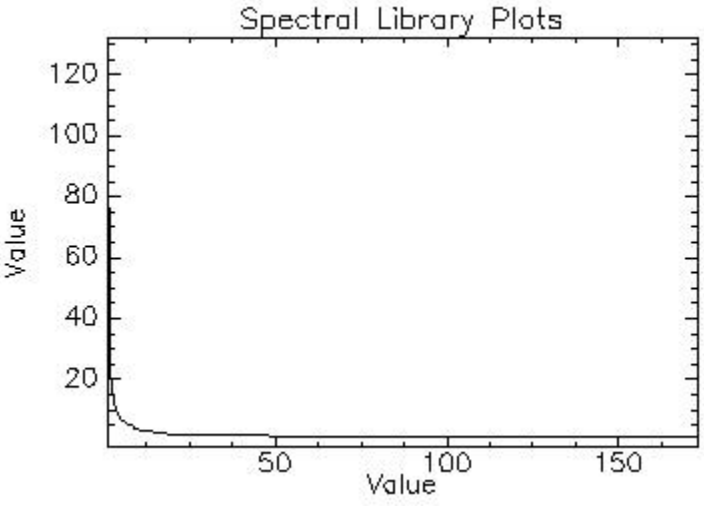

Figure 4.13 MNF Eigen value plot of Udaipur dataset

16	2.4534	51.27%
17	2.3512	51.81%
18	2.2905	52.34%
19	2.2153	52.85%
20	2.1993	53.36%

4.5.3 Pixel Purity Index

The pixel purity index image was determined on the MNF image for both the Orissa and Udaipur datasets. The number of iterations was chosen as 10000 with 250 iterations per block, given a threshold of 3. The threshold were changed and tested on various MNF images of both the hyperion datasets. The threshold value of 3 has given the best results and it has been chosen for further selection of the region of interests (ROIs).

4.5.4 Endmembers Selection

The endmember needs to be selected for the abundance mapping using various mapping methods such as Linear Spectral Unmixing (LSU), Spectral Angle Mapper (SAM), Mixed Tuned Matched Filtering (MTMF), Matched Filtering etc. The various endmembers are chosen with respect to their relevance in the study area. For both the Udaipur and Orissa, the geologically relevant features are chosen as endmembers.

In the Orissa study area, all the relevant topographic features are clustered in the N-Dimensional visualizer and demarcated as separate region of interests and saved. These ROI'S were used for the further mapping using various techniques. The endmembers clustered in the Orissa study area are as follows.

1. Water
2. Vegetation
3. Hematite ore
4. Mine tailings
5. Alluvium.

The study area is a reserve forest and has the largest cluster of mines in India. The area doesn't have any rock exposures. For accurate mapping using linear spectral mapping, all the land features need to be extracted.

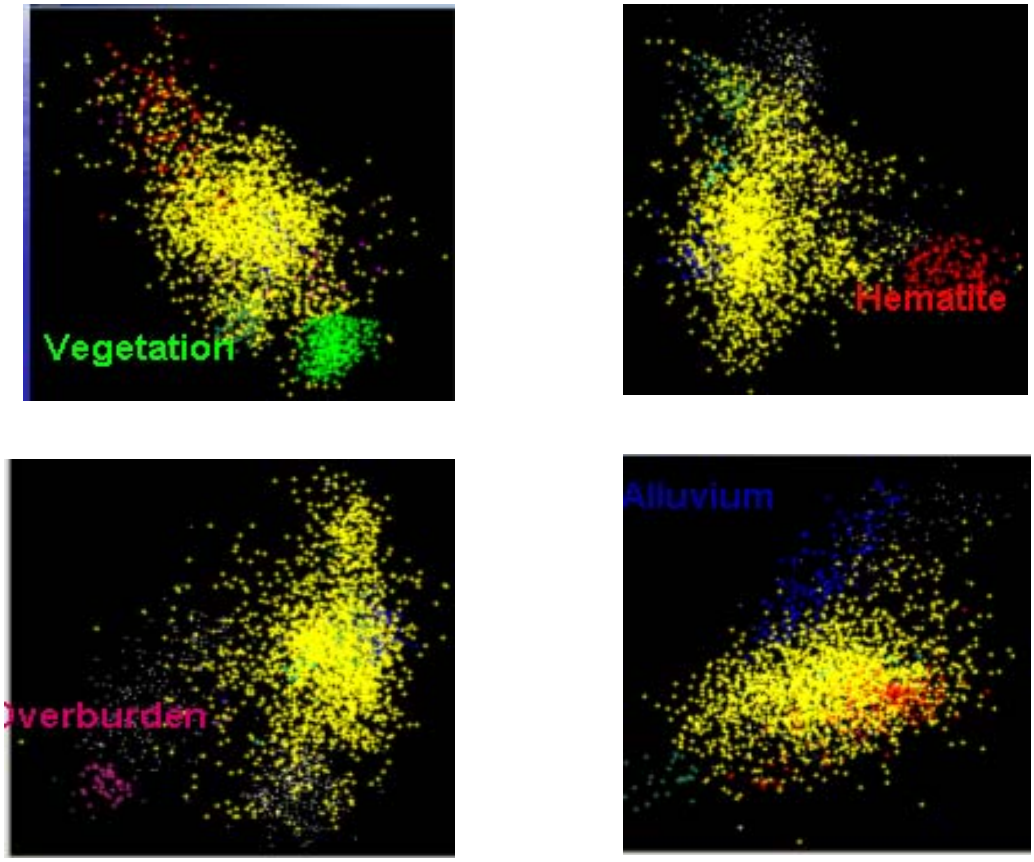

Figure 4. 14 Endmember selection in N-Dimensional visualizer (Orissa)

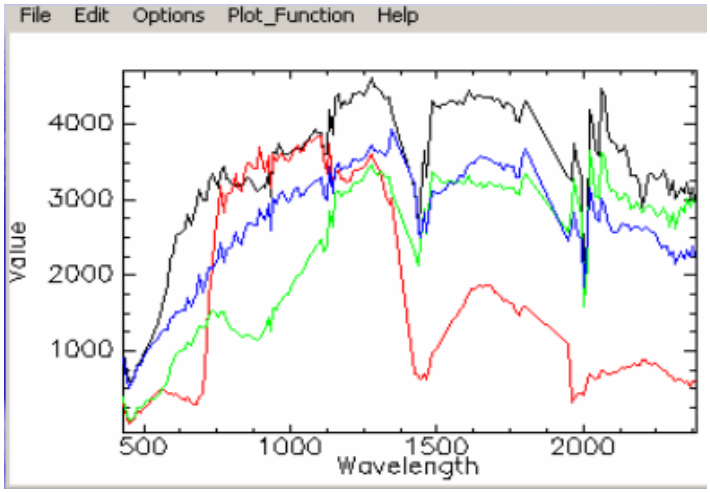

OVERBURDEN
HEMATITE
ALLUVIUM
VEGETATION

Figure 4.15 Endmember spectra collected from Orissa hyperion dataset

4.6 Characteristics of endmembers of Orissa dataset

The spectral as well as the mineralogical aspect of each endmember demarcated from the N-Dimensional visualizer is discussed in the below section.

4.6.1 Hematite

Hematite, also spelled as Haematite, is the mineral form of iron oxide (Fe_2O_3). Hematite crystallizes in the rhombohedral crystal system. Hematite is a very common mineral, colored black to steel or silver-gray, brown to reddish brown, or red. It is mined as the main ore of iron. Hematite is harder than pure iron, but much more brittle.The name hematite is derived from the Greek word for blood (haima) because hematite can be red, as in rouge, a powdered form of hematite. The color of hematite lends it well in use as a pigment. Clay-sized hematite crystals can also occur as a secondary mineral formed by weathering processes in soil, and along with other iron oxides or oxyhydroxides such as goethite, is responsible for the red color of many tropical, ancient, or otherwise highly weathered soils.

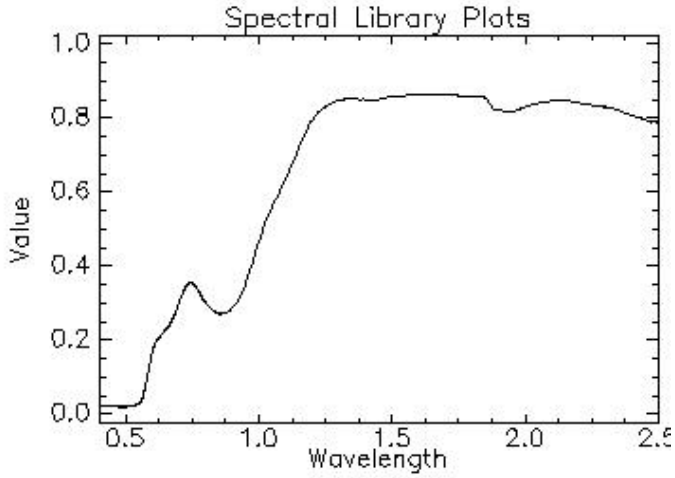

Figure 4.16 Hematite spectra from USGS spectral library

The hematite spectra have certain diagnostic absorption depths. The absorption depth at 0.87 μm is the most characteristic of hematite. This absorption depth is also seen in the image spectra of the Orissa dataset. This absorption depth at 0.87 μm is basically due to the crystal field effect of transition element “Fe”.

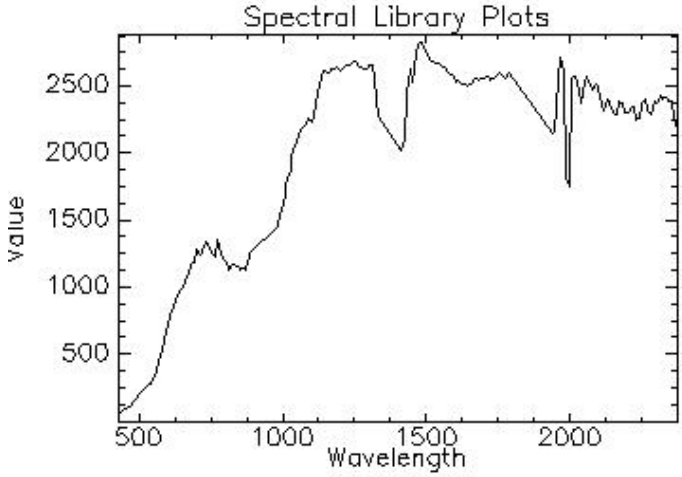

Figure 4.17 Hematite Spectra from hyperion image

4.6.2 **Alluvium**

Spectral reflectance characteristics of soils are the result of their physical and chemical properties and are influenced largely by the compositional nature of soils in the main components are inorganic solids, organic matter, air and water. During the field investigation it was noticed that the alluvium present in the study area are mainly derived from the weathering of the iron bearing banded iron formation. This results in iron rich alluvium showing diagnostic reddish to yellowish colour. The spectra collected from the alluvium pixel indicate this inference with their corresponding characteristic absorption depth and water absorption at 1.4 and 1.9 μm..

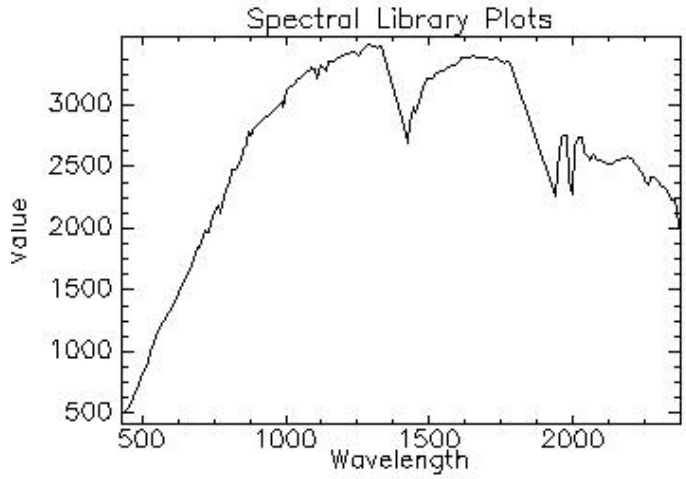

Figure 4.18 Alluvium spectra from Hyperion image

4.6.3 **Mine tailings**

The mine tailings present in the study area comprises of alluvium, low grade iron ore and boulders of banded iron formations. The spectra generated from the mine tailings shows the diagnostic characteristics of the alluvium as well as the hematite iron ore. The absorption depth at 0.87 μm which is characteristic of Hematite is also seen in the mine tailing's spectra. The general trend of the spectra resembles that of the alluvium with deep absorption depths at 1.4 and 1.9 μm due to water absorption.

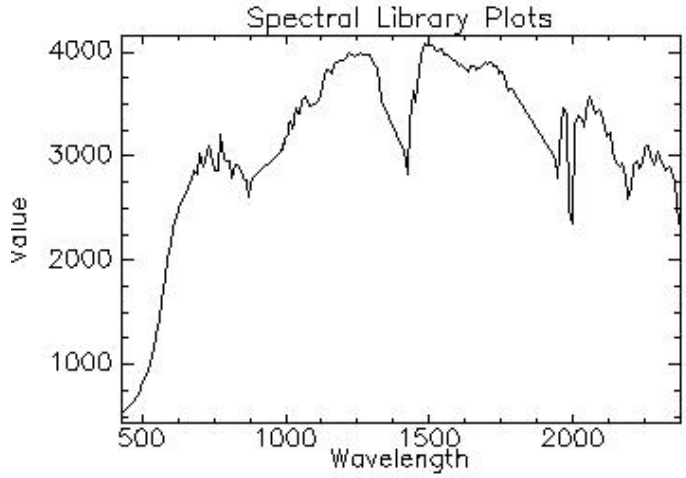

Figure 4.19 Mine tailing spectra from hyperion image

4.7 Characteristics of endmembers of Udaipur study area

The endmembers selected from the Udaipur study area are as follows.

1. Kaolinite
2. Montmorillonite
3. Pyrophyllite
4. Chlorite

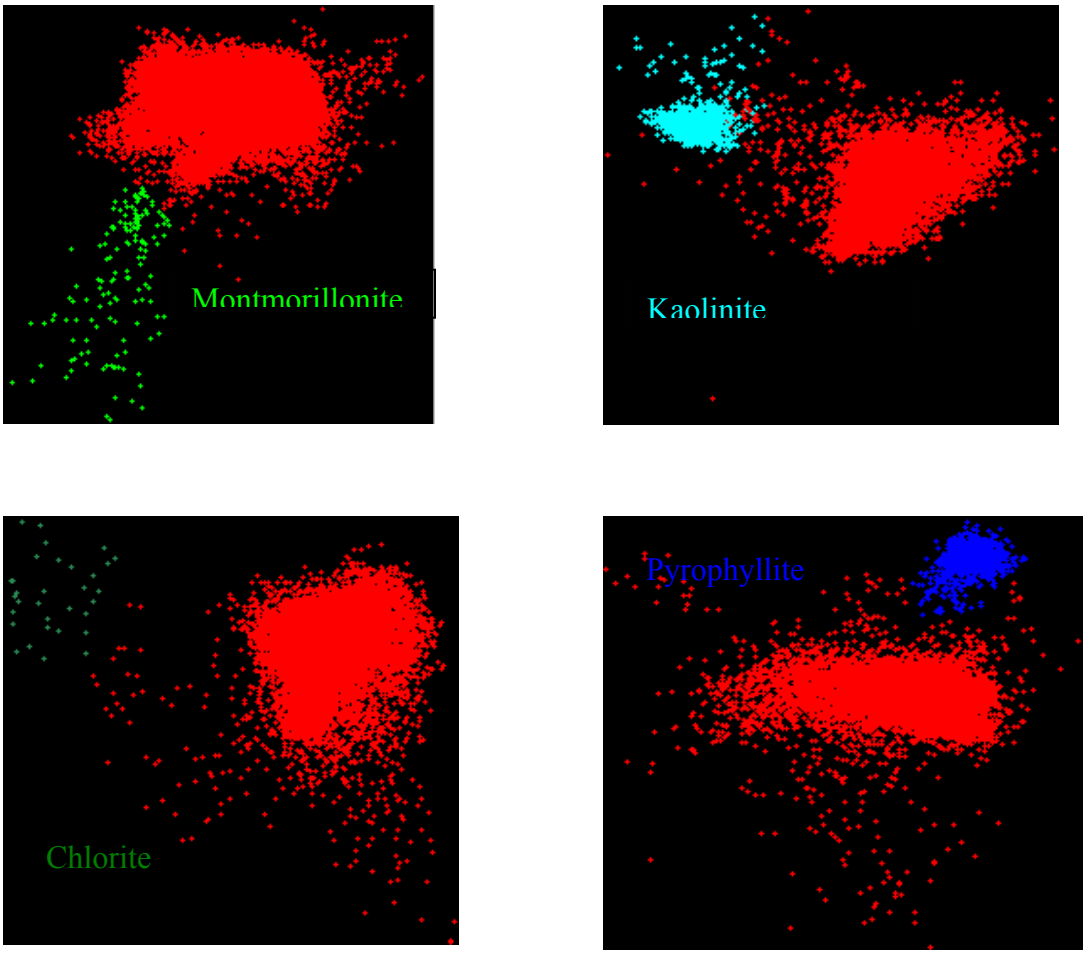

Figure 4.20 Endmember collection in N-Dimensional Visualizer (Udaipur)

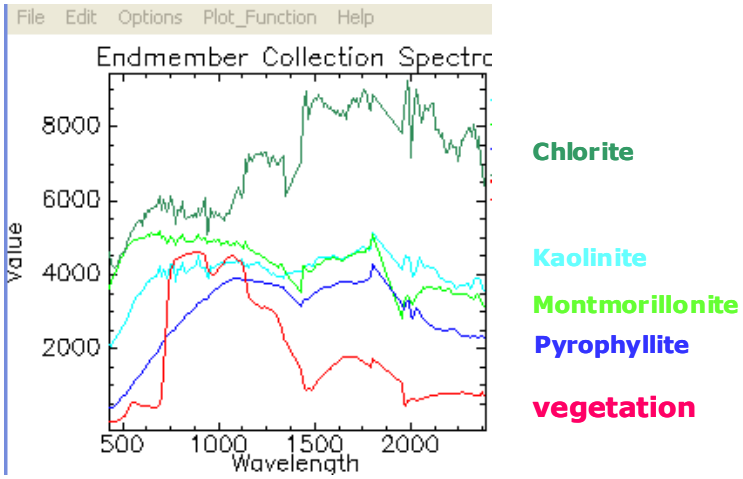

Figure 4.21 Endmember spectra collected from Udaipur hyperion dataset

4.7.1 Clay Minerals

Clay minerals are hydrous aluminium phyllosilicates, sometimes with variable amounts of iron, magnesium, alkali metals, alkaline earths and other cations. Clays have structures similar to the micas and therefore form flat hexagonal sheets. Clay minerals are common weathering products (including weathering of feldspar) and low temperature hydrothermal alteration products. Clay minerals are very common in fine grained sedimentary rocks such as shale, mudstone and siltstone and in fine grained metamorphic slate and phyllite.

Clay minerals include the following groups,

1. Kaolinite group which includes the minerals kaolinite, dickite, halloysite and nacrite. Some sources include the serpentine group due to structural similarities (Bailey 1980).

2. Smectite group which includes pyrophyllite, talc, vermiculite, sauconite, saponite and montmorillonite

3. Illite group which includes the clay-micas. Illite is the only common mineral.

4. Chlorite group includes a wide variety of similar minerals with considerable chemical variation.

4.7.1.1 Kaolinite ($Al_2Si_2O_5(OH)_4$)

Kaolinite is a clay mineral with the chemical composition $Al_2Si_2O_5(OH)_4$. It is a layered silicate mineral, with one tetrahedral sheet linked through oxygen atoms to one octahedral sheet of alumina octahedra. Rocks that are rich in kaolinite are known as china clay or kaolin.The name is derived from Gaolin ("High Hill") in Jingdezhen, Jiangxi province, China. Kaolinite was first described as a mineral species in 1867 for an occurrence in the Jari River basin of Brazil.[3]

Kaolinite is one of the most common minerals; it is mined, as kaolin, in Brazil, France, United Kingdom, Germany, India, Australia, Korea , the People's Republic of China, and the USA.

Kaolinite has a low shrink-swell capacity and a low cation exchange capacity (1-15 meq/100g.) It is a soft, earthy, usually white mineral (dioctahedral phyllosilicate clay), produced by the chemical weathering of aluminium silicate minerals like feldspar. In many parts of the world, it is colored pink-orange-red by iron oxide, giving it a distinct rust hue. Lighter concentrations yield white, yellow or light orange colours. Alternating layers are sometimes found, as at Providence Canyon State Park in Georgia, USA.

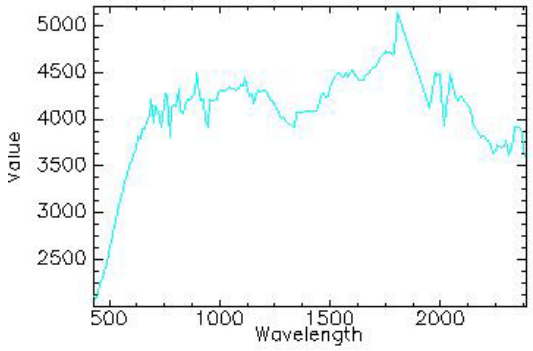

Figure 4.22 Image spectra of Kaolinite

The spectral characteristics of clay minerals are mainly concentrated in the SWIR portion of the electromagnetic spectrum. Spectroscopic indicators are of great interest because reflectance spectra show absorption bands in the visible and near-infrared (NIR) region, which permit identification of clay minerals in natural soils.and, then the strong absorption bands at 1400 nm and 1900 nm are due to bound water. The strong OH bands at 1400 nm and 2200 nm are typical of Kaolinite (Hunt and salisbury, 1970). The Al-OH overtone-combination absorption band around 2200-2300 nm is very diagnostic of all clay minerals. Short Wave Infrared (SWIR) part of the spectrum, 1400-2500 nm, and particularly the SWIR2, 1900-2500 nm, are the most useful part of the spectrum for the identification of clays. Kaolinite shows doublet absorption bands at 1400 nm and 2200 nm that are characteristic of the mineral.

4.7.1.2 Montmorillonite

Montmorillonite is a very soft phyllosilicate mineral that typically forms in microscopic crystals, forming a clay. It is named after Montmorillon in France. Montmorillonite, a member of the smectite family, is a 2:1 clay, meaning that it has 2 tetrahedral sheets sandwiching a central octahedral sheet. The particles are plate-shaped with an average diameter of approximately 1 micrometre. Montmorillonite's water content is variable and it increases greatly in volume when it absorbs water. Chemically it is hydrated sodium calcium aluminium magnesium silicate hydroxide $(Na,Ca)_{0.33}(Al,Mg)_2(Si_4O_{10})(OH)_2{\cdot}nH_2O$. Potassium, iron, and other cations are common substitutes, the exact ratio of cations varies with source. It often occurs intermixed with chlorite, muscovite, illite, cookeite and kaolinite.

Montmorillonite swells with the addition of water. However, some montmorillonites expand considerably more than other clays due to water penetrating the interlayer molecular spaces and concomitant adsorption. The amount of expansion is due largely to the type of exchangeable cation contained in the sample. The presence of sodium as the predominant exchangeable cation can result in the clay swelling to several times its original volume.

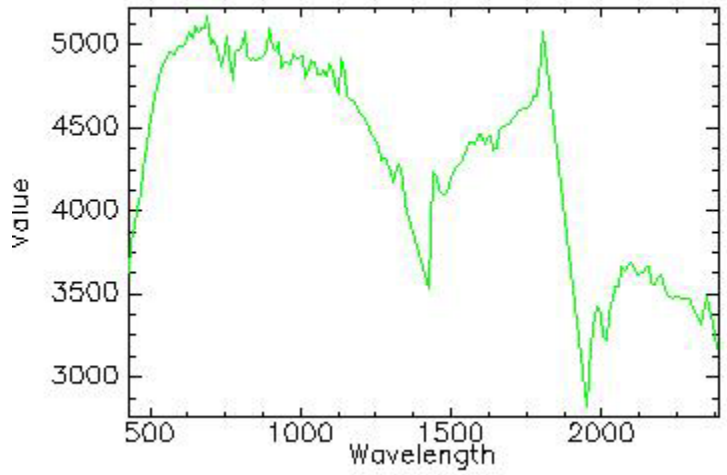

Figure 4.23 Image spectra of Montmorillonite

The spectral characteristics of Montmorillonite is very much similar to that of Kaolinite. The absorption depth at 1395 and 1415 nm for the OH overtones and 2163 and 2208.5 nm for the combination of AL-OH bend plus OH stretch are very unique for Montmorillonite among the clay minerals. Montmorillonite exhibits a well defined single absorption band around 2200 nm due to the combination of the above mentioned facts. Montmorillonite often shows shift in the 2200 nm absorption depth and this can be attributed to their mineral composition. This shift is mainly due to the increase in the content of calcium (Ca) and decrease in the sodium (Na) content. Hence this absorption depth is very critical in understanding the swelling potential of Montmorillonite. The sodium rich montmorillonites swell more than calcium rich montmorillonites. The shift in the 2200 nm absorption band has been attributed to interaction with interlayer cation held (Ryskin, 1974).

4.7.1.3 Chlorite

The chlorites are a group of phyllosilicate minerals. Chlorites can be described by the following four endmembers based on their chemistry via substitution of the following four elements in the silicate lattice; Mg, Fe, Ni, and Mn.

Clinochlore: $(Mg_5Al)(AlSi_3)O_{10}(OH)_8$
Chamosite: $(Fe_5Al)(AlSi_3)O_{10}(OH)_8$
Nimite: $(Ni_5Al)(AlSi_3)O_{10}(OH)_8$
Pennantite: $(Mn,Al)_6(Si,Al)_4O_{10}(OH)_8$

The range of chemical composition allows chlorite group minerals to exist over a wide range of temperature and pressure conditions. For this reason chlorite minerals are ubiquitous

minerals within low and medium temperature metamorphic rocks, some igneous rocks, hydrothermal rocks and deeply buried sediments. Chlorite is a common metamorphic mineral, usually indicative of low-grade metamorphism. In Udaipur, they are commonly found in areas where there is large exposures of Phyllite and Schist.

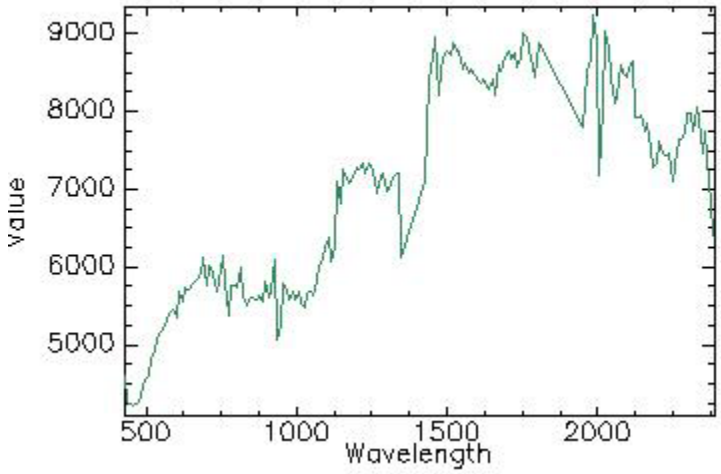

Figure 4.24 Image spectra of Chlorite

The variety found in Udaipur is Chamosite. They are iron rich chlorite with characteristic Fe absorption depth at 875 nm.

4.7.1.4 Pyrophyllite

Pyrophyllite is a phyllosilicate mineral species belonging to the clay family and composed of aluminium silicate hydroxide: $AlSi_2O_5OH$. Alkaline aluminum silicate (28.3% Al_2O_3 ; 66.7% SiO_2 ; 5.0% H_2O). It occurs in two more or less distinct varieties, namely, as crystalline folia and as compact masses.

Pyrophyllite occurs in phyllite and schistose rocks, often associated with kyanite, of which it is an alteration product. Pale green foliated masses, very like talc in appearance, are found at Beresovsk near Yekaterinburg in the Urals, and at Zermatt in Switzerland. The most extensive deposits are in the Deep region of North Carolina, where the compact variety is mined, and in South Carolina and Georgia. Major deposits of pyrophyllite occur within the region of Ottosdal, South Africa, where it is mined for the production of a variety of manufactured goods and blocks are quarried and marketed as "Wonderstone" for the carving of sculptures. In Australia, pyrophyllite has been mined at three sites near Pambula on the Sapphire Coast of NSW.

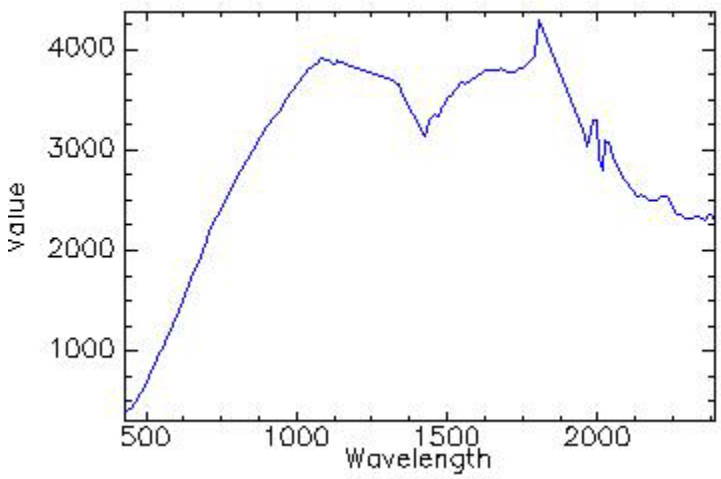

Figure 4.25 image spectra of pyrophyllite

The spectral absorption depths in the pyrophyllite spectra is basically concentrated in the infrared portion of the spectrum mainly around 2160 and 2320 nm. These absorption depths are mainly due the Al-OH concentration which is typical of clay minerals. Another strong band absorption is centered around 1390 nm which is attributed to the water molecule absorption.

4.8 Results of various mapping techniques

Various mapping techinues were used in the present study to map the minerals that have been demarcated using the endmember collection. Linear spectral unmixing Mixed tune match filtering (MTMF) and spectral feature fitting were used for this purpose.

4.8.1 Results of Linear Spectral Unmixing (Udaipur)

Linear spectral unmixing has been performed using the five endmembers of the Udaipur study area. The results of this mapping technique for both the study areas are discussed below.

Linear spectral unmixing images produced for the Udaipur study area have been generated by the giving endmember region of interest as the reference spectra and their abundances in the image are given in the resultant final linear spectral unmixing image. This models gives information about the relative abundances of the endmember material considering each endmember present in a pixel. Five endmembers for the Udaipur and three endmembers for the Orissa dataset have been used to describe the resultant image. The five resultant endmember abundance image and the rms image is shown below.

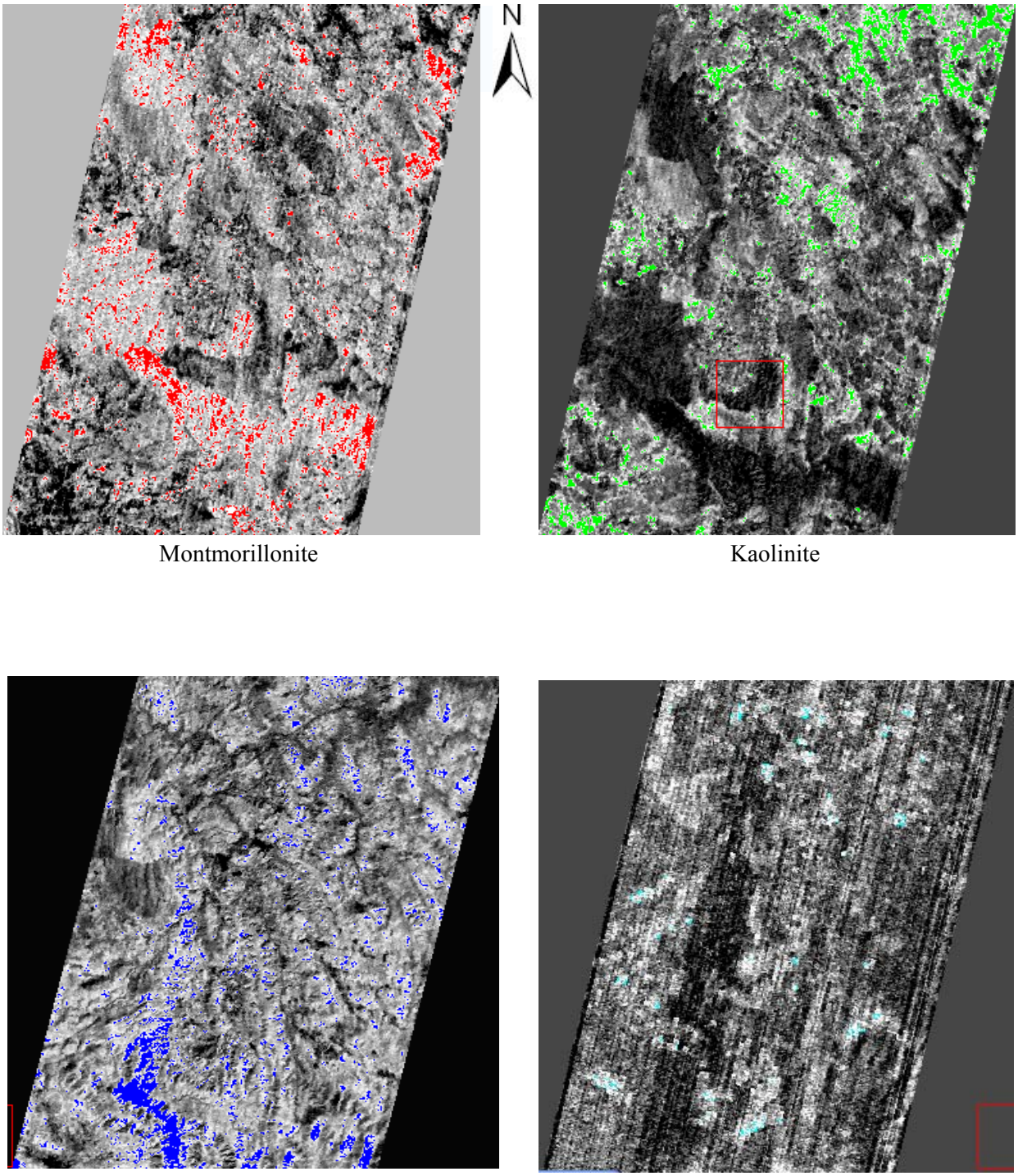

Montmorillonite Kaolinite

Pyrophyllite Fe rich Chlorite (Chamosite)

Figure 4.26 linear spectral unmixing results for Udaipur (approximate map scale 1:61,400)

The linear spectral unmixing results of the udaipur study area clearly demarcates the clay minerals kaolinite and Montmorillonite. This is basically due to the mineral composition of the

two minerals. It is the characteristic absorption depth at 2160 nm enables these minerals to be distinguished in the image. The abundance image of pyrophyllite exhibits areas of intermixing existance with the montmorillonite. This makes them obscure to identify in the image. The abundance of iron rich chlorite (Chamosite) is very sparse. Due to their unique Fe absorption depth at 875 nm, their presence has also been succesfully mapped using the linear spectral unmixing model.

4.8.2 Results of Spectral Feature Fitting (Udaipur)

According to the principle of SFF a scale image and one rms image is the output for each reference spectrum or a combined "fit" (scale/rms) image is output for each refernce spectrum. The scale image is a measure of absorption feature depth, which is related to material abundance, and the rms image shows the error percenatge in the scale image. Therefore the brighter pixel in the scale image (corresponding to low rms error) indiactes a better match to the reference spectrum. Since here the spectra are devoid of any absorption feature this method did not give suitable result for different enmembers.

The images calculated for each endmember did not show any noticeable variability or discriminability among themselves. Hence it can be concluded that the technique of SFF (Spectral Feature Fitting) is not the appropriate mapping tecnique where absorption depths of individual endmember mineral is not taken into consideration. The results of each endmember images are given below. The vegetation spectra was also taken as an endmember for the SFF mapping method. This model was not appropriate even for the mapping of vegetated area.

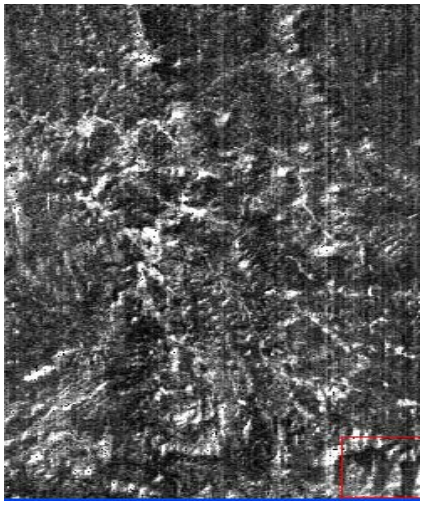

Kaolinite

Montmorillonite

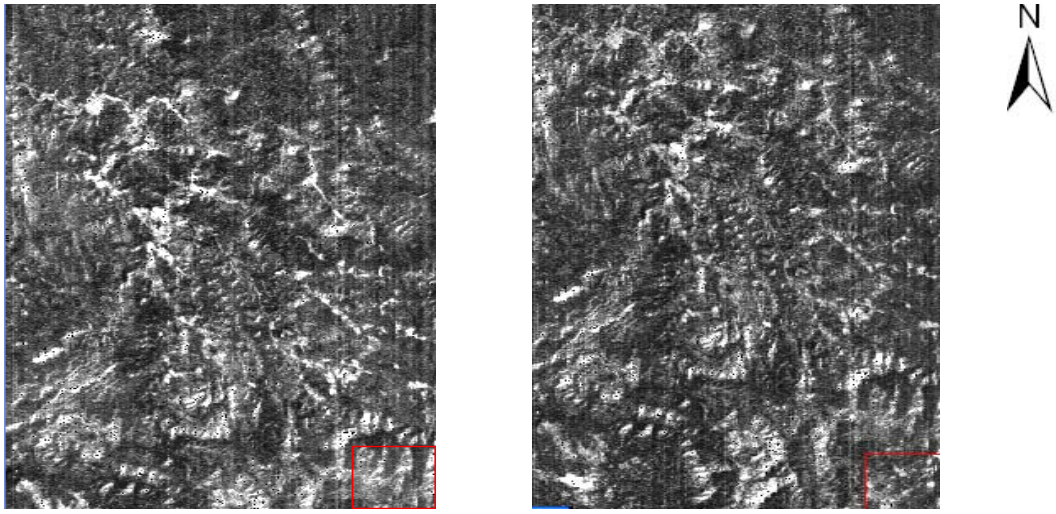

Pyrophyllite Chamosite

Figure 4.27 Spectral feature fitting results for Udaipur endmembers (approximate map scale 1:40,528)

4.8.3 Results of Mixture Tuned Matched Filtering (Udaipur)

Image endmembers are derived from the hyperion satellite imagery using the interactive analysis technique of ENVI. All the four image endmembers mostly describing the image were considered for creating a set of score and infeasibility image.

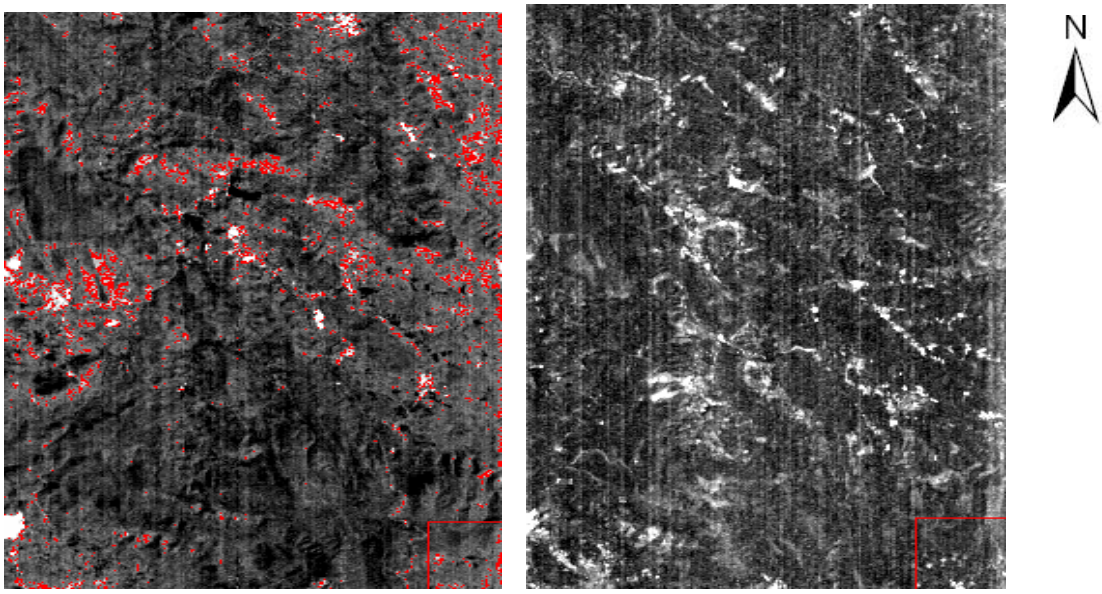

Kaolinite (score) Kaolinite (infeasibility)

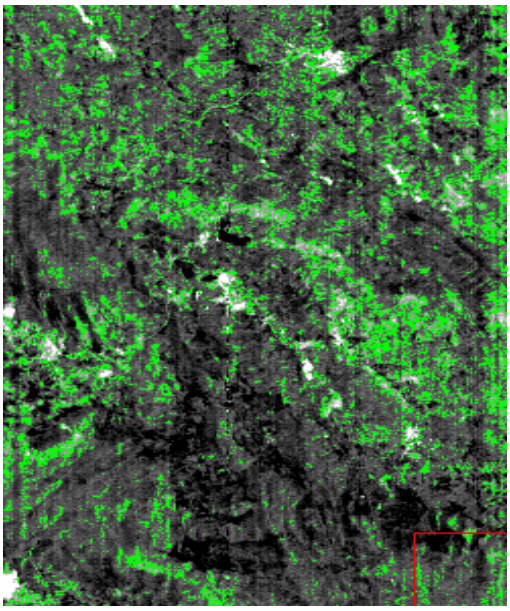

Montmorillonite (Score)

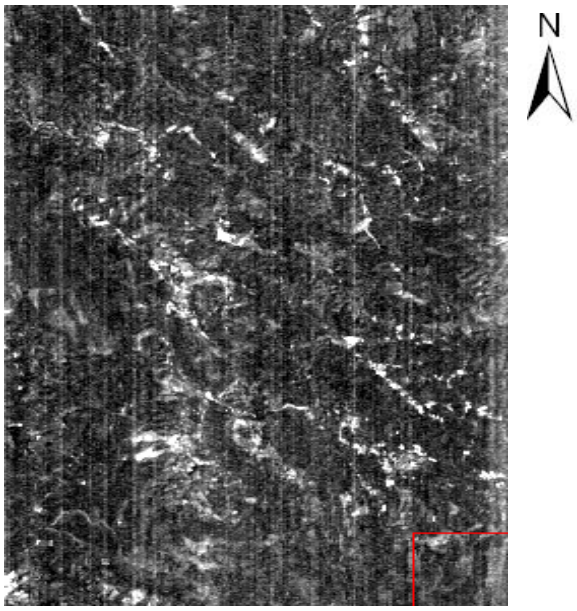

Montmorillonite (Infeasibility)

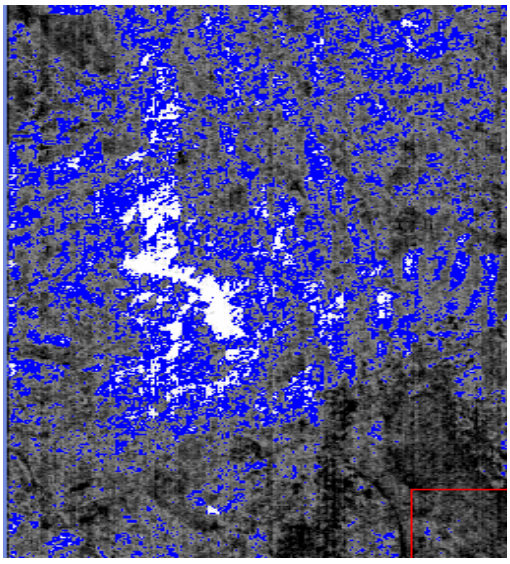

Pyrophyllite (Score)

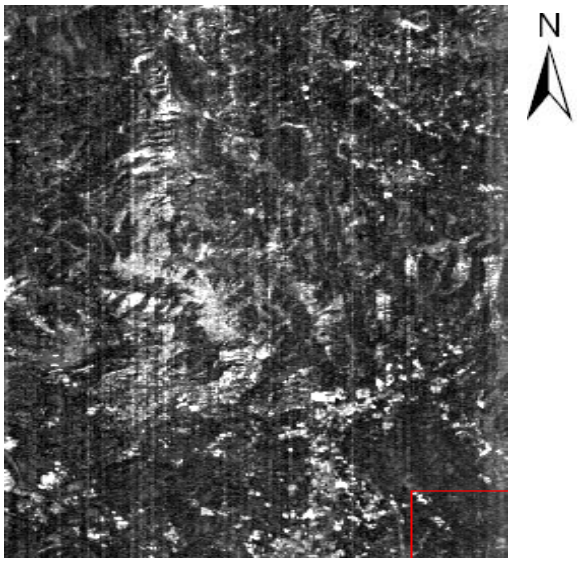

Pyrophyllite (Infeasibility)

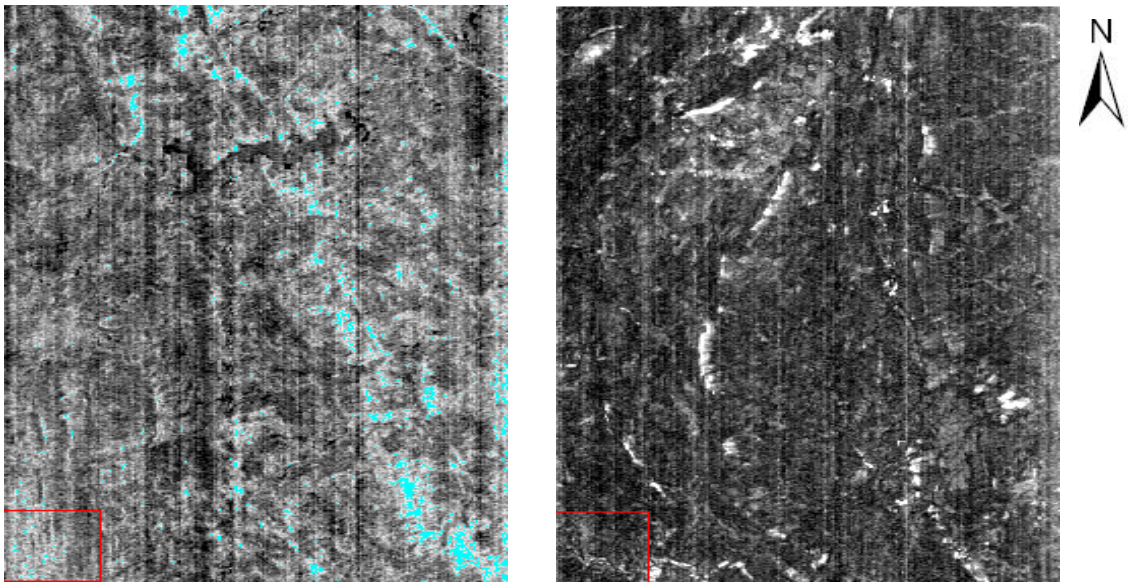

Chlorite (Score) Chlorite (Infeasibility)

Figure 4.28 MTMF mapping results for Udaipur (approximate map scale 1:40,528)

The interpretation of mixture tuned matched filtering mapping method involves the integration of close analysis of both the score and infeasibility images of the individual endmembers. The four endmember's score as well as infeasibility image are given above. The score images of kaolinite exhibits their abundance in the study area with high pixel values and they can be considered only valid if the same area have low pixel values in the infeasibility image. The kaolinite and montmorillonite are the two major clay minerals and their occurrence is primarily due to the weathering of the parent rock, quartzite which is abundant in the study area. The method indicates that both the clay minerals co-exist in the study area and their differentiability is meek using this method. Similarlly the mineral, pyrophyllite which is derived from the weathering of the parent rock, Phyllite can be differentiated and mapped using the method. The chlorite which is a retrograde metamorphic alteration mineral of existing ferromagnesian minerals is found associated with the chlorite schist in the study area. The exposures of these rock are very sparse in the study area and hence their abundance is also found low using this method. This method is very efficient in mapping the three set of minerals, kaolinite and montmorillonite as a single group, pyrophyllite and chlorite are the other two.

4.8.4 Band Absorption Depth Analysis (Udaipur)

The atmospherically corrected reflectance spectra contain compositional information of minerals, mineral mixtures, rocks and vegetation, exhibited as characteristic absorption at specific wavelength. The spectral reflectance in the visible and near-infrared wavelengths provides a rapid and inexpensive means for determining the mineralogy of samples and obtaining information on chemical composition. The significance of performing band positioning and absorption analysis is to see whether the spectra for a sample feature extracted from the atmospherically corrected Hyperion dataset of Udaipur behave in accordance with the USGS standard spectroscopic band absorption characteristics of that sample feature.

In order to attempt band position absorption, the atmospherically corrected spectra were examined at 2200 nm to 2300 nm for Udaipur quartzite. Quartz does not exhibit any significant absorption feature and is considered as featureless spectrum. Aventurine Quartz found in India has scales of Biotite / Muscovite, Zircon or Hematite distributed within it. Samples of ultra mafic origin that have Biotite / Muscovite and Zircon inclusions exhibit characteristic absorption feature at hydroxyl bands of 1400 nm and between 2200 and 2600 nm indicating presence of Fe-Mg-OH and Fe_2O_3. Figure 4.29 shows this characteristic absorption feature for the Aventurine quartz sample from India as published by USGS Denver spectroscopy laboratory (source: http://speclab.cr.usgs.gov/spectral.lib456.descript /DESCRIPT/quartz.avent.hs117.html). A similar absorption feature is also exhibited in the ASD field spectra of Udaipur quartzite and the spectra extracted from the atmospherically corrected Hyperion dataset of Udaipur, as seen in figure 4.30

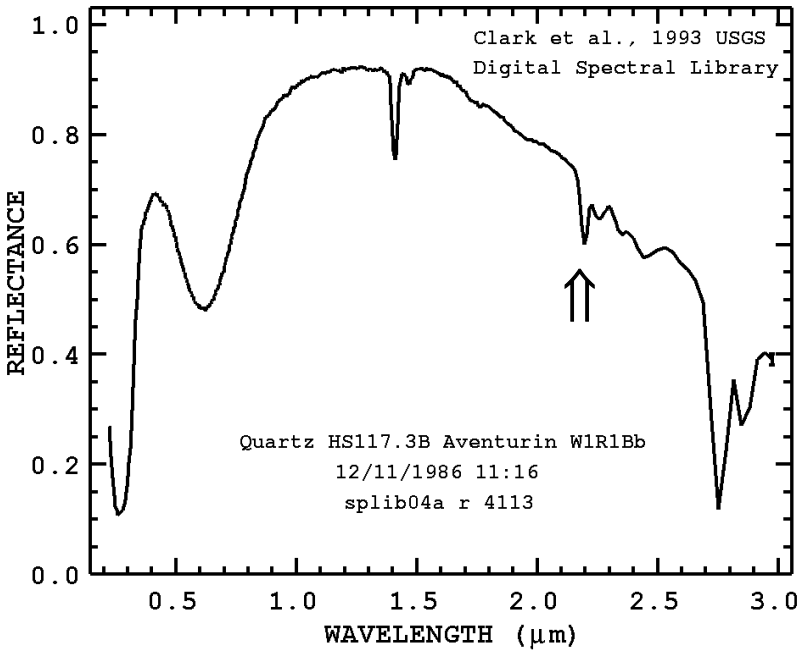

Figure 4.29 Aventurine quartz reference spectra

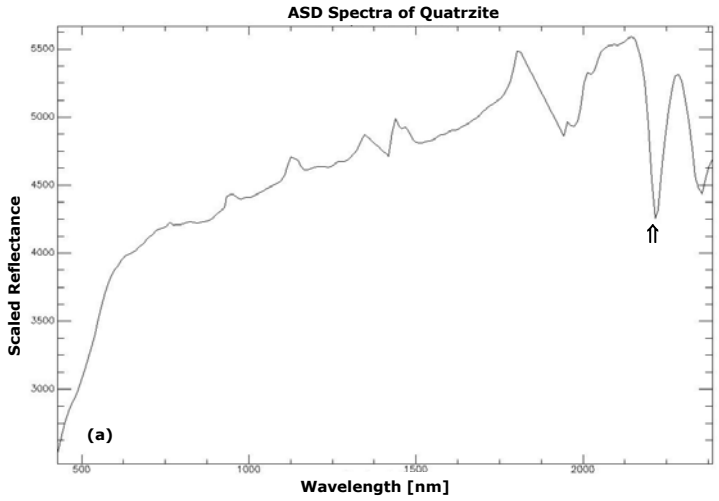

Figure 4.30 ASD spectra of Quartzite

For the derivation of asymmetry and band depth parameters (i.e. S_1, S_2, A_1, A_2) required for the band position absorption analysis, continuum removed bands between 2280 to 2340 nm were used. Two shoulders S1 at 2337.04 and S2 at 2286.55 were selected for the diagnostic absorption at 2316.84 nm. Two absorption points for interpolating the depth A1 at 2326.94 and A2 at 2296.64 were used.

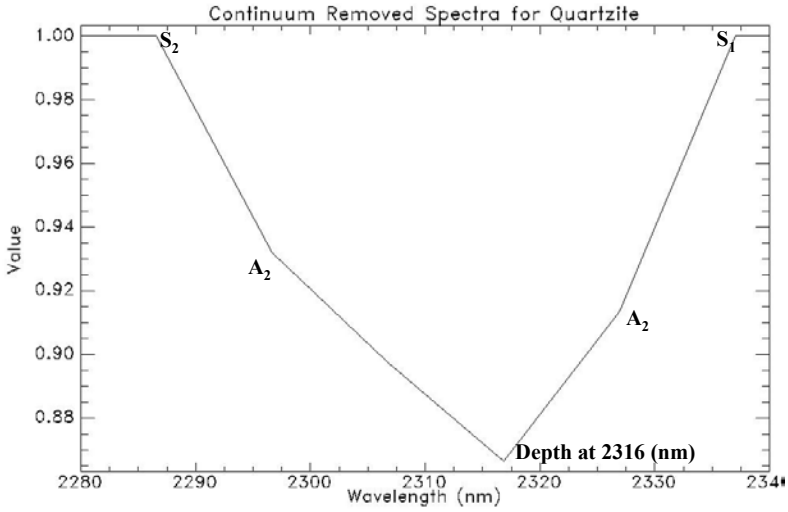

Figure 4. 31 Continuum removed absorption position of Udaipur Quartzite

The derived band asymmetry and depth images enhance the analysis of Hyperion dataset for surface compositional mapping. The resulting asymmetry image shows pixel values ranging between 0.0035 – 0.0113 and can be interpreted as weakly skewed towards the shorter wavelength. The asymmetry image displays pixels that have the same asymmetry as that of the quartzite spectra at 2316 nm.

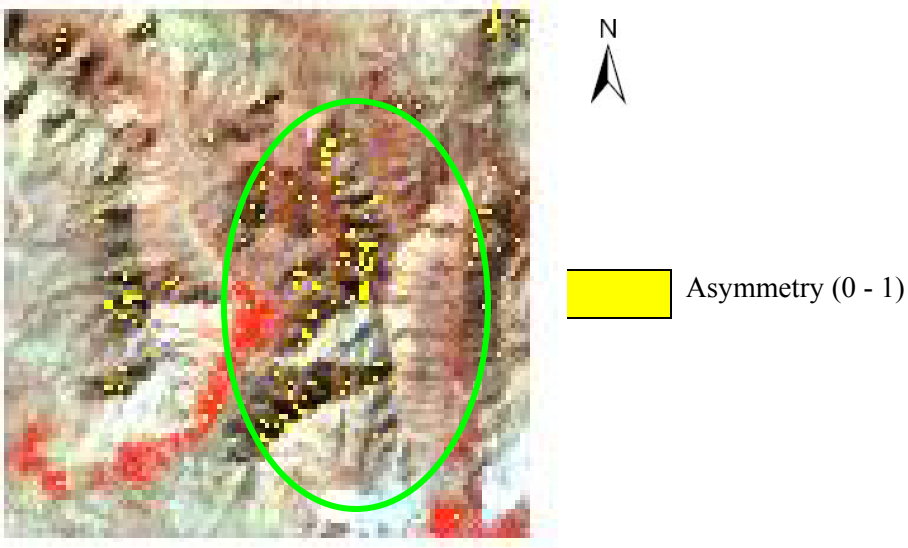

Figure 4.32 Asymmetry image for Udaipur Quartizes. Yellow pixels have asymmetry value range between 0 and 1 are weakly skewed towards shorter wavelength.

The depth of absorption feature in quartzite is higher in relation to the continuum. Higher depth values indicate a greater possibility of the occurrence of mineral that is displaying the absorption feature in the spectra.

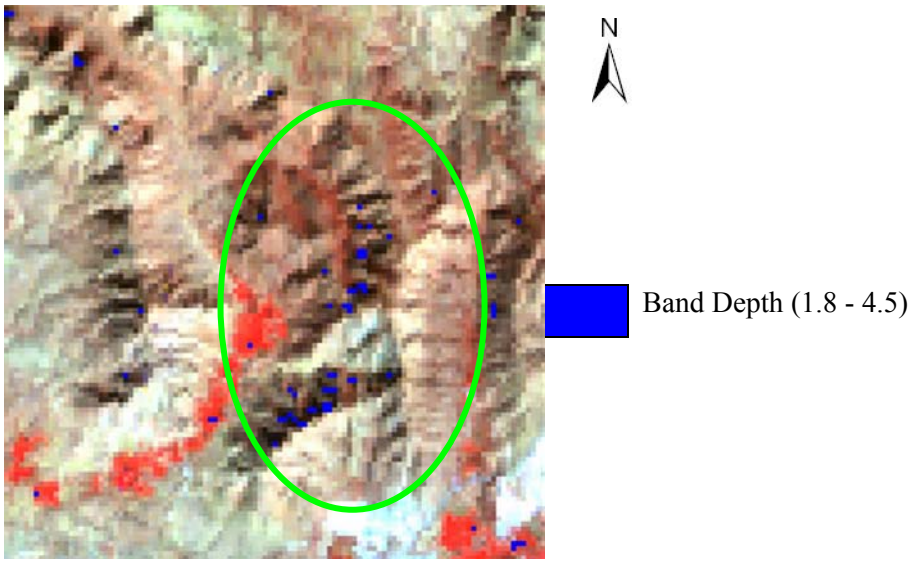

Figure 4.33 Depth image of Udaipur Quartzites. (approximate map scale 1:20,858)

Band absorption analysis has not shown good results for Udaipur hyperion dataset. In case of Udaipur Quartzite, the absorption range is covered by 6 bands. The result of band position and absorption analysis shows a very low number of pixels (2206) qualifying for the hydroxyl

band depth and asymmetry, most of which fall in the shadow region. This indicates that identification of absorption feature depends not only on the spectral quality of the dataset but also on absorption width (number of bands that constitutes the absorption range). Earlier studies have reported Hyperion SNR in the range of 1 to 60 in SWIR region resulting in less information extraction from hyperion for mineralogical targets (Kruse et al., 2003a). Other reason of underperformance of this technique for hyperion could be attributed to very strong superimposed hydroxyl absorption due to atmospheric moisture accumulation in the shadowed region of the study area. This dominant absorption interfered with the characteristic hydroxyl absorption of Udaipur quartzites. Hence the areas in shadow region show similar band depth and asymmetry in the study area.

4.8.5 Results of linear spectral unmixing (Orissa)

Linear spectral unmixing has been performed using the six endmembers of the Orissa study area. The results of this mapping technique for both the study areas are discussed below.

This models gives information about the relative abundances of the endmember material considering each endmember present in a pixel. The three endmembers used in the Orissa dataset are alluvium, minetailings and hematite. Three endmembers for the Orissa dataset have been used to describe the resultant image. The three resultant endmember abundance image and the rms image is shown below.

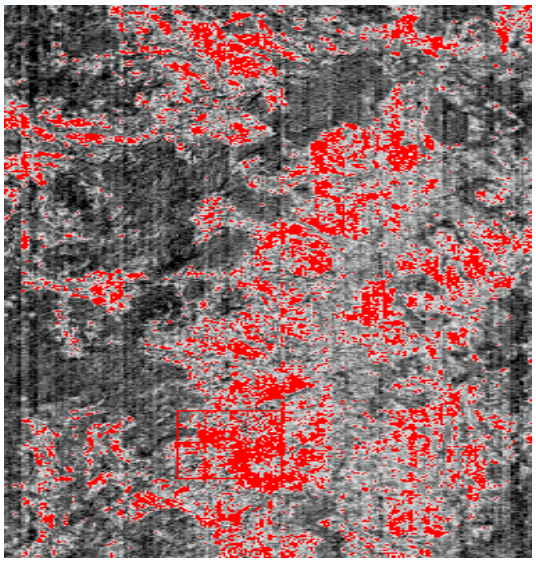

Alluvium

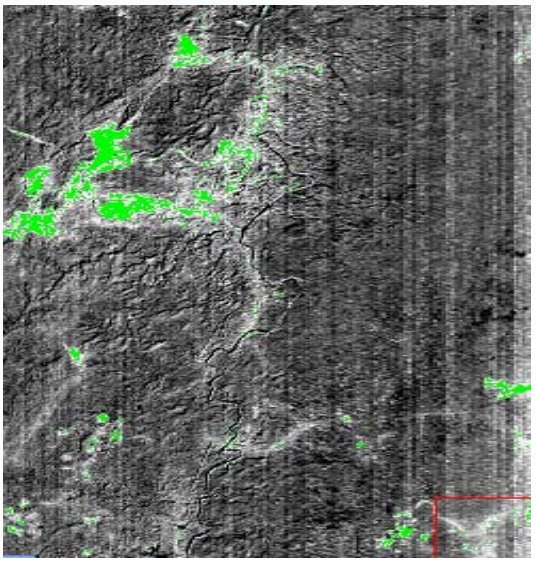

Hematite

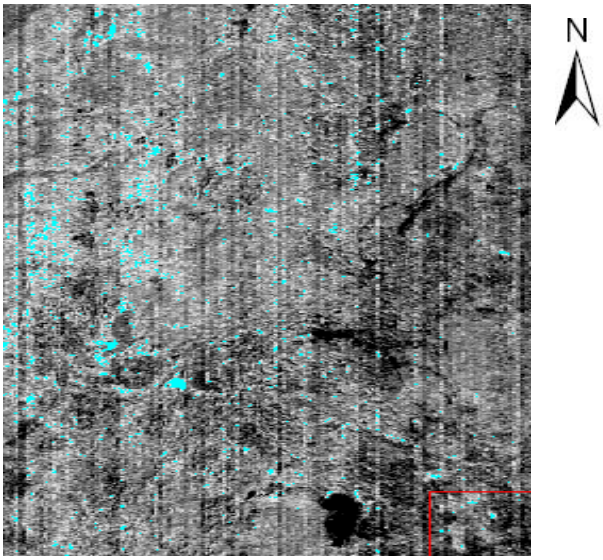

Figure 4.34 Results of linear spectral unmixing (Orissa) (approximate map scale 1:40,528)

The linear spectral unmixing results of Orissa study area clearly demarcates the hematite mineral and alluvium. This is primarily due to the characteristic absorption depth at 875nm for Fe (hematite). The minetailings which are the residue or leftout portion of the mined or target material can also be demarcated using this method, but in some location there is an intermixing between the hematite. The minetailings present in this area are also rich in iron content. They are normally discarded due to the low grade quality. They had a spectra resembling both the hematite and alluvium as discussed in section 4.6.3. They exhibit the general spectral trend of the alluvium but shows a moderate absorption depth at 875 nm which is primarily due to the Fe absorption. This absorption depth at 875 nm is basically due to the crystal field effect of transition element "Fe".

4.8.6 Results of Mixture tuned matched filtering (Orissa)

Mixture tuned matched filtering is used to perform MF and add an infeasibility image to the results. The infeasibility image is used to reduce the number of false positives that are sometimes found when using MF. Pixels with a high infeasibility are likely to be MF false positives. Correctly mapped pixels will have an MF score above the background distribution around zero and a low infeasibility value. The infeasibility values area in noise sigma units that vary in DN scale with an MF score.

The results from linear spectral un-mixing exhibits an intermixing of hematite and mine tailings. This mapping technique is adopted to differentiate between these two targets. The results from the mixture tuned matched filtering (MTMF) for the Orissa study area is given below. The score image and the corresponding infeasibility image for both hematite and minetailings are given below in figure 4.35

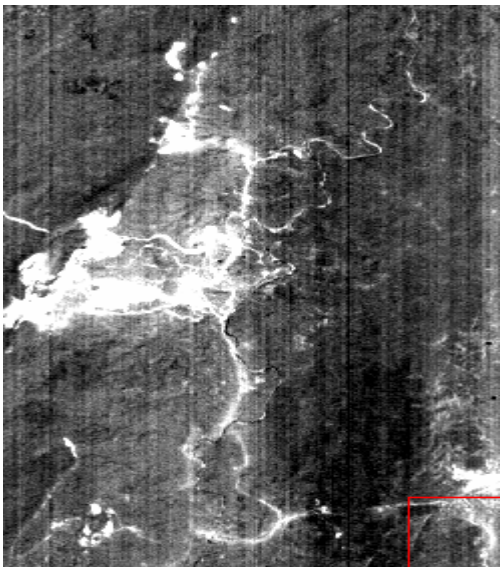

Hematite (Score)

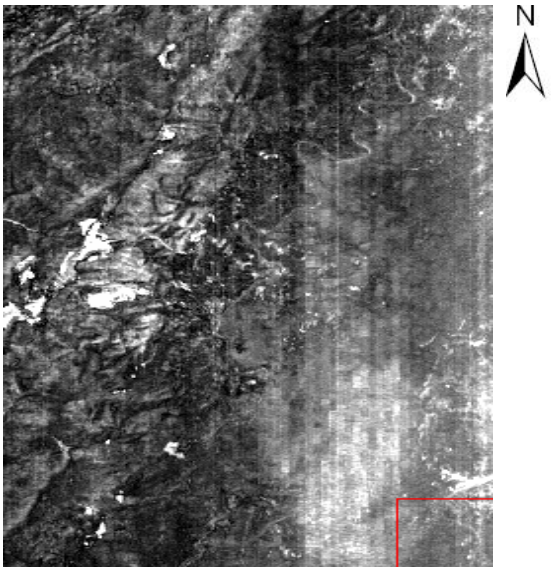

Hematite (Infeasibility)

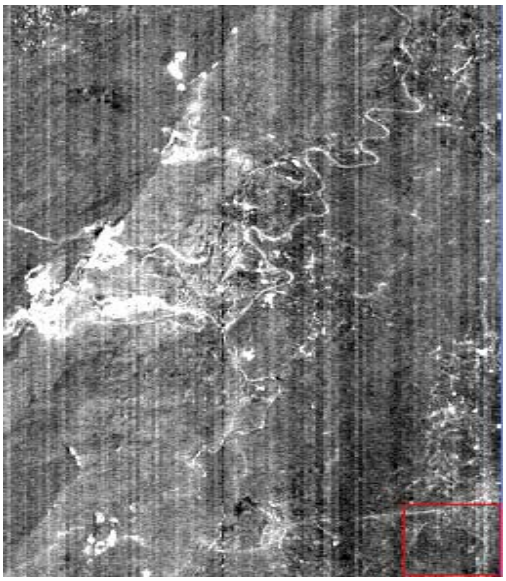

False minetailings (Score)

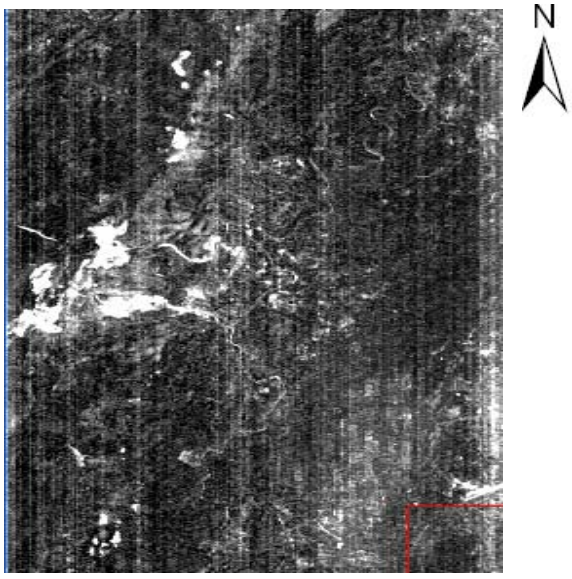

Minetailings (Infeasibility)

Figure 4.35 Results of MTMF Orissa (Scale (approximate map scale 1:40,528)

The visual interpretation of false minetailings image given above, figure 4.35 indicates that the areas with high pixel values (appearing bright) are actually false indications of minetailings. This can be understood by the close analysis of minetailings infeasibility image in which the same area appears bright with high pixel values. These areas are actually hematite mines.

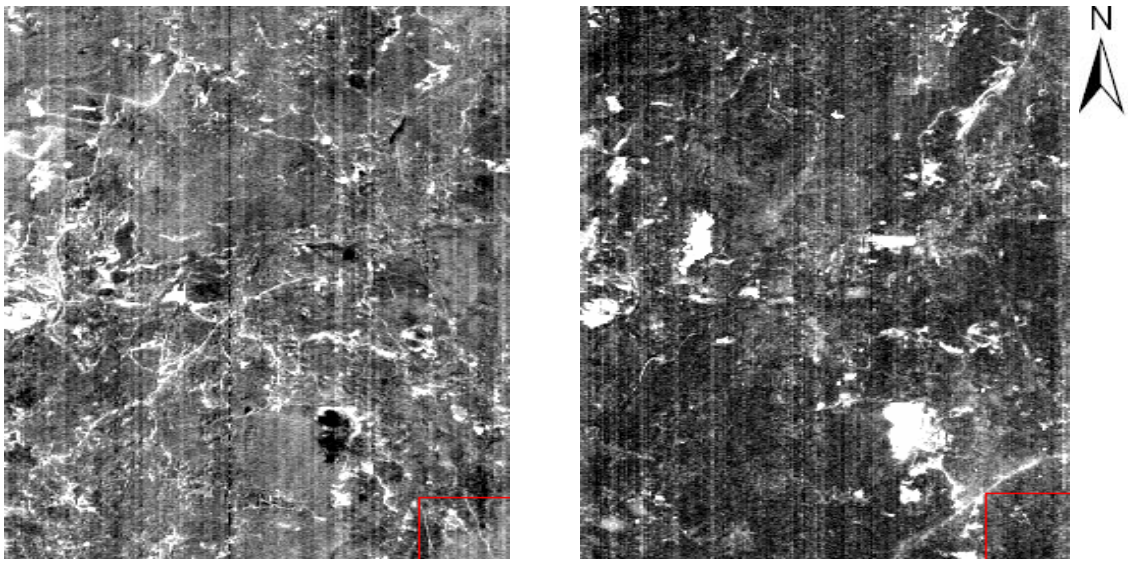

Minetailings (Score) Minetailings (Infeasibility)

Figure 4.36 Results of MTMF minetailing (approximate map scale 1:40,528)

The results of the MTMF minetailings image, figure 4.36 indicate areas of minetailings abundance. The bright pixels present in the score image indicate their abundance. The areas in the score image which have correspondingly low pixel values (appear dark) in the infeasibility image indicate their presence in ample amounts.

4.8.7 Results of Spectral Angle Mapper (Orissa)

The spectral angle mapper algorithm determines the spectral similarity between two spectra by calculating the angle between the spectra and treating them as vectors in a space with dimensionality equal to the number of bands. The output from SAM is a classified image and a set of rule images (one per endmember). The pixel values of the rule images represent the spectral angle in radians from the reference spectrum for each class. Lower spectral angles represent better matches to the endmember spectra. The SAM classification method was applied to the Orissa dataset and hematite endmember spectra was given as the reference spectra..

The rule image generated for the hematite in Orissa dataset is given below.

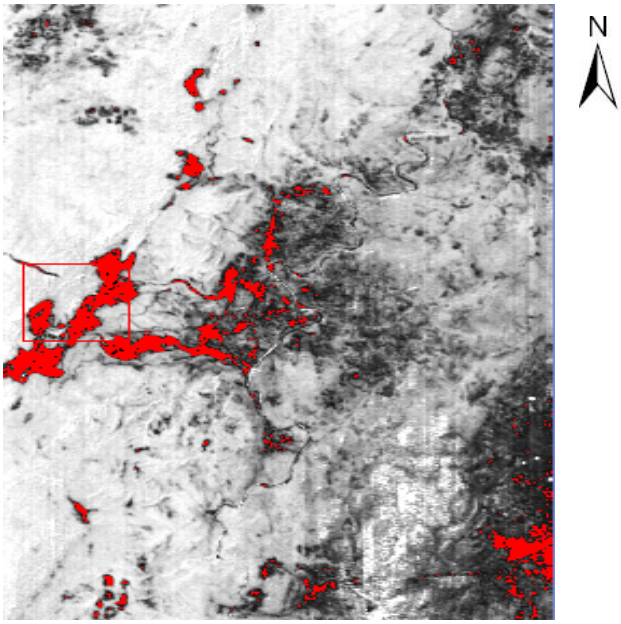

Figure 4.37 Results of SAM Hematite rule image (approximate map scale 1:40,528)

The results of the SAM mapping method for the Orissa dataset indicates that the lowest radian measurement (angle between the reference spectra and the target) have been registered for the hematite mineral. This indicates the similarity in the spectra of the reference and target spectra. This indicates that the SAM mapping method has given good results in the mapping of hematite in Orissa.

The band rationing images of LISS 4 dataset for the both the study areas are given below.

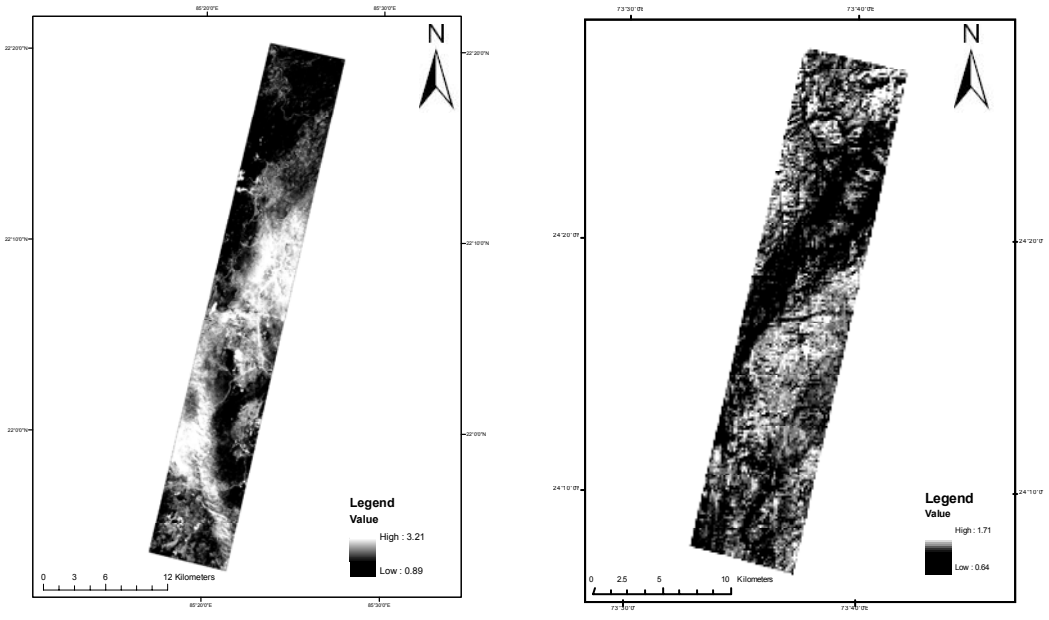

Figure 4.38 Results of band rationing of LISS IV image

4.9 Lithological Differentiation

After carefully analyzing the output images of the various mineral mapping techniques such as the Linear Spectral Unmixing (LSU), Mixture Tune Matched Filtering (MTMF) and others the different abundant materials were mapped separately from separate images. They are prepared with each other and with the result of other image processing techniques. A final lithological map was prepared from the output results. This is compared with the existing geological map of the study area.

Minerals like Montmorillonite, Kaolinite, Pyrophyllite and Chlorite has been mapped using the various mapping techniques in the Udaipur study area. Rock is a naturally occuring aggregate of minerals or mineraloids and they are basically classified based on their mineralogical as well chemical composition. The genesis and distribution of these minerals are mainly controlled by the distribution of the parent rock and the weathering process they have undergone. The results from the various mapping techniques have been analyzed to generate this final validation process. The above mentioned minerals are basically clay minerals which are alteration minerals of other major deposits. Hence it becomes very important to map the lithology of the area which may be promising to other major potential deposits.

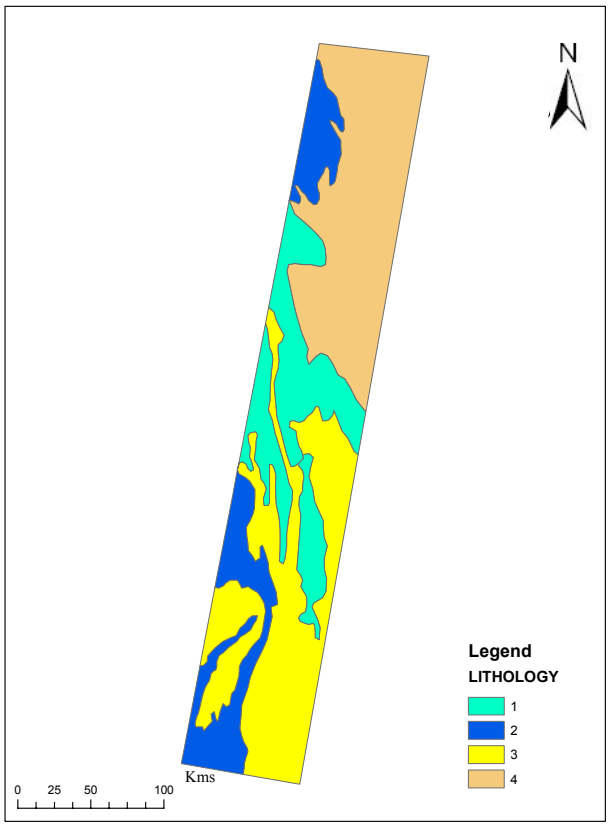

Figure 4.39 Geological map of Udaipur study area modified after Mohan Lal Sukhadia University, Department of Geology, Udaipur

The lithological explanation of the above mentioned legend is as follows.

1. Conglomerate with phyllitic matrix, greywacke – phyllite – laminated greywacke – Phyllite - rhythmite

2. Carbonaceous phyllite – slate, phyllite - mica schist

3. Quartzite – dolomite facies variation, dolomite with rock phosphate, sideritic marble and impure crystalline dolomite

4. Conglomerate with quartzitic matrix – Quartzite silty arenite

The lithosequence comprising of greywacke and phyllite is best developed around Udaipur, and hence it is designated as the Udaipur formation. They follows a rhythmic sequence of greywacke – slate/phyllite which laterly passes into lithic arenite as it moves from Udaipur. These formations are overlain by a carbonate sequence hosting Pb-Zn mineralization and is designated as the Zawar formation. Their rock sequence comprises of Phyllite, conglomeritic and gritty greywacke, dolomite. The conglomerate-arkose-grit-quartzite horizon, occurs in kailashpuri in the north of Udaipur marks the base of the Debari group and is designated as the Debari conglomerate. They are poorly sorted conglomerate and contains pebbles, cobbles and boulders of quartzite, metabasics and marble. The composition varies from arkosic and arenaceous to calcareous.

As discussed in section 4.8.1 and 4.8.3 and the figures depicting the results of the various mineral mapping techniques for Udaipur study area, it is clear that the two major rock classes have resulted in the generation of various clay and mica minerals in the study area. They are the Quartzite and Phyllite. The study area of Udaipur is dominated by these two classes of lithology.

The rock discrimination was done using two various methods, one using the spectral signatures (using the spectral library of the samples collected from the study area during the field investigation) and the tonal analysis of the reflectance image. The two major rock classes Quartzite and Phyllite and mapped based on these findings and is given in figure 4.40. The results of the mapping techniques shows the abundance of minerals like Montmorillonite and Kaolinite and their genesis is related to the weathering of the Quartzite rock. Similarly for the Pyrophyllite mineral, they are distributed in the areas pertaining to the Phyllite rock variety and their genesis is related to the weathering of the Phyllite rocks. The mineral Chlorite is found associated with the Chlorite schist rock which itself is found along with the Phyllite greywacke sequence. The mapping of the Chlorite schist rock hence becomes difficult and have been left out in the final lithological map as they may be associated with the Phyllite schist sequence.

The colour composites of classified images (mineral classified images) have been used in the present study for lithological differentiation. Three mineral classified images have been used in the colour composite image. They are the Montmorillonite, Kaolinite and Pyrophyllite. The results from the Mixture Tuned Matched Filtering (MTMF) have been used for this. The score images of these three minerals have been stacked together to generate the colour composite image.

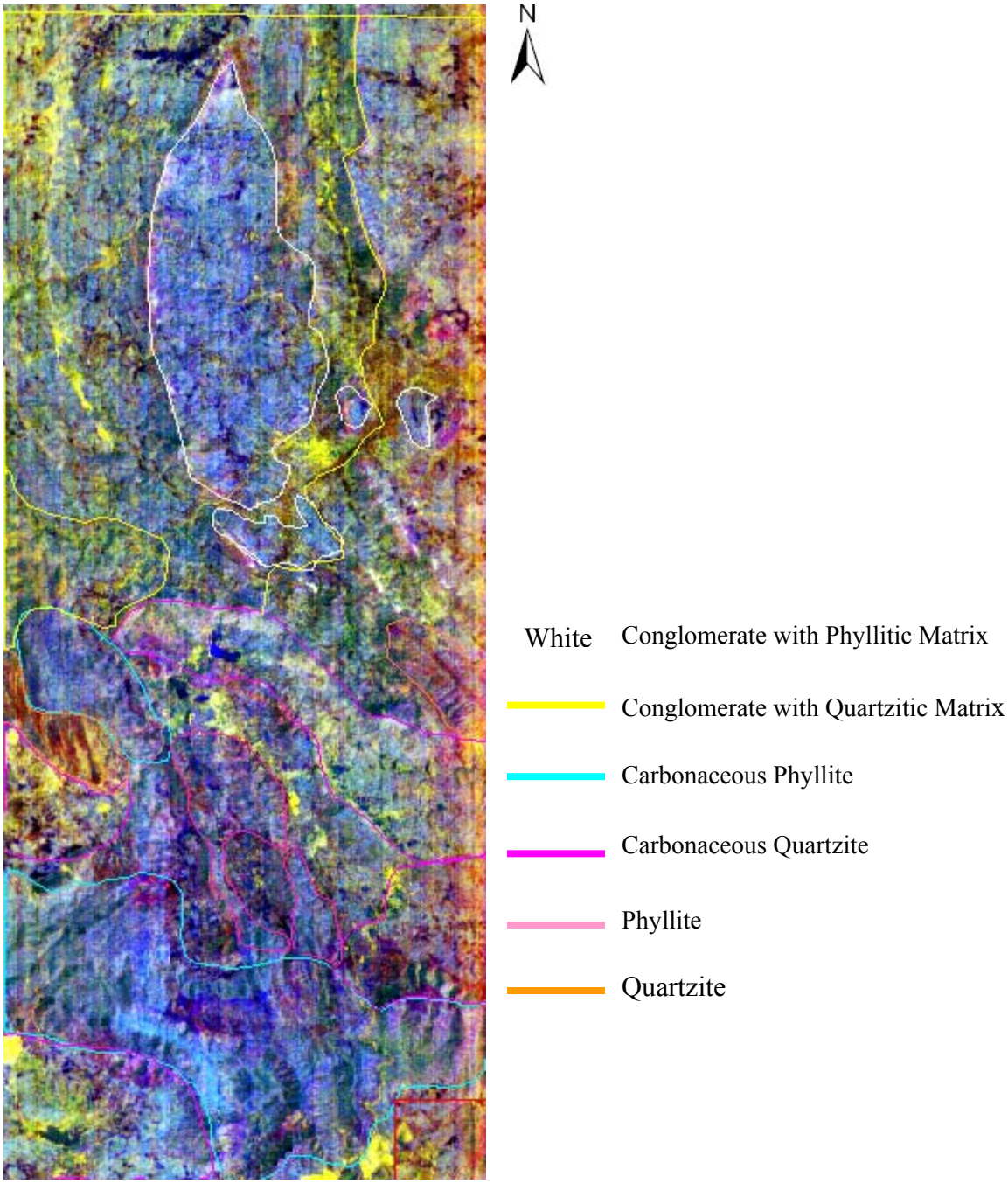

Figure 4.40 Colour composite of classified image and FCC, 47 28 15 (approximate map scale1:84,253)

Three classified mineral images of Kaolinite, Montmorillonite and Pyrophyllite have been assigned red, green and blue sources in the colour composite. The colours in the composite image gives a clear idea about the lithological boundary of the parent rock present in the study area as the three minerals (Kaolinite, Montmorilonite and Pyrophyllite) have been derived by the weathering of their respective parent rock.

Six lithologies have been demarcated in this analysis. They are depicted along with the colour composite image. They are 1. Conglomerate with phyllitic matrix, 2. Conglomerate with quartzitic matrix, 3. Carbonaceous phyllite, 4. Carbonaceous quartzite, 5. Phyllite and 6. Quartzite. In the FCC, 47 28 15 band combination of Hyperion Udaipur dataset could demarcate only three lithologies. It is the spectral analysis that have been conducted uasing the endmembers collected from the n-dimensional visualizer that enabled as to demarcate six lithologies with slight variations in the Udaipur study area. These rocks are primarily Phyllite and Quartzite but their mineralogical variations resulted in the generation of other classes of lithology.

Since Pyophyllite, the clay mineral derived from the Phyllite have been assigned blue colour, the lithology or the rock types with Phyllitic matrix exhibits bluish tint in the colour composite image. Similarlly the Montmorillonite and Kaolinite which are derived from the weathering of Quartzite rock have been assigned green and red colour gives a brownish to yellowish tint to the quartzite and arenitic variety which makes them distinguishable in the colour composite image. The pure quartzite rock exhibits brownish colur and their colurs varies from brownish to yellowish tone These findings along with the information derived from supplementary as well as auxillary sources like geologic map of the study area and information collected during the ground-truth investigation have immensely helped in the demarcation of six lithologies in the Udaipur study area.

Chapter 5

Conclusions and recommendations

This chapter deals with the various conclusions that have been arrived at the end of the study. The primary objective of this study was to retrieve reflectance from the raw (radiance) data from Hyperion dataset and to evaluate its application potential in mineral exploration in the two selected study areas. The two study areas selected for this study are the Udaipur in Rajasthan and Keonjhar (Jamda-Koira valley), Orissa, India. Geologically both the study areas belong to the Precambrian era of the geological time scale.

Recent advances in remote sensing and geographic information has led the way for the development of hyperspectral sensors. Hyperspectral remote sensing, also known as imaging spectroscopy, is a relatively new technology that is currently being investigated by researchers and scientists with regard to the detection and identification of minerals, terrestrial vegetation, and man-made materials and backgrounds. Hyperspectral data sets are generally composed of about 100 to 200 spectral bands of relatively narrow bandwidths (5-10 nm), whereas, multispectral data sets are usually composed of about 5 to 10 bands of relatively large bandwidths (70-400 nm) (www.csr.utexas.edu/projects/rs/hrs/hyper.html). With the increase in the number of bands, the volume of information it gives are enormous and the challenges it poses for a researcher is also ample. Being a new and innovative technology, this branch of remote sensing is under tremendous growth and is going to be the face of the remote sensing technology in the coming decade.

5.1 Conclusions

Pre-processing of the hyperspectral dataset is one of the initial steps included in the retrieval of atmospherically corrected reflectance data. The Hyperion satellite data contains 242 bands. All the entire bands do not contain information basically due to the atmospheric attenuation. Spectral subsetting need to be done to remove those badly affected bands. This process leaves 196 unique hyperion bands in the dataset. The visual analysis of the several bands among the 196 bands in the hyperion dataset indicates that there are number of vertical stripes encroached in to the dataset, which is primarily due to the sensor faults. These stripes are removed using 3*3 local filter and it removes only the spurious pixel values present in the striped area, which doesn't represent any characteristics of the target sensored. This local balancing technique improved the spectra of the dataset once the reflectance is retrieved from the radiance image.

Two atmospheric correction techniques have been employed to retrieve the reflectance from the radiance. FLAASH and ATCOR 2.3 based on the MODTRAN. ATCOR and FLAASH both use MODTRAN and has out performed other radiative transfer code especially in the water region 940. Visual comparison of the ATCOR 2 and FLAASH retrieved reflectance spectra indicated that both the models compensated for the O_2, and CO_2 atmospheric gas absorptions. The SWIR portion of the reflectance spectra exhibited spurious spikes in both the atmospheric correction models. Since two models have been used in the present study, it is very important to estimate their comparative performance. This will help in selecting the better-performed model result, which can be used for further spectral analysis and mineral mapping. Validation of the two models have been done using the spectral similarity parameters SAM and NED. They have been used considering the Analytical Spectral Device (ASD) derived spectra as the standard. SAM

exhibited lower values for the ATCOR derived spectra than the FLAASH and can be stated that the ATCOR had better performed than FLAASH. Low NED values of the FLAASH derived spectra indicated their better performance when compared to that of the ATCOR. Since NED being a better similarity measure, it has been stated that FLAASH atmospheric correction model have performed better than ATCOR2 model. Spectral polishing technique EFFORT was performed on FLAASH reflectance result to smoothen the reflectance spectra. Hence FLAASH derived reflectance data have been selected for the further spectral analysis and mineral mapping for both the study areas.

During the field investigation, rock samples were collected from both the study areas which have been used to generate the field spectra (reference spectra) using ASD. The endmembers were selected after understanding the geology of both the study areas. Three endmembers were selected for Orissa and five endmembers were selected for Udaipur. The number of endmembers selected also depends upon the mapping technique used. Linear spectral Unmixing technique requires all the land use classes to be included to give a better result. The endmembers were collected after spectral processing of the reflectance data which is discussed in section 3.13.1. After collection of endmembers they are used in various mapping techniques.

Mapping technique such as linear spectral unmixing, mixture tune matched filtering, spectral feature fitting, spectral angle mapper and band absorption depth analysis were used to map the different endmembers. For Udaipur study area, Kaolinite, Montmorillonite, Pyrophyllite and Fe rich Chlorite (Chamosite) were mapped. Linear spectral unmixing results for Udaipur helps in mapping Kaolinite and Montmorillonite. There is an intermixing between the Pyrophyllite and Montmorillonite in the linear spectral unmixing results. Due to the unique iron absorption at 870 nm Fe rich Chlorite (Chamosite) have been successfully mapped using this method. Spectral feature fitting technique uses an approach in which individual adsorption depths of the endmembers are not taken into consideration and this resulted in poor results for this method. The mixture tuned matched filtering technique was successful in mapping Pyrophyllite and Chamosite but shows intermixing between Kaolinite and Montmorillonite. The Kaolinite and Montmorillonite are derived from the weathering of the parent material, Quartzite, where as the Pyrophyllite is derived from Phyllite and Chamosite forms a part of Chlorite schist. The band absorption depth analysis was conducted on Udaipur dataset and gave poor results and this could be attributed to the very strong superimposed hydroxyl absorption.

For Orissa study area, linear spectral unmixing, Spectral angle mapper, MTMF were used to map the endmembers. The three endmembers used for the Orissa study area are Hematite, Minetailings and Alluvium. The linear spectral unmixing method successfully mapped the hematite and alluvium but showed intermixing between minetailing and hematite in minetailing abundance image. The MTMF method was adopted for the Orissa study area primarily to differentiate between the hematite mineral and minetailings which were intermixed in the Linear spectral unmixing result. The MTMF successfully conducted the abundance mapping for hematite and minetailing. The final interpretation of the MTMF results need to be done after integrating the score image results to that of the infeasibility image for all the endmembers. Spectral angle mapper (SAM) also gives good results for hematite but showed intermixing between alluvium and minetailings.

Band rationing of LISS 4 images were generated to map the clay minerals in Udaipur and the Hematite mineral in Orissa study area. The band rationing results of Udaipur highlighted the clay minerals but was incapable of demarcating the variety among them as been expected from a multispectral dataset. Similarly for the Orissa data set, all the features other than water and

vegetation got highlighted in band rationing as the area has high concentration of iron content due to mining activities.

An integrated approach of different mapping technique gives a much better result than depending on a single method. Results from several mapping methods have helped in the mineral abundance mapping.

The careful analysis of the classified mineral images have been done for the lithological differentiation in the Udaipur study area. A colour composite image of Montmorillonite, Kaolinite and Pyrophyllite has been generated to meet this objective. Six major lithologies have been demarcated as a result of this analysis. They are Conglomerate with Quartzitic and Phyllitic matrix, Carbonaceous Phyllite, Carbonaceous quartzite, Phyllite and Quartzite.

The following research questions were answered to meet the objectives of the present study.

5.1.1 Can the existing the pre-processing techniques used in the multispectral images sufficient for the efficient feature extraction in hyperspectral data?

The hyperspectral dataset contains numerous bands with very narrow spectral bandwidth, 10 nm in the case of hyperion. The multispectral images contain three to four bands with very broad bandwidth. This itself gives an overview about the amount of information the hyperspectral sensor gives. Proper pre-processing of hyperspectral dataset, which includes the spectral subsetting of noise prone bands, destriping of vertical columns in the bands need to be done to achieve a less noise prone dataset. The broad bandwidths of the multispectral images are less affected by the atmospheric attenuation. Hence the pre-processing approach for the multispectral and hyperspectral satellite data need to be different.

5.1.2 How good are the atmospheric correction models that have been used for the retrieval of reflectance in hyperspectral (Hyperion L1R) data?

FLAASH and ATCOR2 atmospheric correction models have been used in the present study. The visual comparison of the reflectance spectra derived form both the atmospheric correction models have performed well enough to retrieve the spectral characteristics of the target sensored. The SWIR portion of the spectrum is largely affected by the various absorbing gases present in the atmosphere. Most of the mineral species have characteristic absorptions in SWIR portion of the spectrum. Both the atmospheric correction models could not remove the spurious spikes in the SWIR portion of the spectrum, which cannot be attributed to any spectral characteristics of the object under study.

5.1.3 Which among the various mapping techniques are the most efficient for the mineral mapping?

Various mapping techniques have been employed in this study. Linear Spectral Unmixing, Mixture Tune Matched Filtering, Spectral Angle Mapper, Band Absorption Depth Analysis and Spectral Feature Fitting are few of the techniques that have been used in the study. A single mapping technique has not given all the endmember classified result. In the case of Udaipur study area, Mixture Tune Matched Filtering as well as linear spectral unmixing was successful in mapping all the endmembers. Similarly, in Orissa study area, linear spectral unmixing as well as Mixture Tune Matched Filtering have given good results. Hence it can be

concluded that an integrated approach of several mapping techniques will lead to the successful mapping of the endmembers.

5.1.4 Can the statistical parameters like SAM (Spectral Angle Mapper) and NED (Normalised Euclidean Distance) be used as the validation parameters for the various atmospheric correction models?

As stated by the previous study conducted by Robila and Gershman 2005, it was proved that the techniques based on image ratio and difference such as Spectral Angle Mapper (SAM), Normalized Euclidean Distance (NED) provide useful information on spectral similarity between reference and test spectra. This approach was selected to validate the performance of two atmospheric correction models (FLAASH and ATCOR2) that has been used in the present study. According to these statistical parameters, FLAASH atmospheric model have outperformed the ATCOR2 model for both the study areas and hence been taken up for mineral abundance mapping in both the areas.

5.2 Recommendations

- Mineral prospecting need to be conducted by taking into account various factors including the landuse-landcover of the study area. Geo-botanical anomaly is an important criteria in this regard. These anomalies induces spectral shift in the chlorophyll absorption at 0.66 and 0.68 μm.. The changes in the chlorophyll concentration produces spectral shift in the reflectance spectra of the vegetation. This phenomenon is called red edge shift. Inclusion of these parameters in the prospecting will ensure a better and comprehensive result in mineral abundance mapping which has not been taken into consideration in this study due to lack of knowledge and experience in vegetation studies.

- Both the atmospheric correction models have not compensated well enough for the sporadic spikes in the SWIR portion of the spectrum. Improvement in the SWIR portion of the spectrum will enhance the prospecting capability of the hyperion dataset in future studies as most of the minerals have characteristic absorptions in the SWIR portion.

- Improvement in SNR of Hyperion sensor should be worked out for future space borne Hyperspectral sensors to allow the same level of mineral mapping capability as airborne sensors.

References

Bakliwal, P.C. and Ramasamy, S. M. (1987). Lineament fabric of Rajasthan and Gujarat, India, Rec. Geol. Surv. Ind., v.113 (7), pp. 54-64.

Bateman, P.C. (1988) Constitution and Genesis of the Central Sierra Nevada Batholith, California. U.S. Geological Survey Open File Reports: 88-382, 284p

Boardman, J.W. (1989). Inversion of Imaging Spectrometry data using singular value decomposition (abs): in proceedings, IGARSS'89, 12 Canadian Symposium on Remote Sensing, Vol. 4.

Boardman, J.W. (1993). Automated spectral unmixing of AVIRIS data using convex geometry on concepts in summaries (abs). Fourth JPL Airborn Geosciences Workshop, JPL Publication 95-26.

Boardman, J.W., Kruse, F.A. (1994). Automated spectral analysis: A geologic example using AVIRIS data, north Grapevine Mountains, Nevada: in proceedings, Tenth Thematic conference on geologic remote sensing, Environmental research institute of Michigan, Ann Arbor

Boardman, J.W., Kruse, F.A., and Green, R.O. (1995). Mapping target signatures via partial unmixing of AVIRIS data in summaries (abs), Fifth JPL Airborn Earth Science Workshop, JPL publication 95-1.

Cappaccioni B., Vaselli O., Moretti E., Tassi, F., Franchi R. (2003), The Origin of thermal water from the eastern flank of the Dead Rift Valley, Terra Nova, volume 15 issue3, page145.

Chen, .Y., Reed, I.S., 1987., A detection algorithm for optical target in clutter. IEEE Transactions on Aerospace and Electronic System AES-23, 46-58.

Clark, R.N., King, T., Klejwa, M. and Swayze, G.A., 1990. High spectral resolution reflectance spectroscopy of minerals. Journal of Geophysical research 95 (B8): 653-680

Cudahy, T.J., 1992. A Model for the development of the regolith of the Yilgam Craton incorporating selected spectral information. CSIRO exploration Geoscience Restricted Report 43R 26pp.

Cudahy and In Papp, E., 2002 Geophysical and Remote Sensing Method for Regolith Exploration CRCLEME Open File Report 144, pp 13-21.

Cunningham, C.G., Arribas, A.J., Rythba, J.J. and Arribas, A., 1990. Mineralized and unmineralized calderas in Spain; Part I, evolution of Los Frailes Caldera. Mineral Deposita, 25: 21-28.

Datt, B., McVicar, T.R., Van Niel, T.G., Jupp, D.L.B. and Pearlman, J.S., 2003. Preprocessing EO-1 Hyperion hyperspectral data to support the application of agricultural indexes. IEEE Transactions on Geoscience and Remote Sensing, 41(6 Part 1): 1246-1259.

Dunn, J.A., (1940). The stratigraphy of South Singhbhum. Mem. Geol. Surv. Ind., V 63, pt. 3,

Edgardo G. , James J. Hurtak (1992) : Laser Remote Sensing of Forest and Crops in Genetic-Rich Tropical. International Archives of Photogrammetry and Remote Sensing, Vol. XXIX, ISPRS, 7 pages.

Gathania, R.C et al. (1995). Occurrence of ultramafics of komatiitic affinity in the Rakhabdev-Dungarpur belt, Udaipur and Dungarpur Dists. Rajasthan, Jour. Geol. Soc. Ind. V.46, pp.585-594.

Ghosh, P.K. (1933). Talc-serpentine-chlorite rocks of southern Mewar and Dungarpur, Rec. Geol. Surv. Ind. V. LXVI(4).

Goodenough, G.D., Dyk, A., Niemann, O.K. and Pearlman, J.S., 2003. Preprocessing Hyperion and ALI for forest classification. IEEE Transactions on Geoscience and Remote Sensing, 41(6 Part 1): 1321-1331

Green, A.A., and Craig, M.D. (1985), Analysis of aircraft spectrometer data with logarithmic residuals (abs): in proceedings, AIS work shop, 8-10 april, 1985, JPL publications 85-41, Jet Propulsion Laboratory, Pasadena, California.

Gross, H.N. and Schott, J.R., 1998. Application of Spectral Mixture Analysis and Image Fusion Techniques for Image Sharpening. Remote Sensing of Environment, 63(2): 85-94.

Griffin, M.K. and Hsiao-hua, K.B., 2003. Compensation of Hyperspectral data for atmospheric effects. Lincoln Laboratory Journal, 14(1): 29-53.

Gupta et al. (1981). Lithostratigraphic map of Aravalli region, Southeastern Rajasthan and northern Gujarat, Geol. Surv. Ind., Hyderabad

Harsanyi, J.C., Chang, C., 1994. Hyperspectral image classification and dimensionality reduction: An Orthogonal subspace projection approach. IEEE Transactions on Geoscience and Remote Sensing 32, 779-785.

Heron, A.M. (1953). The geology of central Rajaputana, Mem. Geol. Surv. Ind., v. 79, pp. 1-389.

Hunt, G.R., Salisbury, J.W. and Lehnoff, C.J., 1971. Visible and near infrared spectra of minerals and rocks: 111. Oxides and Oxyhydroxides. Modern Geology 2: 195-205.

Janssen, L.L.F., Weir, M.J.C., Grabmaier, K.A. and Kerle, N., 2004. Geometric aspects. In: N. Kerle, L.F.L. Janssen and G.C. Huurneman (Editors), Principles of remote sensing. ITC education text book series. The international institute for geo-information science and earth observation (ITC), Enschede, pp. 317-345.

Jones, H.C. (1934) – The Iron ore deposits of Bihar and Orissa. Mem_Geological Survey of India Vol. 63 pp. 2.

Jupp, D.L.B., Datt, B., Lovell, J., Campbell, S. and King, E., 2004. Backgroung notes for Hyperion data user workshop, CSIRO office of space science and applications, Earth Observation Centre.

Kneizys, F.X. et al., 1996. The MODTRAN 2/3 Report and LOWTRAN 7 MODEL, Phillips Laboratory, Geophysics Directorate.

Kruse, F.A., Kiereinyoung, K.S. and Boardman, J.W., 1990. Mineral Mapping at Cuprite, Nevada with a 63-Channel Imaging Spectrometer. Photogrammetric Engineering and Remote Sensing, 56(1): 83-92.

Kruse, A.Fred., 2002. Comparison of AVIRIS and Hyperion for Hyperspectral Mineral mapping.

Kruse, F.A., Boardman, J.W. and Huntington, J.F., 2003b. Final Report: Evaluation and Geologic Validation of EO-1 Hyperion, NASA.

Lillesand, T.M. and Kiefer, R.W., 1999. Remote Sensing and Image Interpretation. John Wiley & Sons, Inc, 9-10, 592-597 pp.

Lt.Colonel James Todd - Annals and Antiquities of Rajasthan (1829-32)

Matthew, M.W. et al., 2000. Status of atmospheric correction using a MODTRAN4-based algorithm, Algorithms and Technologies for Multispectral, Hyperspectral, and Ultraspectral Imagery VI. SPIE, Orlando, FL, USA.

Matthew, M.W. et al., 2000. Status of atmospheric correction using a MODTRAN4-based algorithm, Algorithms and Technologies for Multispectral, Hyperspectral, and Ultraspectral Imagery VI. SPIE, Orlando, FL, USA

Middlemiss, C.S. (1921). Geology of Idar state. Mem Geol. Surv. Ind., v. XLIV(1).

Murthy, V.N. and Acharya, S. (1975) – Lithostratigraphy of the Preccambrian rocks around Koira, Orissa, Jr. Geol. Soc. Ind. Vol 16 (1) pp 55-68

Paliwal, B.S. (1988). Deformation pattern in the rocks of the Aravalli Super group around Udaipur city, Rajasthan. Mem. Geol.Soc. Ind, v.7, pp.153-168.

Pandya, M.R. et al., 2002. Bandpass solar exoatmospheric irradiance and Rayleigh optical thickness of sensors on board Indian Remote Sensing Satellites-1B, -1C,-1D, and P4. IEEE Transactions on Geoscience and Remote Sensing, 40(3): 714 - 718.

Pantazis, M. et al., 1998. Trade Studies in Multi/hyperspectral Imaging Systems Final Report.

Pearlman, J.S. et al., 2003. Hyperion, a space-based imaging spectrometer. Ieee Transactions on Geoscience and Remote Sensing, 41(6): 1160-1173

Pollard, P.J., 1995. Geology of rare metal deposits: An introduction and overview. Economic Geology 90: 489-494.

Prasada Rao, G.H.S.V.et al (1964) – Stratigraphic relations of Precambrian Iron formations and associated sedimentary sequences in parts of Keonjhar, Cuttack, Dhenkanal and Sundargarh dist, Orissa, Proc 22nd Ind Geol. Sec. 10 72-87.

Ramsey, E. and Nelson, G., 2005. A whole image approach using field measurements for transforming EO1 Hyperion hyperspectral data into canopy reflectance spectra. International Journal of Remote Sensing, 26(8): 1589-1610

Robila, S.A. and Gershman, A., 2005. Spectral matching accuracy in processing hyperspectral data. IEEE Transactions on Geoscience and Remote Sensing, 1(1): 163- 166

Roy, A.S. (1988). Stratigraphic and tectonic framework of the Aravalli Mountain Range. In : A.B. Roy (Eds.) Precambrians of Aravalli Mountain, Rajasthan, India, Mem. Geol. Soc. Ind., v.7, pp. 3-31.

Roy, S.-S., Malhotra, G. and Mohanty, M., 1998. Geology of Rajasthan. Geological Society of India, Balgalore, 278 pp.

Sabins, H.F. – Remote sensing, Principles amd interpretation edition (Text) pp 177 – 233.

Saha, A.K.; Sarkar, S.N. (1986) – Early history of the Earth evidences from eastern Indian Shield. Gr. Discussion, Dhanbad (Abst) : 1-2.

Sarkar, S.N. and Saha, A.K. (1977) – The present status of the Precambrian stratigraphy, tectonic and geochronology of Singhbhum, KJR-Mayurbhanj region, eastern India, Ind. Jr. Earth Sc. Pp 37-65.

Sarkar, S.N and Saha, A.K. (1983) – Structure and tectonics of the Singhnhum Orissa Iron Ore craton, Eastern India, Recent researches in Geology, Vol 10, pp 1-18.

Sinha-Roy, S. (1988). Proterozoic Wilson Cycles in Rajasthan. In : A.B. Roy (Eds) Precambrians of Aravalli Mountain, Rajasthan, India, Mem, Geol. Soc. Ind. V. 7, pp. 95-105.

Sinha-Roy, S et al. (1993b). Conglomerate horizons in south central Rajasthan and their significance on Proterozoic stratigraphy and tectonics of the Aravalli and Delhi fold belts, Jour. Geol. Soc. Ind., v.41, pp. 331-350.

Staenz, K., Secker, J., Gao, B.C., Davis, C. and Nadeau, C., 2002. Radiative transfer codes applied to hyperspectral data for the retrieval of surface reflectance. ISPRS Journal of Photogrammetry and Remote Sensing, 57(3): 194-203.

Van der Meer., Imaging Spectrometry and the Ronda Peridotites (PhD Thesis, Wageningen Agricultural University, 1995).

Van der Meer, F. and De Jong, S., 2003. Imaging Spectrometery. Basic Principles and Prospective Applications, 4. Kluwer Achademic Publishers, Dordrecht/ Boston/ London, 35 pp.

Van der Meer, F., 2004. Analysis of spectral absorption features in hyperspectral imagery. International Journal of Applied Earth Observation and Geoinformation, 5(1): 55-68.

Van der Meer, F., 2006. The effectiveness of spectral similarity measures for the analysis of hyperspectral imagery. International Journal of Applied Earth Observation and Geoinformation, 8(3): 3-17.

Weissbeod T., Karcz I., Abed A., (1988), Discussion on the supposed Precambrian palaeosuture along the Dead Sea Rift , journal of the Geological Society, volume 142, number 3, 527-531.

Other references

http://www.geolmlsu.org/geology.html

http://glovis.usgs.gov/

http://geo.arc.nasa.gov/sge/health/sensor/sensors/irsp6.html

http://www.crisp.nus.edu.sg/~research /tutorial/e ye.htm

http://www.gisdevelopment. net/tutorials/tuman008.htm

http://www.csr.utexas.edu/ projects/rs/hrs/hyper.html

http://speclab.cr.usgs.gov/spectral.lib456.descript /DESCRIPT/quartz.avent.hs117.html